Numerical Investigation of the Cooling Performance of Microchannel Heat Sinks under Uniform and Non-Uniform Heating Conditions

Ling Ling

A Thesis

in

The Department

of

Mechanical an Industrial Engineering

Presented in Partial Fulfillment of the Requirements

for the Degree of Master of Applied Science (Mechanical Engineering) at

Concordia University

Montreal, Quebec, Canada

March 2012

CONCORDIA UNIVERSITY
School of Graduate Studies

This is to certify that the thesis prepared

By: **Ling Ling**

Entitled: **"Numerical Investigation of the Cooling Performance of Microchannel Heat Sinks under Uniform and Non-Uniform Heating Conditions"**

and submitted in partial fulfillment of the requirements for the degree of

Master of Applied Science (Mechanical engineering)

complies with the regulations of the University and meets the accepted standards with respect to originality and quality.

Signed by the final examining committee:

Dr. R. Sedaghati	Chair
Dr. Lyes Kadem	Examiner
Dr. Otmane Ait Mohamed	Examiner External
Dr. Ibrahim Hassan	Supervisor

Approved by: Dr. A. K. Waizuddin Ahmed MASc Program Director

Department of Mechanical and Industrial Engineering

Dr. Robin A. L. Drew

Dean of Faculty of Engineering & Computer Science

Date December 20th, 2012

Abstract

Numerical Investigation of the Cooling Performance of Microchannel Heat Sink under Uniform and Non-Uniform Heating Conditions

Ling Ling

High-power electronic devices are now widely applied in computer, mechanical and sustainable energy industries. As electronic devices become further more integrated and powerful, more effective cooling is required to remove increasing heat fluxes generated by smaller devices. Microchannel heat sink has been recognized as a very promising cooling technology since it was brought up by Tuckerman and Pease.

The purpose of the present work is to numerically study the cooling performance of microchannel heat sinks under non-uniform heating conditions and to compare to that under uniform heating conditions. Water with temperature-dependent properties is used. The temperature distribution, pressure drop, and total thermal resistance of the heat sink are selected as criteria of their cooling performance. The heat sinks are tested under various inlet velocities and heat fluxes. Firstly, cross-linked microchannel heat sink is used for cooling of heat source with hotspots. Three widths of cross-linked channel which are 0.5 mm, 1 mm, 2 mm are compared to straight channel with different positions and amount of hotspots on the bottom surface of the heat sink. Secondly, straight channel micro heat sinks are studied and optimized

under continuously varying heat flux conditions. Two layouts of the heat sink are proposed on which heat fluxes change perpendicular and along flow direction, respectively. Then, the layout with better cooling performance is optimized with Taguchi method. Finally, a novel swirl channel heat sink is employed for cooling of continuously varying heat flux conditions on a circular plate and is compared to uniform heating. Erenow, four cross sectional geometries of the channel (rectangular, trapezoidal, inverse-trapezoidal, and isosceles triangular) are compared for the heat sink.

Table of Contents

List of Tables

List of Figures

Nomenclature

Symbols

A	=	area (m^2)
C_p	=	specific thermal capacity (J/kg·K)
D	=	diameter (mm)
E	=	error
H	=	height (mm)
f	=	friction factor
k	=	thermal conductivity (W/m·K)
L	=	length (mm)
L^*	=	dimensionless distance $y/(D_h Re)$
P	=	pressure (Pa)
Pr	=	Prandtl number
$\dot{q}$	=	heat flux (W/m^2)
$\dot{Q}$	=	power (W)
r	=	radius (mm)
R	=	thermal resistance (K/W) $(T_{max} - T_{\min})/\dot{Q}$
R^*	=	dimensionless thermal resistance $(W_c\ k_f\ L_c R)/H_c$
T	=	temperature (K)
t	=	time (s)
U	=	radial velocity (mm/s)
$\vec{V}$	=	velocity vector (m/s)
V	=	inlet velocity (m/s)
$\bar{V}$	=	mean velocity (m/s)
W	=	width (mm)

Greeks

α	=	thermal diffusivity
μ	=	viscosity of working fluid (N·s/m^2)
ρ	=	density of working fluid (kg/m^3)
ω	=	angular speed (rad/s)

Subscripts

b	=	base
cr	=	cross-linked channel
ch	=	channel
f	=	fluid
i	=	inlet
max	=	maximum
min	=	minimum
o	=	outlet
w	=	wall

Chapter 1 Introduction

Microelectronic devices are now widely used in electronic, mechanical, sustainable energy industries. Its development trend is more integrated designs with compact packaging and higher clock speed. Therefore, the heat produced per unit area increases which now can reach over 100 W/cm^2. To keep their working temperature within the safety range, effective cooling is indispensable. Forced air convection has been the earliest and most common way of cooling. However, the heat dissipation rate is relatively low because of the natural properties of gas. Since the concept of microchannel heat sink was first brought up by Tuckerman and Pease in the early 1980s (Tuckerman et al. 1981), it has been proved to be a very promising cooling technology for semiconductor devices because of its small size, low thermal resistance, small coolant inventory requirement, and small coolant flow rate requirement. A microchannel heat sink usually contains a number of parallel microchannels whose hydraulic diameter ranging from 10μm to 10^3μm. During the past twenty years, the stronger interest among researchers has provided better understanding of design and application of microchannel heat sinks in both single-phase and two-phase fluid conditions. However, most existing researches are conducted under uniform heating condition, while practical applications are characterized by non-uniform heat flux conditions.

In the present work, the cooling performances of microchannel heat sinks are numerically investigated under non-uniform heating conditions and compared to that under uniform heating conditions using the commercial CFD software-Fluent. Three kinds of heat sinks are simulated: cross-linked microchannel heat sink, straight channel micro heat sink and swirl channel micro heat sink. Two types of non-uniform heating conditions are proposed. Chapter 4 presents the cooling performance of the cross-linked microchannel heat sink with local high heat flux conditions. The effects of heat flux and geometric parameters are investigated. The cooling performance of straight micro heat sink is studied under continuously varying heat flux conditions on a rectangular plate in chapter 5. Further optimization on geometry specifications of the heat sink is carried out using Taguchi method in order to improve the cooling performance. In chapter 6, different cross sectional geometries are proposed and compared for the swirl channel micro heat sink under uniform heating conditions. Then, the cooling performance of the swirl channel micro heat sink under continuously varying heat flux conditions is compared to that under uniform heating with the same amount of heat. Conclusions and future works are presented in chapter 7.

Chapter 2 Literature Review

In this chapter, a brief review of open literatures is presented for liquid cooling in microchannel heat sinks. Literatures are categorized into uniform heating conditions and non-uniform heating conditions. Objectives of this work are presented at the end of the chapter.

2.1 Uniform Heating Condition

Microchannel heat sink with uniform heating condition is sufficiently studied both numerically and experimentally. The aspects of research includes materials of solid and liquid phase (Poh et al. 1998; Zhang et al. 2007; Kuan et al. 2008), cross sections (Dickey et al. 2003; Li et al. 2006; Nonino et al, 2010; Asgari et al. 2010), heat sink design concepts (Xu et al. 2005; Liu et al. 2007; Xu et al. 2008; Muwanga et al. 2008; Qu et al. 2008; Fan et al. 2011), and important parameters in heat transfer such as critical heat flux(Revellin et al. 2007) and etc (Chamarthy et al. 2010).

Tuckerman and Pease (1981) brought up the concept of microchannel heat sink as a promising cooling technology for very-large-scale integrated (VLSI) circuits which could generate over 100 W/cm^2 of heat flux. They experimentally tested a water-silicon heat sink with high aspect ratio. The thermal resistance was selected as the criteria of the heat sink's performance. Laminar flow with high flow rate was considered necessary for reducing thermal resistance. The deionized water was used as coolant with a temperature

of 23 °C at the inlet. The tested heat flux was up to 790 W/cm^2 which resulted in a maximum temperature of 71 °C of the heat sink at a high pressure loss of 220 kPa. Thermal resistance decreased when flow rate increased and was under 0.2 °C/W with a flow rate of 2 cm^3/s which was the lowest flow rated tested.

Poh and Ng (1998) numerically investigated the heat transfer phenomenon and thermal resistance with uniform heating in manifold microchannels. ANSYS was used to simulate 16 cases with different geometric parameters of the heat sink. Fluorocarbon Liquid FX-3250 was used as coolant and the flow was laminar. The effects of channel geometries, inlet velocity and wall heat flux value were studied and compared to an analytical model. It was found out that the thermal resistance of the heat sink decreased with the increase of channel length or depth. Yet increase in inlet velocity reduced thermal resistance. The numerical results agreed well with analytical analysis when interfacial effects were not neglected.

Zhang et al. (2007) proposed and experimentally studied three types of microchannel heat sinks: metallic microchannel heat sink (MMCHS), silicon microchannel heat sink (SMCHS), and metallic foam heat sink (MFHS). 21 microchannels were machined on aluminium for MMCHS. The microchannels etched on SMCHSs 1 and 2 were 102 and 152 respectively. MFHSs with porosities of 0.9, 0.8, 0.7, and 0.6 were studied. The manufacturability for the three types of heat sinks was compared. MMCHSs were the easiest to assemble

while MFHSs were proper for large-scale production. MMCHSs had the smallest thermal resistance with low pressure drop because of the natural properties of the metals. SMCHSs provided lowest thermal resistance at sufficient high pressure drop. The heat dissipation could reach 200 W/cm^2 for SMCHSs with a temperature rise of 50°C.

Kuan et al. (2008) studied two-phase flow boiling stability at critical heat flux (CHF) using refrigerant 123 (R-123) and water as coolant. CHFs For both coolants were obtained experimentally. Flow restrictors were found as an effective technology when applied at the inlet for stabilizing the two-phase flow and reduce backflow phenomenon. The test module contained 6 microchannels. It was found that CHF was reduced when using R-123 as coolant. Employing pressure drop elements of 7.7% improved flow boiling stability. A theoretical model was also established for CHF prediction and results showed better agreement.

Dickey et al. (2003) numerically investigated the availability of applying porous media assumption to a microchannel heat sink with triangular “saw tooth” cross section under uniform heating. Results were compared with an analytical solution. It was found that under porous media assumption, good agreement was only in the solid phase for the triangular channel micro heat sink.

Li et al. (2006) optimized the geometric parameters for a rectangular

microchannel heat sink with numerical simulations. Partial dimensionless analysis was used for the 3-D heat transfer model. Uniform heat flux was applied on the bottom surface of the heat sink. Thermal resistance was compared to determine the optimal design. High aspect ratio was found able to reduce thermal resistance since heat transfer area was increased. A channel number of 120 per centimeter was found to be the optimal design with both tested channel height.

Nonino et al. (2010) numerically investigated developing laminar flow in a microchannel heat sink. Six different cross sectional geometries of the channels were proposed which were circular, flat-plate, square, rectangular, trapezoidal, and hexagonal. Fluid properties were constant except the viscosity. Results confirmed that the effect of temperature-dependent viscosity should not be neglected for developing flow. Nusselt number was sensitive to the viscous dissipation and cross-sectional geometries. Yet the situation was the opposite for pressure drop which was mainly influenced by viscosity.

Asgari et al. (2008) developed an approximate asymptotic method to determine the optimum cross section and the corresponding geometry sizes of microchannel heat sink. The optimum design was calculated under a certain pressure drop to obtain maximum heat transfer per unit volume. The model is a function of Bejan number (Bejan et al. (1992)) and dimensional parameters of the channel or duct. The Bejan number is the dimensionless pressure drop

along a channel of length L ($Be = \frac{\Delta P \cdot L^2}{\mu \alpha}$).Ten different cross sections were investigated: parallel plate channel, circular duct, rectangular channel, elliptical duct, polygonal duct, equilateral triangular duct, isosceles triangular duct, right triangular duct, rhombic duct and trapezoidal duct. Results were compared to the solutions obtained using two exact methods which were applied in Yilmaz et al. (2000) and showed fine agreement. Triangular ducts were proved to be the most efficient for maximizing dimensionless heat transfer, followed by trapezoidal and rectangular channels. Circular and quasi-circular ducts (elliptical and polygonal channels) were found not very efficient because they could not fill the space in the package effectively.

Xu et al. (2005) experimentally compared the temperature distribution and heat transfer characteristics of a conventional heat sink with a novel straight channel micro heat sink which had five transverse microchannels to prove the existence of the thermal boundary layer redeveloping mechanism. Both heat sinks had triangular straight channels at the same size. There were 10 parallel channels in the test section whose hydraulic diameter was 155 μm. The area coved by the channels was 21.45 mm×4.35 mm. Five trapezoidal transverse channels were placed evenly along the longitudinal direction. The distance between the centers of each two transverse channels was 3.694 cm, which was almost the thermal developing length for a flow velocity of 1 m/s. High resolution IR technology was used to obtain the module temperature and Nusselt number. The tested ranges for inlet pressure, inlet temperature, mass flow rate, pressure

drop, and heat flux are 1-2 bar, 30-70 °C, 534.79-4132.85 kg/m^{2}s, 10-100 kPa, and 10-100 W/m^2, respectively. The temperature distribution of the conventional heat sink had the horseback shape with a positive gradient in the x-direction. The maximum temperature appeared at x=14 mm. The Nusselt number decreased along the flow direction and decreased especially fast at the entrance region. For the novel heat sink, the horseback shape appeared periodically at each independent zone which consisted of a part of the straight channel and a transverse channel. The low velocity in transverse channels caused the high temperature in the transverse channel which could be reduced by narrower channel width and increase silicon wafer thickness. The Nusselt number also had the periodic shape and was larger in the first region near entrance. The distributions of temperature and Nusselt number verified the existence of thermal boundary redeveloping mechanism.

Liu et al. (2007) designed a fractal network microchannel heat sink for cooling of uniform heat flux on a rectangular plate. Fractal branch net divided each channel (mother) into branches (daughter) which had the same shape but smaller diameter in order to obtain better temperature uniformity without causing very high pressure loss. For arbitrary aspect ratio of rectangular plate, fractal net branch profiles were designed. With certain pressure drop, branching level 7 was discovered to be the best. With fixed heated area, optimal heat sink aspect ratio was 1.87.

Xu et al. (2008) used CFD method for further study of the flow and heat transfer in the conventional and interrupted microchannel heat sink following the experimental work in 2005. The numerical results showed good agreement with the experimental data. The silicon wafer was 30 mm × 7 mm × 0.525 mm and bonded with a 7740 glass cover. There were 10 channels covering 4.35 mm in width in the test module. The geometry size of each longitudinal channel was 21.45 mm × 0.3 mm × 0.212 mm with a hydraulic diameter of 155.4 μm. The trapezoidal microchamber which interrupted the longitudinal channels had the top width of 1.015 mm and bottom width of 0.715 mm. Three-dimensional conjugate heat transfer was computed. The results showed that mass flux and received heat were larger in central channels than edge channels by 0.2% and 2% respectively. This was caused by the heat conduction from center to edge in the wafer. The thermal and hydraulic boundary layers were proved to redevelop at the entrances of each separated zone which consisted of a part of longitudinal channel and a transverse channel. The thermal boundary layer was not fully developed in each zone. The hydraulic boundary layer increased and grew even thicker than the conventional heat sink. The redeveloping mechanism of the thermal boundary layer enhanced heat transfer in the heat sink. Pressure decreased along the flow direction. For the interrupted microchannel heat sink, the pressure drop was larger. It was also found out that there was a jump of pressure distribution at the center each transverse microchannel.

Muwanga et al. (2008) compared flow and heat transfer characteristics

obtained from experiments of a standard heat sink and a cross-linked microchannel heat sink. The heat sink contained 45 channels whose dimensions were 16 mm×0.269 mm×0.283 mm (L×W×H). There were three cross-linked channels with the same width of the straight channel in the heat sink. Two different kinds of support modules were used. Uniform heat flux of 25W/cm^2 was provided to the bottom surface of the heat sink by a serpentine platinum heater. Water and air were both studied as coolant. The inlet and outlet fluid temperature and pressure were measured by thermocouples and pressure transducers, respectively. While thermochromic liquid crystal (TLC) technology was used to obtain fluid temperature in the channels. Results showed that for both coolants, cross-linked channels had minimal effect on pressure drop. Heat transfer measurements were only succeeded for cross-linked microchannel heat sink and only a very slight temperature drop was observed at the last cross-linked channel for all tested Reynolds numbers. It was suggested that this phenomenon was caused by thermal boundary layer redeveloping yet whose effect was minimized by the small width of the cross-linked channels. Further studies of various cross-linked channel width and boundary conditions needed to be carried out.

Qu et al. (2008) performed experiments in order to obtain heat transfer characteristics of single-phase flow in a micro-pin-fin heat sink. The tested heat sink consisted of an array of 1950 staggered square micro-pin-fins which were 0.2 mm × 0.2 mm × 0.67 mm. Inlet flow with the temperature of 30 °C and

60 °C were tested at various velocities. Temperature distribution on the bottom surface was acquired and the results were typical. However, existing correlations had poor accuracy of predicting heat transfer in the paper. Two new correlations were developed and showed much better ability for prediction. Local Nusselt numbers were predicted with a mean absolute error (MAE) of 13.7% and 13.0% respectively for the two new correlations.

Fan et al. (2011) designed a novel swirl channel micro heat sink and its cooling performance was investigated numerically. The module was used for improving cooling of uniform heat flux on a circular flat plate. Swirl channels aligned radially around an expander which was at the center of the module. The swirl channel micro heat sink was tested under different heat fluxes with inlet velocity of 0.5 m/s and 1 m/s. Heat fluxes varied from 10 W/cm^2 to 60 W/cm^2. Compared to straight channels, swirl channels resulted in lower maximum temperature and temperature gradient on the bottom surface. Because the length of flow stream was extended and secondary flow was created by the curvature of the channel. The effects of channel curvature and channel number were also studied. It was found that increase in curvature and channel number enhanced the cooling performance of the heat sink by reducing maximum temperature and improving temperature uniformity. Pressure drop decreased at higher channel number because the velocity in the channel was lower at a certain inlet velocity.

Revellin et al. (2007) developed a theoretical model for prediction of CHF based on the dryout of the liquid film in microchannels. For validation, the results were compared to the experimental data which were R-245f, R-134a, and R-113 in circular channels, and water and R-113 in rectangular channels with a very large subcooling range of 2- 77 °C CHF. Very good agreement was found between the theoretical model and the experiments.

Chamarthy et al. (2010) conducted an experimental work to study temperature non-uniformity of a rectangular microchannel heat sink due to flow maldistribution at the inlet. Ratiometric laser induced fluorescence (LIF) thermometry was used for temperature measurement. The silicon microchannel heat sink consisted of 76 parallel channels which were 0.11 mm in width and 0.371 mm in depth. The wall between two channels was 0.022 mm in width. A thin film heater (12.7 mm × 12.7 mm) provided uniform heating conditions on the heat sink. The Single-dye LIF method was found with less uncertainty than two-dye method. Difference of over 4°C in temperature can be found between center and edges with Reynolds number and heat input to be 40.8 and 49.7 W, respectively. Increase of flow rate would result in larger temperature non-uniformity of the heat sink.

2.2 Non-Uniform Heating Condition

Practical applications are characterized by non-uniform heat flux conditions.

However, the research under non-uniform heating is far from adequate. Non-uniform heating conditions can be realized by irregularity in the aspect of space (Lee 1998; Cho et al. 2003; Gatapova et al. 2008; Revellin et al. 2008; Zhang et al. 2008; Wang et al. 2009; Biswal et al. 2009; Bogojevic et al. 2009; Cho et al. 2010; Sankar et al. 2010) or in the aspect of time (Hetsroni et al. 2001)

Lee (1998) optimized pin array for an integrated, liquid-cooled Insulated Gate Bipolar Transistor (IGBT) power module with a novel approach. Flotherm was used for the CFD simulation. There were six IGBT devices in the module which generating local high heat flux. There were three dies in the upstream region and the other three were in the downstream region. The objects were reducing the temperature magnitude and temperature variation among IGBTs. Based on the temperature distribution and fluid field of the module without pins, rectangular pin arrays were placed directly under the six IGBT dies. The number of pins was increased gradually. Better performance was obtained because convection area was increased and thus heat transfer was enhanced. It was also found that more pins in the downstream region improved temperature uniformity on the module. With pin arrays positioned in 3-2-3 in upstream and 4-3-4 in downstream combinations, the total power of 1200 W was dissipated by the module and the temperature of each die was controlled around 100 °C. Temperature variation among dies was within 1 °C. Comparison with other liquid cooling techniques (pool boiling and cold plate) showed that heat sink

with pin arrays maintained better temperature uniformity of the module.

Cho et al. (2003) experimentally studied the cooling performance of a standard and a cross-linked microchannel heat sink under non-uniform heat flux conditions. Hotspots were placed in the downstream of the heat sinks. High heat flux at the hotspots deteriorated the temperature uniformity of the heat sink. The temperature of the central channels was lower than the edge ones because of the high flow rate. There were difficulties for comparing the temperature distribution with respect to the flow rate under the same heating condition. With hotspot applied to the whole downstream of the channels, cross-linked heat sink shows better cooling performance, while the regular one did if hotspot located at part of the downstream. The temperature uniformity of thermal interface material (TIM) affected the onset of flow boiling and chip temperature distribution drastically, especially with high heat flux at the hotspots. Thinner and more uniform TIM or integrating the microchannels to the thermal die would improve cooling performance.

Gatapova et al. (2008) set up a one-sided two dimensional model to simulate the heat transfer and thermocapillary film deformation for weakly heated films. An inclined channel with its width much larger than its height was considered in this case. The viscous incompressible liquid film flows under the action of the action of gas flow and gravity. A local heater was placed at the bottom of the channel. Under linear velocity profile, high Reynolds number had more

significant influence on convection heat transfer rate. Film thinning can be observed due to thermocapillary forces. The Biot number, which can be a high uncertainty for this case, had a sectional-hyperbolic distribution as a function of the longitudinal axis.

Revellin et al. (2008) improved the one dimensional theoretical model former proposed by Thome et al. (2008) to simulate the flow boiling inside a microchannel under non-uniform axial heat flux condition. The effects of hot spot number, size, location, microchannel diameter, length, mass flow rate, saturation temperature, and the distance between two hot spots were investigated. Three kinds of coolants were used to attain the results. In order to obtain higher dissipation rates at the hotspots, proper microchannel diameter, high mass flow rate and low saturation temperature are required. Furthermore, for local hotspots, the smaller the size, the fewer the amount, the longer the distance between two spots, would lead to better heat dissipation efficiency. The author also proposed a new design of the microchannels, which was to place the flow inlet at the location of hotspot, to decrease the pressure drop when increasing the mass flow rate or reducing the channel diameter.

Zhang et al. (2008) applied the commercial software-Fluent to establish a three dimensional model of microchannel heat sink (MCHS) cooler to simulate the temperature distribution under uniform and non-uniform heating conditions. A traditional uniform channel-width heat sink with water as coolant was studied

in this paper. Comparison between two heating conditions showed that the heat sink has a better heat dissipation character under uniform heating condition. A new type of MCHS with variable channel width was developed to enhance the heat transfer under nonuniform heating condition. With narrower width channel beside the hot spot, the heat dissipation rate increased about 10% at the same inlet velocity.

Wang et al. (2009) continued with Zhang's work (Zhang et al. (2008)) and investigated the temperature distribution and pressure drop of micro channel heat sink (MCHS) coolers using water as coolant and with a heat source at the center of the bottom. Fluent was used to simulate the three dimensional models of three different types of heat sinks, two of which had uniform channel width and one had non-uniform channel width. Results showed that the variable width-channel heat sink maintained the lowest bottom surface temperature at all inlet velocities higher than 0.1 m/s. For uniform width channel heat sinks, with the increase of inlet velocity and channel width, the maximum bottom surface temperature decreased. Maintaining outlet pressure at 1 atm, the pressure distribution for variable width channel heat sink was parabolic with 0.3 bar higher pressure in the center than the edge at 0.5 m/s inlet velocity. While it was almost uniform for equivalent width channel heat sinks. The largest pressure drop of the variable width channel heat sink was between the other two equivalent width channel heat sink, which increased with the inlet velocity.

Biswal et al. (2009) optimized a rectangular microchannel heat sink but with more parameters such as the position and size of heat source, thickness and material of substrate, flow rate and etc. When studying the effects of position and size of heat source, heat source area that was smaller than heat sink footprint was simulated thus non-uniform heating with hotspots heat flux conditions were generated. When heat sink was under non-uniform heating, channel width was at 0.1 mm and height was at 0.3 mm. Two types of non-uniform heating were simulated. First, heat source had the same width as the heat sink and its length reduced from the length of the heat sink to half of its value. Temperature rise and thermal resistance decreased by up to 30% in this process. Second, heat source coverage increased from 4% to 100% with the center placed at the center of the heat sink. Total thermal resistance was reduced from 3 to 0.324 °C/W.

Bogojevic et al. (2009) studied flow boiling in an experimental work under non-uniform heating conditions in a micro channel heat sink. The temperature distribution, pressure drop and two-phase flow instability were investigated with three different heating conditions which had hotspot placed in upstream, middle and downstream region, respectively. Characteristic fluctuations of temperature and pressure in the channels were observed. The highest amplitude of temperature for each hotspot position appeared in the following region for upstream and middle hotspots; while it was in the upstream region for downstream hotspot. At the flow rate of 17 g/min, downstream hotspot resulted

in better temperature uniformity in transverse direction but worse temperature distribution in axial direction. Higher heat flux at the hotspots also caused more significant temperature non-uniformity in the transverse direction. The highest pressure drop appeared when the hotspot was placed in the upstream region.

Cho et al. (2010) performed a numerical modeling and simulation to investigate the effect of header geometry on flow distribution in the microchannel heat sink under three different non-uniform heating conditions. Chisholm's coefficient method and homogenous method were applied to simulate the two-phase flow in the channels without considering the subcool and superheat region. A geometric parameter "n" of the header shape was defined. n=4 was found to be optimal in all cases in order to obtain reasonable uniformity of flow distribution and relatively low pressure drop with affordable area ratio. It was also found that local hotspot would cause significant deviation of mass flow in the channel near it.

Sankar et al. (2010) developed a Fortran code to investigate the heat transfer of the incompressible Boussinesq fluid in a vertical cylindrical cavity under the influence of modified Rayleigh number, radii ratio, and aspect ratio. There were two flush-mounted heater placed on the inner wall of the cavity which provide constant heat sources. The length of each heater and the non-heated portion of the inner wall were fixed at 0.2 L. The outer wall was kept at a lower temperature while the top and bottom wall were adiabatic. The model was

validated by comparing the average Nusselt number with former benchmark cases. The simulation results revealed that the maximum heat transfer rate usually took place at the bottom heater. The average Nusselt number which presented the heat transfer rate was found to be in direct ratio with modified Rayleigh number and radii ratio while in inverse ratio with aspect ratio. Under low modified Rayleigh number and high aspect ratio, the temperature distribution of the flow appeared to be a bi-cellular form with the center at the parallel location of each heater.

Hetsroni et al. (2001) conducted an experimental study of two-phase flow pattern, temperature distribution and pressure drop in microchannels when flow boiling occurred. Uniform and non-uniform heating conditions were realized by providing constant or timely irregular heat flux to the heated wall. Several prototypes were designed, manufactured and tested. Two types of inlet and outlet designs were specially studied. In this work, with different geometry of micro channels, two periodical flow patterns were observed in flow visualization- annular flow and dry zone which accompanied by hotspots and rewetting and wetting of the surface. Non-uniformity of temperature distribution was caused by flow boiling on the heated bottom of test modules under uniform heating condition, and was enhanced by non-uniform heating. It was also found that the pressure drop increased with the heat flux when maximum surface temperature is over 100 °C, nominally two-phase flow situation.

2.3 Motivation

Under uniform heating conditions, the angles of research in microchannel heat sink have ranged from geometries, materials and heat fluxes to heat transfer mechanism, flow patterns and phase change behaviors. As the study of microchannel heat sink under uniform heating conditions is approaching to a mature level, the research of cooling performance of heat sinks under non-uniform heating is still in the primary stage. However, in real applications, uniform heating conditions are not common; yet non-uniform heating is more practical. For example, non-uniform heating conditions with hotspots can be found on CPUs; continuously varying heat flux can be generated by concentrated photovoltaic cells or laser beams. More efforts should be devoted to the study of non-uniform heat flux conditions. For non-uniform heating, the heat fluxes are changing either with space or time, therefore creating numerous variations of heating conditions. Current investigations are mainly focusing on non-uniform heating conditions with hotspots. Effects of continuously varying heat fluxes require more attention.

The motivation of this work is to extend the study of microchannel heat sinks under non-uniform heating conditions. Different non-uniform heating conditions other than hotspots need to be investigated. In the present work, non-uniform heating conditions including heat flux with hotspots and a novel continuously varying heat flux are applied to the microchannel heat sinks. The

effects of heating conditions are studied to enhance the cooling performance of the microchannel heat sinks.

2.4 Objectives

The cooling performance of the microchannel heat sinks under non-uniform heating conditions are to be discussed in the following work. Numerical simulations will be performed to obtain the results. The objectives of this work are as follows:

1. Propose two types of non-uniform heating conditions which are heat flux hotspots and continuously varying heat fluxes, as well as an approximate method for simulation of the continuously varying heat flux.

2. Apply cross-linked microchannel heat sinks for cooling of heat flux with hotspots. Study the effects of the positions and the amount of heat fluxes of hotspots on heat sink cooling performance. Conduct geometric optimization by modifying the cross-linked channel width and positions.

3. Propose straight channel micro heat sink for the continuously varying heat flux on a rectangular plate. Investigate the effects of heat fluxes that changing perpendicular or along flow directions in order to enhance cooling performance. Optimize the heat sink geometry Taguchi method for future design direction of heat sinks under non-uniform heating.

4. Apply a novel swirl channel micro heat sink which is designed by Fan et al. (2010) for the cooling the continuously varying heat flux on a circular plate. Compare different cross sectional geometries of the channels under uniform heating conditions in order to improve the heat sink performance. Study the effects of two types of continuously varying heat fluxes on the heat sink cooling performance.

Chapter 3 Numerical Methodology

3.1 CFD Modeling

CFD numerical simulation has been proved to be effective and promising in predicting fluid characteristics in micro scale. In this work, the numerical simulations are performed with the commercial CFD software – Fluent. The following assumptions are made for the simulation:

1) heat transfer and fluid flow are in steady state;
2) fluid properties are dependent of temperature;
3) solid properties are constant;
4) radiation and convection heat losses through top and side walls are neglected;
5) neglect viscous dissipation.

3.1.1 Governing Equations

For the present study, heat transfer is conjugated conduction and convection in the whole module. Flow is considered to be incompressible, steady and laminar in the heat sink. Based on the above mentioned assumptions, the Navier-Stokes equations are reduced as following:

Continuity equation:

$$\nabla(\rho\vec{V}) = 0 \tag{3.1}$$

where ρ is the density of the fluid; $\vec{V}$ is the velocity vector.

Momentum equation:

$$\vec{V} \cdot \nabla(\rho\vec{V}) = -\nabla\vec{P} + \nabla(\mu\nabla\vec{V}) \tag{3.2}$$

where P is the pressure; μ is the viscosity of the fluid.

Energy equations:

$$\vec{V} \cdot \nabla(\rho C_p T_f) = \nabla(k_f T_f) \text{ (in liquid)} \tag{3.3}$$

$$k_w \nabla^2 T_w = 0 \text{ (in solid)} \tag{3.4}$$

where C_p is the thermal capacity; k_f and k_w are thermal conductivity of fluid and solid respectively; T_f and T_w are the temperature of the fluid and solid respectively.

3.1.2 Boundary Conditions

The inlet is set as velocity inlet. Constant velocity is applied to the fluid at the inlet and the direction of the velocity is normal to boundary. The outlet is assigned as pressure outlet whose gauge pressure is zero. Water is used as coolant whose properties are dependent of the temperature. A set of polynomial

equations (Jayakumar et al. (2008)) are used for modeling temperature dependent water properties in Fluent. The parameters are listed in Table.3.1. Flow is single-phase and laminar in the channels. No-slip boundary condition exists at inner walls. Side walls are adiabatic except the bottom surface which is supplied with heat flux. The SIMPLE scheme is used for the computation of pressure-velocity coupling. The second-order-upwind scheme is used for the momentum and energy conservation equations. The pressure conservation equation is calculated under standard scheme. For the under-relaxation factors, default values are used. The absolute convergence criterion is 10^{-6} for continuity and velocity equations and 10^{-9} for energy equation.

Table. 3.1 Polynomial coefficient of thermal-dependent properties

	A_1	A_2	A_3	A_4	A_5
ρ	1227.8	-3.0726	0.011778	-1.56E-05	
k_f	-1.0294	0.010879	-2.26E-05	1.54E-08	
C_p	4631.9	-1.478	-3.108E-3	1.11E-05	
μ	0.33158	-3.752E-3	1.60E-05	-3.06E-08	2.19E-11

3.1.3 Approach Method for Continuously Varying Heat Flux Conditions

As mentioned, continuously varying heat flux conditions can be found on concentrated photovoltaic cells. The sketch of the heat flux on a cylindrical collector projected by the concentration device can be found in references

(Prapas et al. (1988); Wang et al. (2010); He et al. (2011)). The heat fluxes can be considered to vary in one single direction. However, the concrete expression of the heat flux has not been specified. Therefore, the heat flux distributions proposed in this thesis are presumed and have the similar shape with the ones in the references.

In order to simulate the continuously varying heat flux condition, the heating area has been divided into multiple zones. The sketch of simulation method is also shown in Figure.3.1. Assume heat flux changes along x axis and has an expression:

$$q1 = 80 \times e^{-x} + 20 \tag{3.5}$$

The heat flux distribution curve is divided and the average value of heat flux in each zone can be determined by:

$$\dot{q}_j = \frac{\int_{A_j} \dot{q}(x)dx}{A_j}, \quad j = 1, 2, 3 \ldots N \tag{3.6}$$

where, $\dot{q}_j$ is the average value of heat flux in the j^{th} zone; A_j is the area of the j^{th} zone; $\dot{q}(x)$ is the assumed heat flux generated on the surface. The error between the simulated and practical heat flux can be evaluated by,

$$E_j = \left|\frac{\dot{q}_j - \dot{q}(x)}{\dot{q}_j}\right| \tag{3.7}$$

where, E_j is the error in the j^{th} zone. In this work, the error in all zones is maintained below 15%. Hence, if heated area is rectangular, the width of each

zone can be determined by solving the following equation:

$$E_j = \left| \frac{\int_{x_j}^{x_{j+1}} \dot{q}(x)dx - \dot{q}(x)}{\int_{x_j}^{x_{j+1}} \dot{q}(x)dx} \right| = 15\% \pm 1\% \quad (3.8)$$

If the heated area is circular, Equation.3.6 can be transformed to:

$$E_j = \left| \frac{\int_{x_j}^{x_{j+1}} \dot{q}(x)\cdot 2\pi x dx - \dot{q}(x)\cdot \pi x^2}{\int_{x_j}^{x_{j+1}} \dot{q}(x)\cdot 2\pi x dx} \right| = 15\% \pm 1\% \quad (3.9)$$

where x_j and x_{j+1} are the left and right coordinates of the j^{th} zone. The value of x_1 is set to zero. Then, the value of x_2 is calculated based on the Equation.3.8 or Equation.3.9. The last zone may not satisfy the condition because of the size limit of the heat sink, but the error is lower than 15%. Matlab is used to solve the equations and to obtain all coordinates.

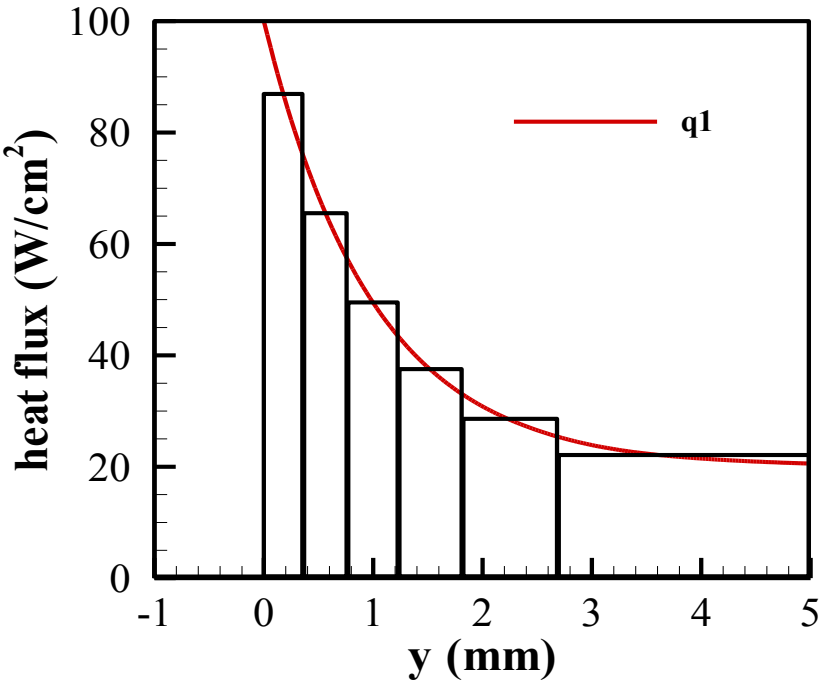

Figure. 3.1 Simulation of continuously varying heat flux

3.1.4 Comparison with Experimental Work

The results of the mesh system and numerical model are compared to experimental data from existing literature (Zhang et al. (2007)). In the experimental work, the test module is a conventional straight channel micro heat sink with 21 channels. Half of the test module is simulated due to symmetric geometry. The dimensions of the computational domain are summarized in Table.3.2. The sketch of the domain is shown in Figure.3.2. Two cuboid plenums are placed at the two ends of the channels. The inlet and outlet are two holes at the middle of the plenums whose diameters are both 3.4mm. Aluminum and water are chosen as materials for solid and fluid, respectively. The effective thermal conductivity of solid and fluid phase is used in the simulation. The tested flow rate varies from 0.07 L/min to 0.4 L/min. Flow is laminar in the heat sink. At the center of the bottom surface of the heat sink, input heat of 60 W is applied uniformly to a square surface area of 12 mm×12 mm. Structured mesh system is used to mesh the computational domain.

The thermal resistance is calculated for different flow rate by the following equation:

$$R = \frac{(T_{max} - T_i)}{\dot{Q}} \tag{3.10}$$

Where T_{max} is the maximum temperature of the heat sink; T_i is the inlet temperature of the fluid; $\dot{Q}$ is the total heat input.

The thermal resistance of the whole module over corresponding pressure drop

is compared between numerical and experimental results. The numerical results are within 15% error of the experimental data as shown in Figure.3.3. The error is resulted from the different method to obtain the junction temperature used between this work and the literature.

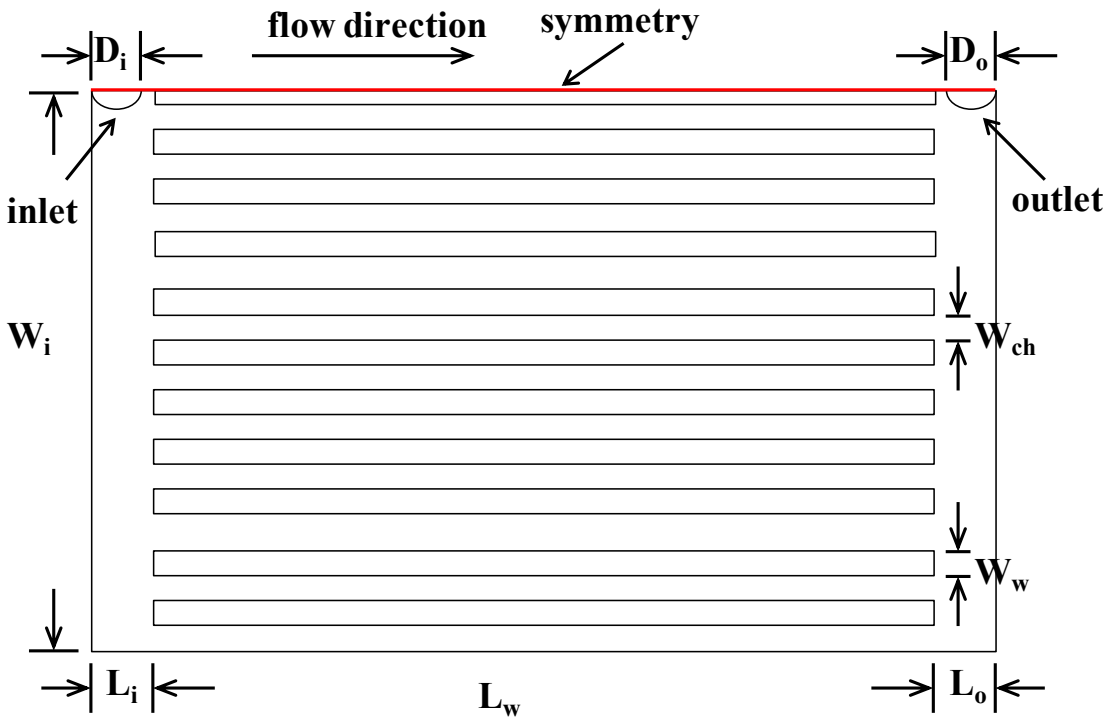

Figure. 3.2 Sketch of geometry

Table. 3.2 Dimensions of the geometry (unit: mm)

Parameter	Dimension
L_i	5
L_w	15
L_o	5
W_i	6.1
W_w	0.4
W_{ch}	0.2
H_{ch}	2
H_b	0.8
D_i, D_o	3.4

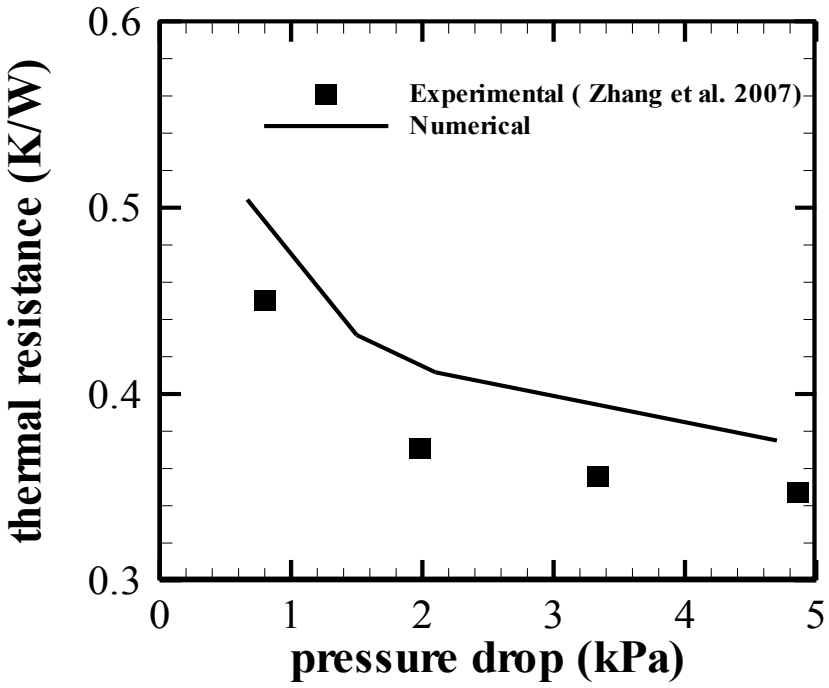

Figure. 3.3 Comparison of the numerical results with experimental data of Zhang et al. (2007)

3.2 Optimization Methodology

In this section, the general procedure of optimization using Taguchi method is presented. More detailed description and results are shown in Chapter 5.

In order to optimize the geometry of the heat sink and to study the effects of geometry on heat sink performance, the Taguchi method is used to determine the optimal geometry sizes. The Taguchi method was developed by Dr. Genichi Taguchi of Japan for investigation of effects of parameters. This Design of Experiment (DOE) method involves using orthogonal arrays to organize parameters selected for optimization in order to reduce the amount of experiments. The procedure of the method is described in the flowchart, shown

in Figure.3.4. In the optimization process, the first step is to select the design variables, and their ranges of variation and the objective function. For the straight channel micro heat sink, the height and width of the channels, the height of the base and the width of the fins are chosen to be the optimization parameters. Maximum temperature is selected to be the objective function. Then, according to the Taguchi method, the corresponding orthogonal array is picked and test matrix is built. Geometries in the test matrix are simulated and evaluated by CFD to obtain results of the object function. The signal (product quality) to noise (uncontrollable factors) ratio (S/N) is calculated for the object function to determine the most sensitive parameters and the optimal design point. Because the product quality is best achieved when the product is immune to noise (uncontrollable factors), the S/N ratio of the object function should be high.

For the case of minimizing the performance characteristic which is to reduce maximum temperature of the heat sink, the S/N (dB) should be calculated by the following equation:

$$\eta = -10log_{10}\sigma^2 \tag{3.11}$$

where σ^2 is the square of standard deviation of the maximum temperature of the bottom surface which is determined as follows:

$$\sigma^2 = \frac{1}{n}\sum_{i=1}^{n}(T_i - T_\infty)^2 \tag{3.12}$$

where n is the number of nodes on the bottom surface defined by the mesh;

T_i is the temperature of each node; T_∞ is the minimum temperature that the node can reach.

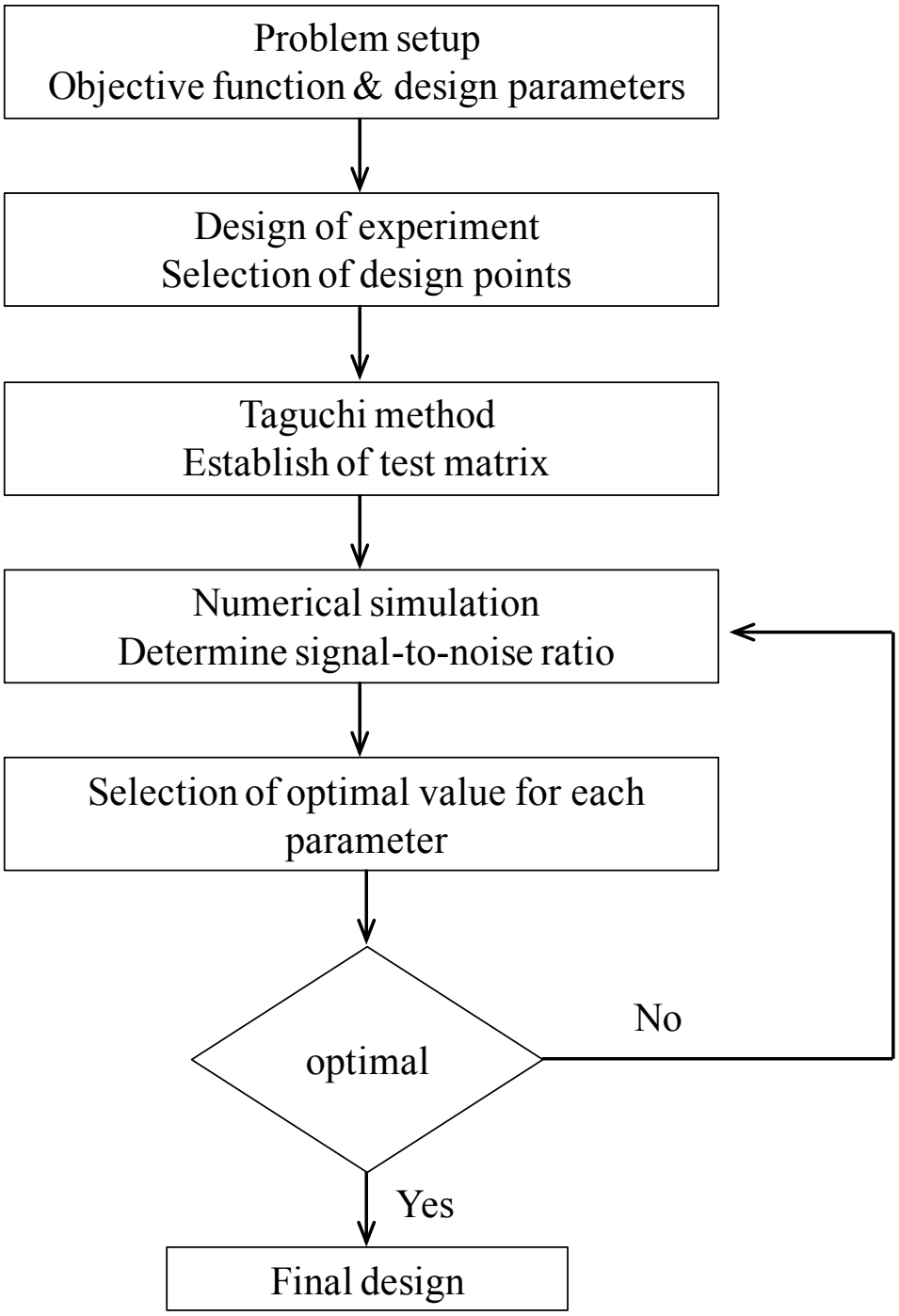

Figure. 3.4 Flowchart of optimization process

Chapter 4 Cooling Performance of Cross-linked Micro Channel Heat Sinks with Hotspots

In this chapter, cross-linked channels are added to standard straight channel heat sink which has local hotspots as heat source on its bottom surface. The cooling performance of the cross-linked micro heat sink is studied and compared to that of the straight channel micro heat sink. The effects of positions and the heat fluxes on local hotspots are studied for straight channel micro heat sink. The effects of geometric parameters, such as the width and positions of cross-linked channels are investigated under different heating conditions and various inlet velocities as well.

4.1 Module Specifications and Test Matrix

The geometric dimensions of half of the test module are shown in Figure.4.1. Figure.4.1 (a) and (b) give the top and section view of heat sink consisting of two cross-linked channels, respectively. Figure.4.1 (c) shows different positions of cross-linked channels. In the figure, only the positions of cross-linked channel in the upstream are shifted but in simulation, both of the two cross-linked channels have the same position reletive to the hotspots. The whole test module is 14 mm in length, 10.75 mm in width and 2 mm in height.

Half of the module is selected as computational domain. The material of the 0.5 mm-high substrate is chosen to be silicon, whose density, specific heat capacity and thermal conductivity are set to be 2329 kg/m^3, 750 J/(kg·K), and 148 W/(K·m), respectively. The inlet and outlet holes are located at the middle of the module, with a diameter of 1 mm. A 2 mm long isosceles trapezoidal header with bottom inner angles of 45° lies in front of the channels. At the exit of the channels, there is a collector which has the same size of the header to guide the flow to the outlet. There are 22 microchannels in the module that are 10 mm in length, 0.25 mm in width and 0.5 mm in height. The wall between each two channels is also 0.25 mm wide. Cross-linked channels have the same depth with the microchannels. Three cross-linked channel width (W_{cr}): 0.5 mm, 1 mm and 2 mm are selected. Cross-linked channels are placed right in front of, above, and after the hotspots. The sizes of upstream hotspot (HS1) and downstream hotspot (HS2) are both 2 mm×5 mm.

For the test matrix, first, as in Table.4.1 the effects of the positions and heat fluxes on hotspots are studied on straight channel heat sink and cross-linked channel heat sink with transverse channels above the center of the hotspots with inlet velocities of 0.5 m/s and 1 m/s. Four heating conditions are applied to the bottom surface of the straight channel heat sink. They are described as following:

1. upstream hotspot by supplying 100 W/cm^2 heat flux to HS1

2. downstream hotspot by supplying 100 W/cm^2 heat flux to HS2
3. supplying 100 W/cm^2 heat flux to HS1 and secondary 50 W/cm^2 heat flux to HS2
4. supplying 100 W/cm^2 heat flux to HS2 and secondary 50 W/cm^2 heat flux to HS1

Second, the effect of geometric parameter W_{cr} is also studied under the four non-uniform heating conditions. For cross-linked heat sink with W_{cr}=0.5 mm, under heating conditions 1 and 3 mentioned above, the positions of the cross-linked channels are shifted to investigate the effects on heat sink cooling performance with inlet velocities of 0.5 m/s and 1 m/s. Three different positions of the cross-linked channels are tested which are shown in Figure.4.1. Dimensionless distance L^* from x-axis to the center of the cross-linked channels is used to present their positions. L^* is calculated by:

$$L^* = y/(D_{h\,c} \cdot Re) \tag{4.1}$$

where y is the coordinate of the center of cross-linked channel; $D_{h\,c}$ is the hydraulic diameter of the microchannels; Re is the Reynolds number at the inlet. L_1^* and L_2^* represent the dimensionless positions of the upstream and downstream cross-linked channels, respectively.

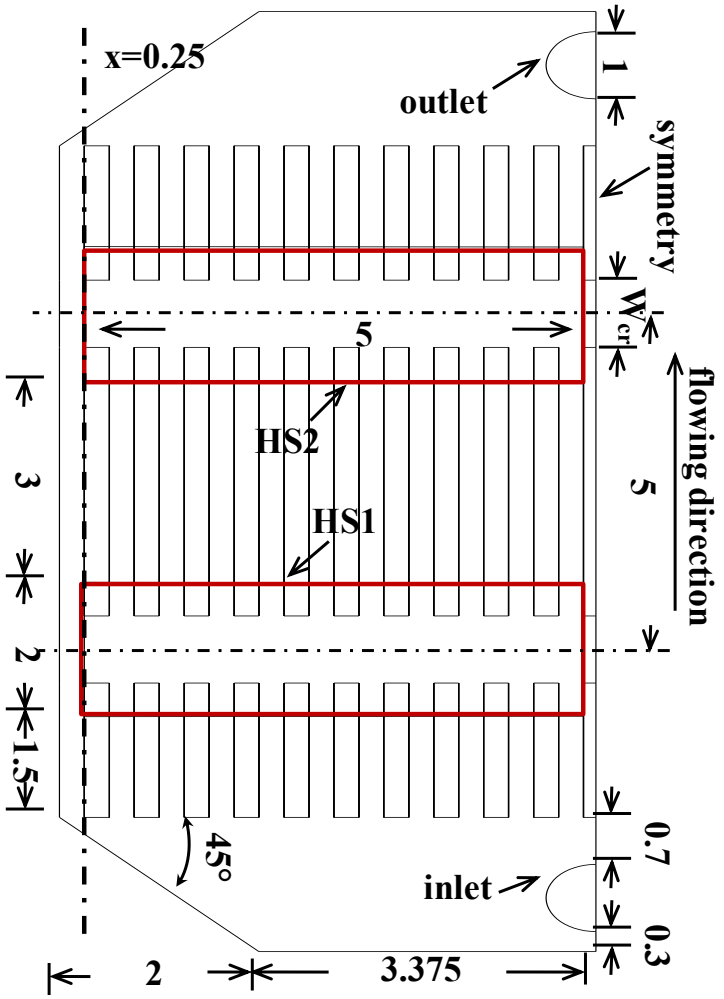
x=0.25
outlet
symmetry
1
W_{cr}
5
HS2
HS1
flowing direction
5
3
2
1.5
45°
inlet
0.7
0.3
2
3.375

(a)

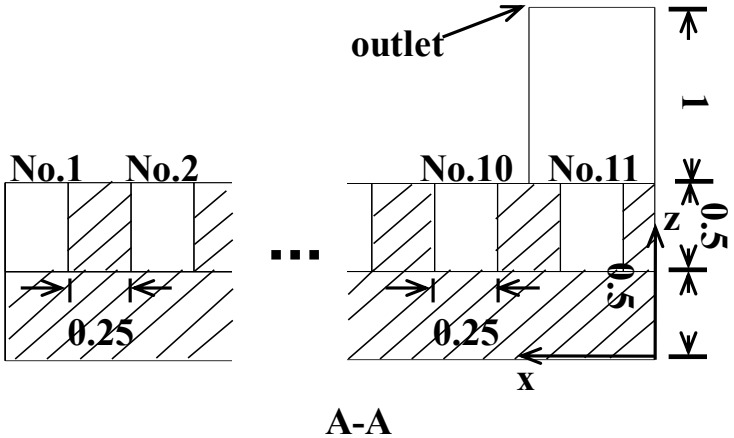
outlet
1
No.1
No.2
No.10
No.11
0.5
z
0.25
0.25
x
A-A

(b)

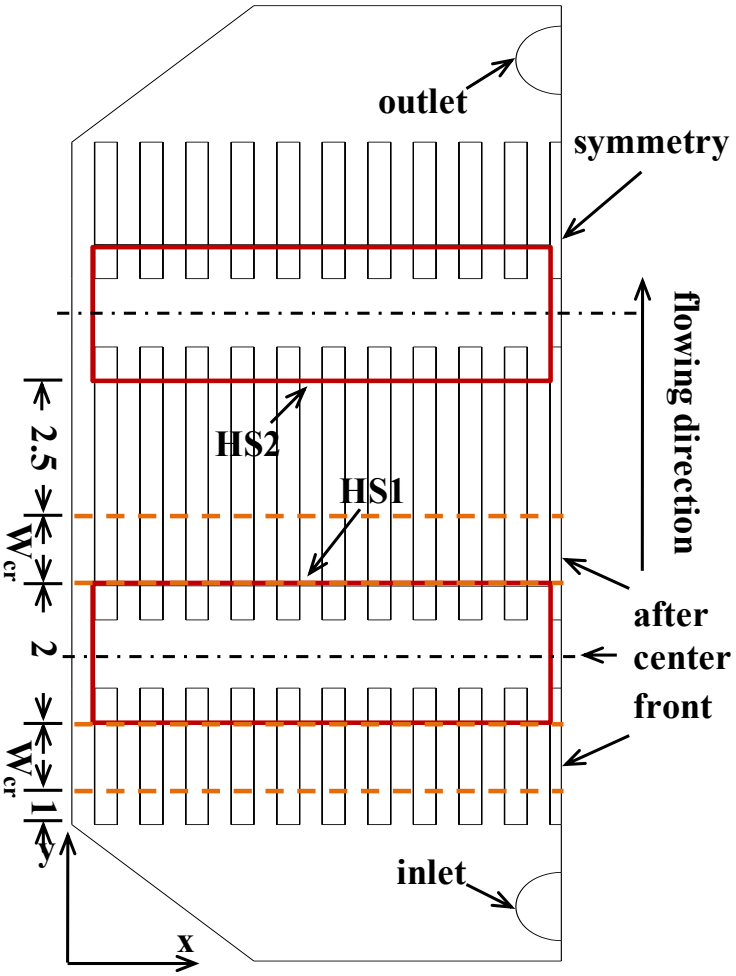

(c)

Figure. 4.1 Geometric dimensions of half of the test module (a) top view (b) section view (c) positions of cross-linked channel (all dimensions are in mm)

Table. 4.1 Test matrix

Case	W_{cr}	$L_1^*, L_2^* \times 10^3$	V (m/s)	Back-ground (W/cm^2)	Hotspot (W/cm^2)	
					One hotspot	Two hotspots
STR	0	None	0.5, 1	10	1. HS1 = 100 HS2=10 2. HS1=10 HS2 = 100	3. HS1=100 HS2=50 4. HS1=50 HS2=100
CR-1	0.5	27, 57	0.5			
CR-2	1					
CR-3	2	13.5, 28.5	1			
CR-1-f	0.5	36, 66	0.5		1. HS1 = 100 HS2=10	2. HS1=100 HS2=50
		18, 33	1			
CR-1-a		18, 48	0.5			
		9, 24	1			

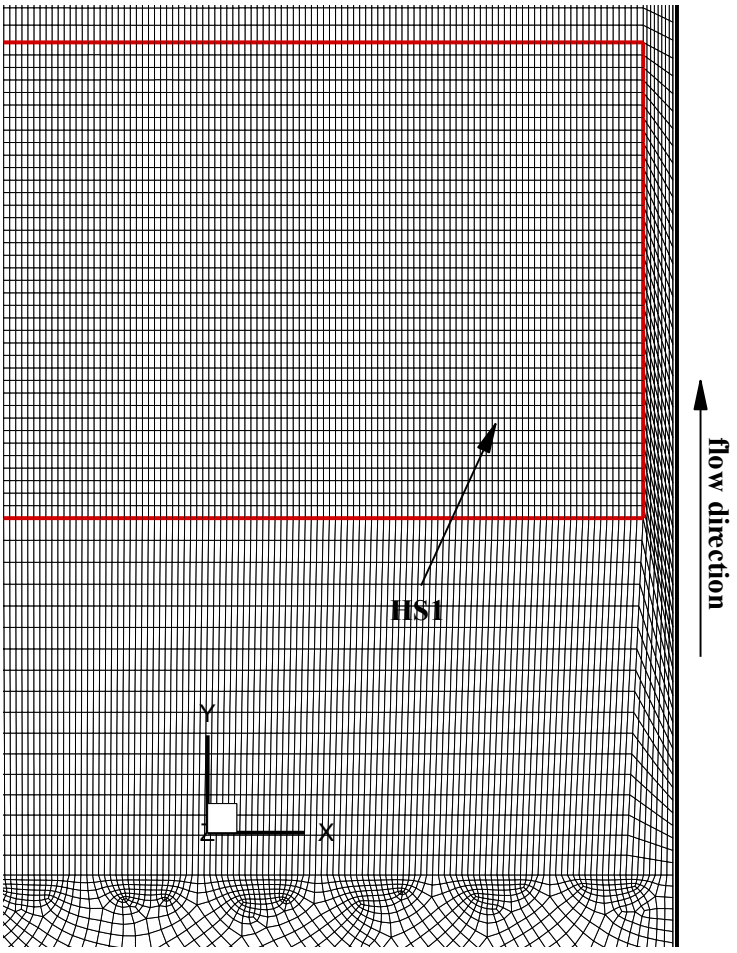

Figure. 4.2 Partial mesh from bottom view of the computational domain

4.2 Mesh Independence

Structured mesh system is used for meshing the computational domain. A portion of the mesh is shown in Figure.4.2. The mesh at the hotspot zone is finer than the rest of the bottom surface. Mesh independence is analyzed for the straight channel heat sink with 100 W/cm^2 applied to HS1 and 50 W/cm^2 to HS2. The inlet velocity is 1 m/s. Results for mesh system with 0.14M, 0.9M and 1.9M cells are compared in Figure.4.3. Figure 4.3 shows temperature distribution along the line at x=0.25 mm as shown in Figure.4.1(a) which is under the edge of channel No.1 and passing the hospot zones. The results are almost identical for meshes with 0.9M and 1.9M cells. Therefore, the grid system with 0.9M cells is used for the computational domain.

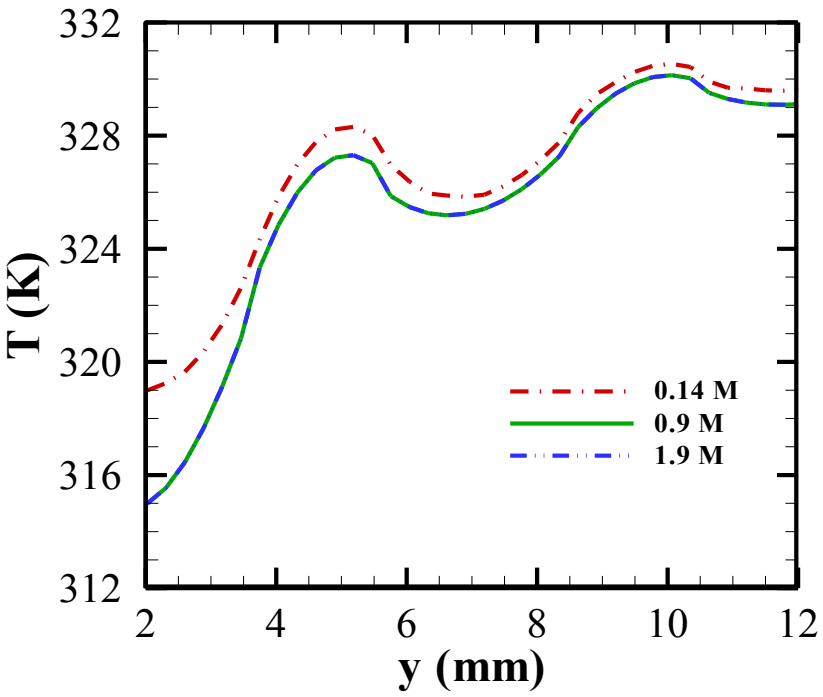

Figure. 4.3 Temperature distribution on the line at x=0.25 mm

4.3 Results and Discussion

4.3.1 Effects of Positions and Heat Fluxes of Hotspots

Straight channel micro heat sink is used to study the effects of positions and heat fluxes on hotspots. The temperature distribution on the center line of the bottom surface under both inlet velocities can be found in Figure.4.4 and 4.5. The increase of inlet velocity reduces the temperature at both hotspots because heat transfer is enhanced in the channels. There are temperature surges at the hotspots due to the very high heat flux applied on them. For one hotspot condition, under both inlet velocities, maximum temperature and temperature difference on the bottom surface are lower when the hotspot is placed in the upstream region. This is because the fluid temperature is much lower above the upstream hotspot zone than that above the downstream hotspot zone. By adding a secondary hotspot on the bottom surface, the maximum temperature still appears in the hotspot zone because of the higher heat flux. Fluid is heated by the increased total power to a higher average temperature therefore the maximum temperature of the heat sink rises. When heat flux at HS1 is higher than HS2, lower maximum temperature and temperature difference on the bottom surface can be obtained rather than that of the opposite situation. Although the hot fluid enters the downstream hotspot zone, by supplying smaller heat flux at HS2, the peak value of the temperature will reduce. And eventually causes smaller temperature difference on the surface.

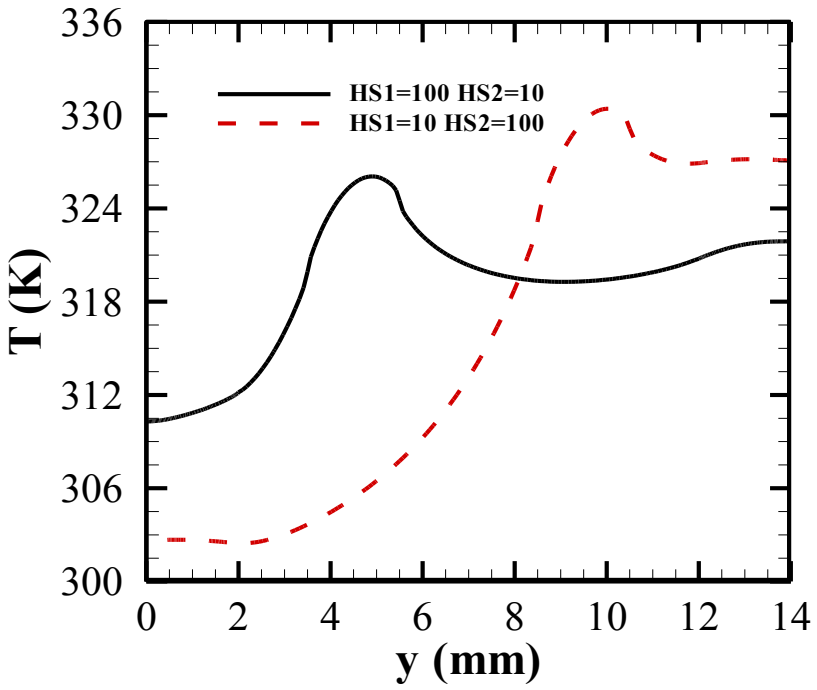

(a) V= 0.5 m/s

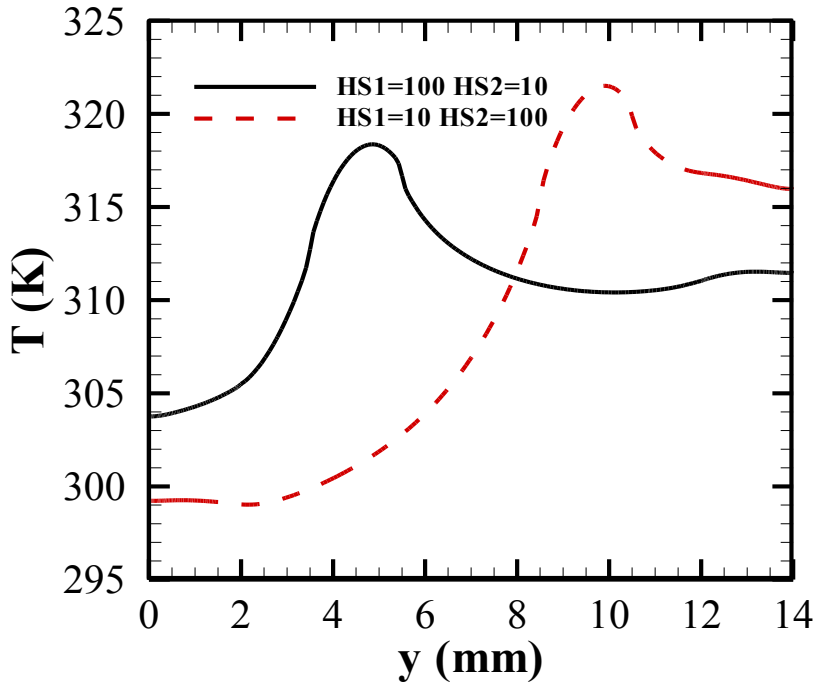

(b) V=1 m/s

Figure. 4.4 Temperature distribution on the center line of the bottom surface with one hotspot (a) V=0.5 m/s (b) V=1 m/s

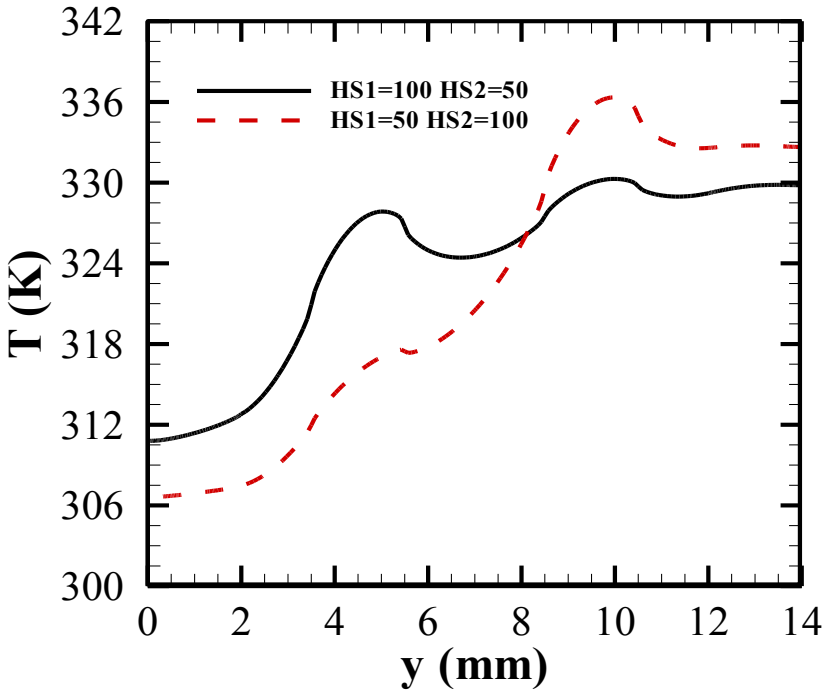

(a) V=0.5 m/s

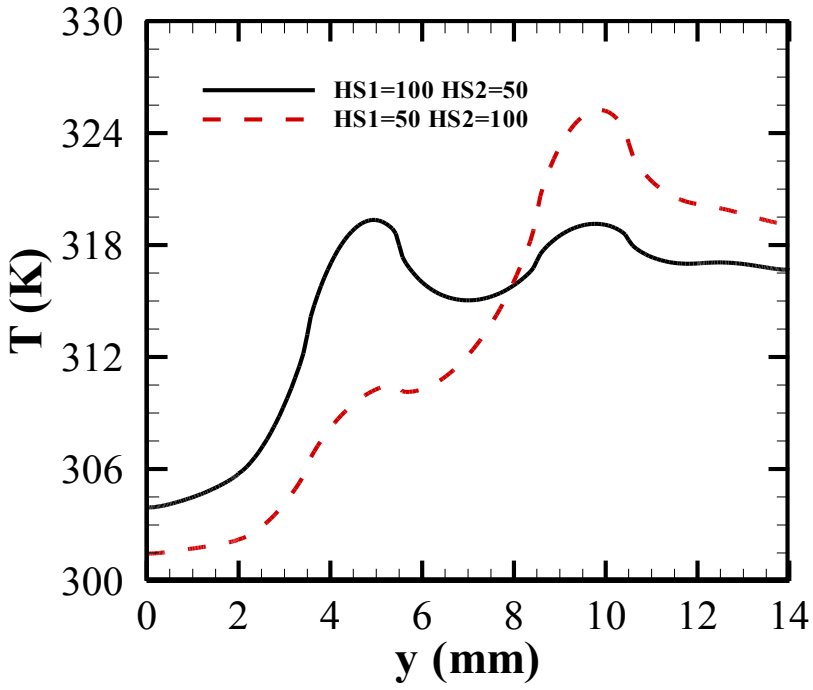

(b) V=1 m/s

Figure. 4.5 Temperature distribution on the center line of the bottom surface with two hotspot (a) V=0.5 m/s (b) V=1 m/s

4.3.2 Effects of W_{cr} of Cross-linked Channel on Temperature Distribution

Figure.4.6 presents the temperature distribution on the bottom surface of the straight and cross-linked channel heat sink with inlet velocity of 1 m/s with two hotspots. Results show that for both heating conditions, the cross-linked channel above HS1 raises the hotspot temperature which is likely caused by the reduction of both heat transfer surface area and the velocity of the flow. However, there is a decrease in temperature after HS1 and at HS2 due to thermal boundary layer redeveloping mechanism at the exit of the upstream cross-linked channel. Temperature uniformity is improved at both hotspots because flow mixing occurs in cross-linked channels as shown in Figure.4.7. The variation of water temperature and properties in different channels leads to a velocity in x axis in the flow; therefore interchannel mixing can be observed.

Figure.4.8 compares the temperature profiles on the centerlines of HS1 and HS2 for the three cross-linked channel geometry designs. Maximum temperature of the heat sink rises drastically when W_{cr} increases. This is induced by a decrease in heat transfer surface area and fluid velocity at the cross-linked channel zone with large W_{cr}. As a result, heat transfer is reduced which results in higher hotspot temperature. At HS1, temperature profiles for all three designs have the almost identical pattern. Larger difference in fluid temperature and water properties at the entrance of downstream cross-linked

channel leads to enhanced flow mixing intensity that improves temperature uniformity at HS2 rather than at HS1. Meanwhile, flow mixing intensity is not greatly affected by W_{cr}, so that minimal effect on temperature uniformity is obtained.

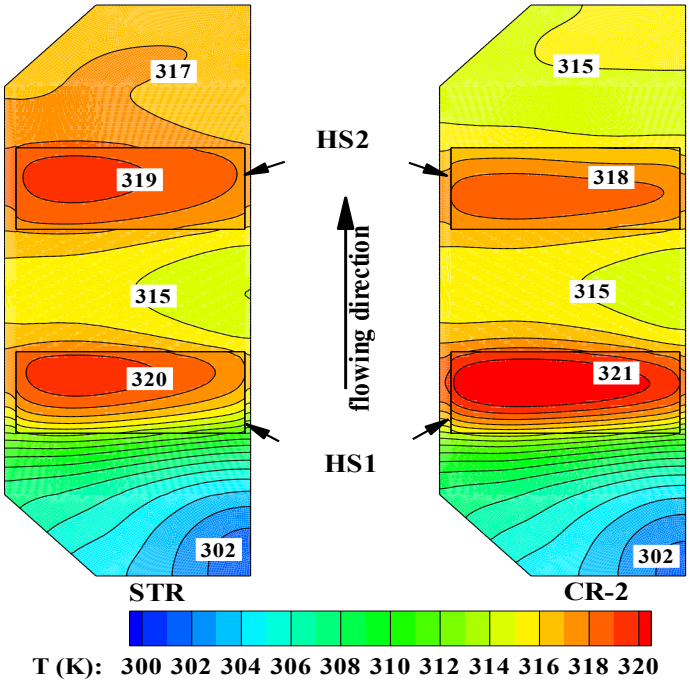

(a) HS1=100, HS2=50

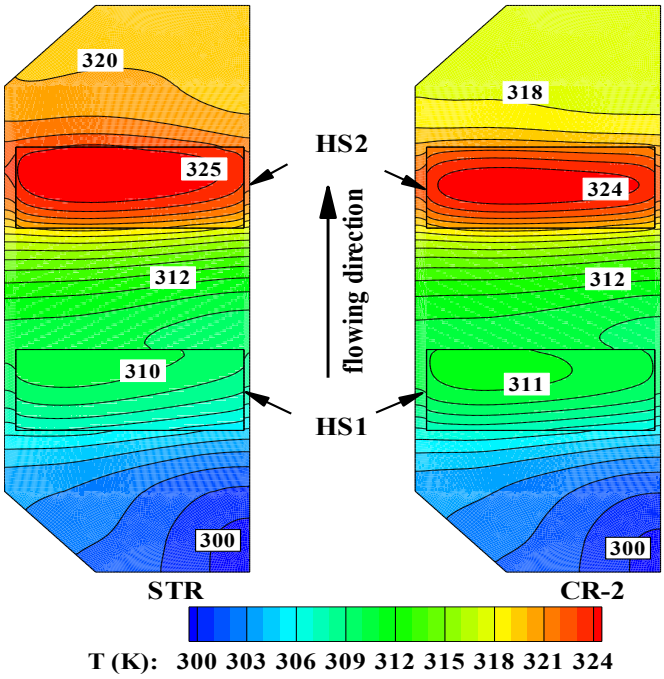

(b) HS1=50, HS2=100

Figure. 4.6 Temperature distribution on bottom surface at inlet velocity of 1 m/s under (a) HS1=100, HS2=50 (b) HS1=50, HS2=100

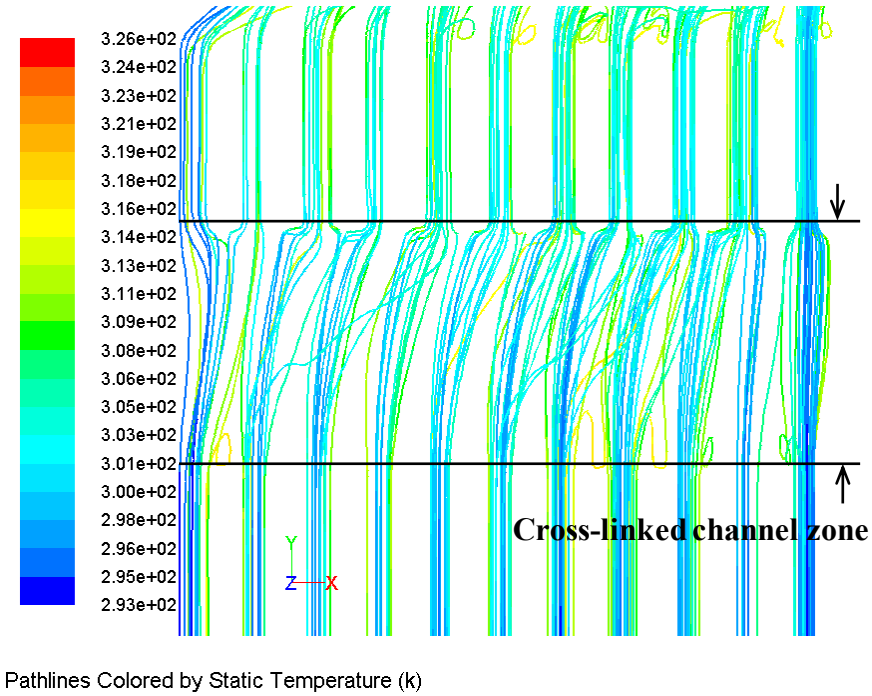

Figure. 4.7 Flow mixing: pathlines in downstream cross-linked channel with inlet velocity of 1 m/s with HS1=100 W/cm^2

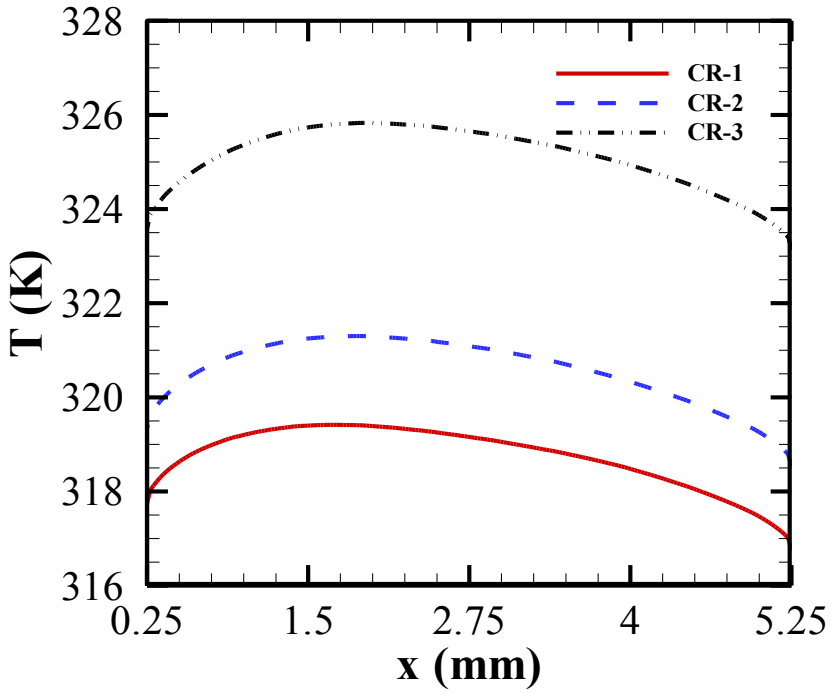

(a) HS1 centerline

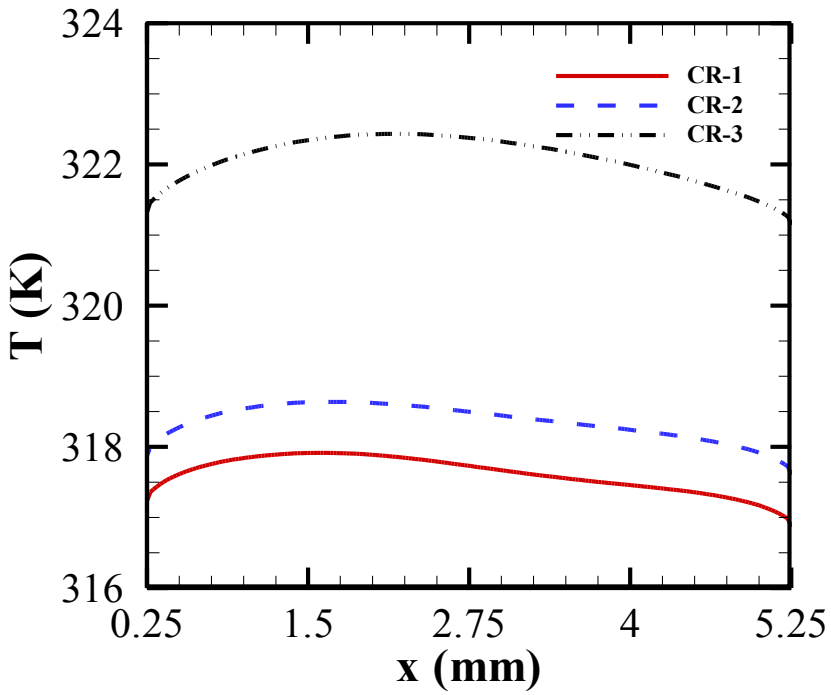

(b) HS2 centerline

Figure. 4.8 Temperature profile on centerlines of hotspots for cross-linked channel heat sink with inlet velocity of 1 m/s with HS1=100 W/cm^2 (a) HS1 centerline (b) HS2 centerline

4.3.3 Effects of Positions of Cross-linked Channels

As discussed above, the maximum temperature and temperature difference are smaller with an upstream hotspot only or HS1 is subjected to a higher heat flux than HS2. As a result, the effect of the positions of cross-linked channels is studied under the two heating conditions. Dimensionless distance L^* from x-axis to the center of the cross-linked channel is used to present different positions of the cross-linked channels. Figure.4.9 and 4.10 show the maximum temperature and the temperature difference on the bottom surface for the heat sinks vs. the dimensionless distance. The width of the transverse channel is 0.5 mm. Minor effect of the positions of transverse channels is discovered from the simulations. Maximum temperature of the heat sink remains almost the same for all positions of cross-linked channel. Decrease of temperature difference on the bottom surface of the heat sink is discovered when the cross-linked channels are placed after the hotpots, especially under low inlet velocity ($L_1^* > 27 \times 10^3$ and $L_2^* > 57 \times 10^3$). In former discussion, the differences of fluid properties and temperature between channels may cause flow mixing in the cross-linked channel. However, when the cross-linked channels are placed after the hotspots, which leads to greater difference in fluid properties at the inlet of the transverse channels, no significant effect on temperature distribution is observed.

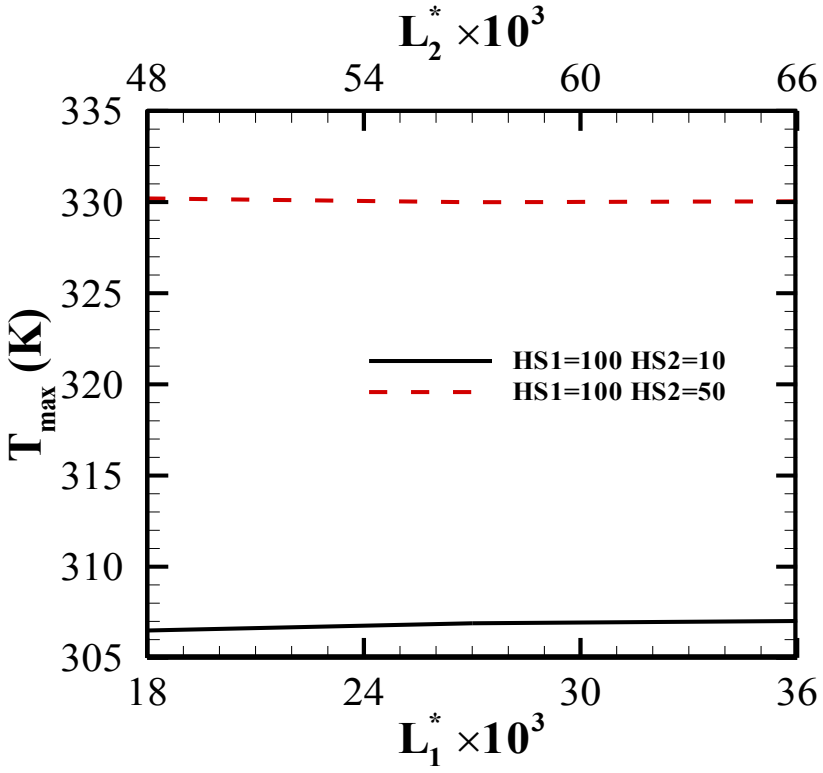

(a) V=0.5 m/s

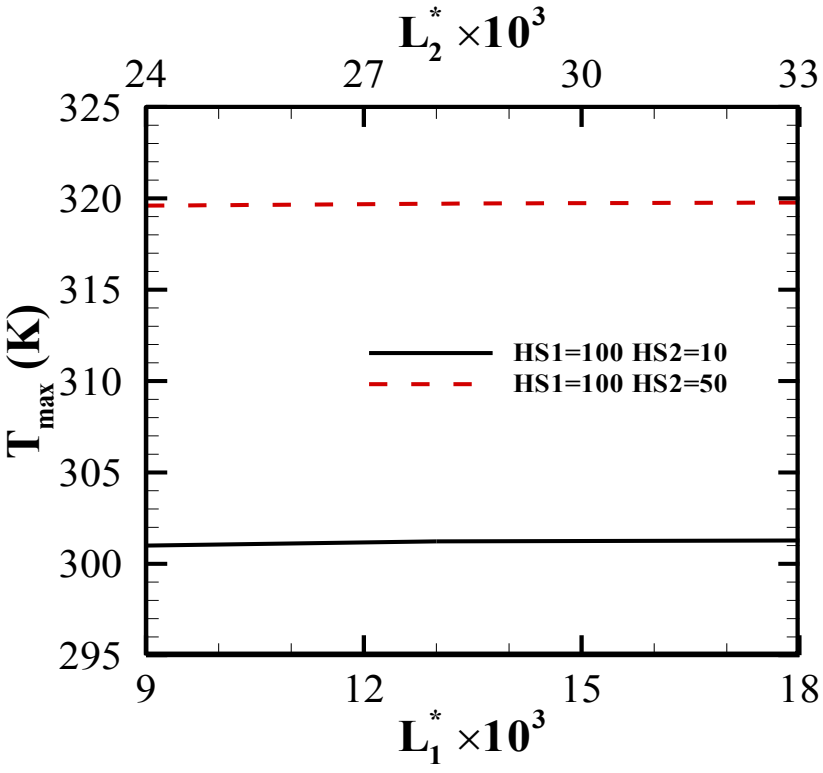

(b) V=1 m/s

Figure. 4.9 Maximum temperature of the heat sink versus dimensionless position of cross-linked channels (a) V=0.5 m/s (b) V=1 m/s

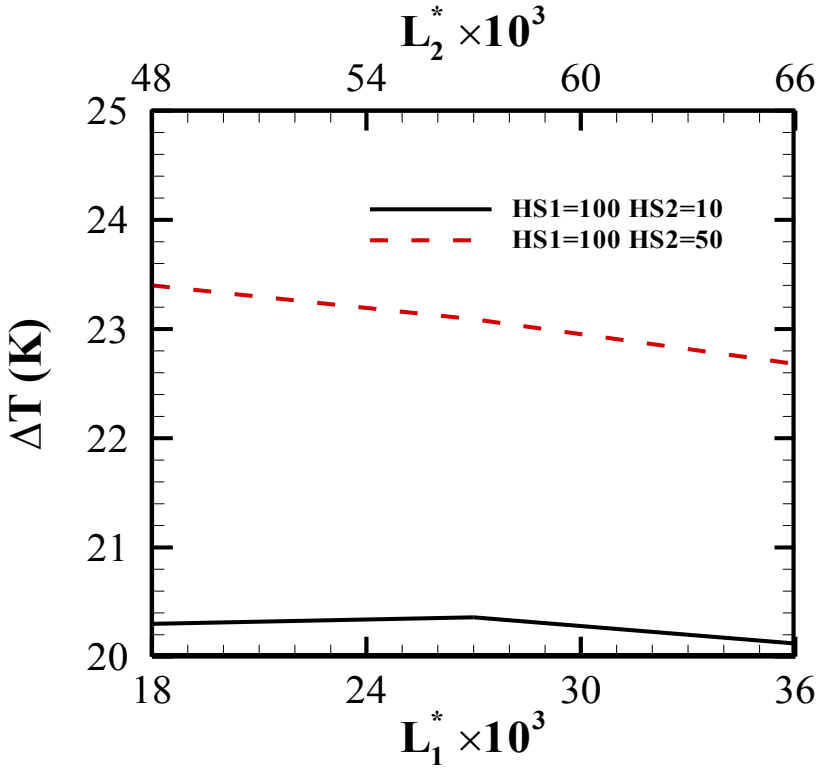

(a) V=0.5 m/s

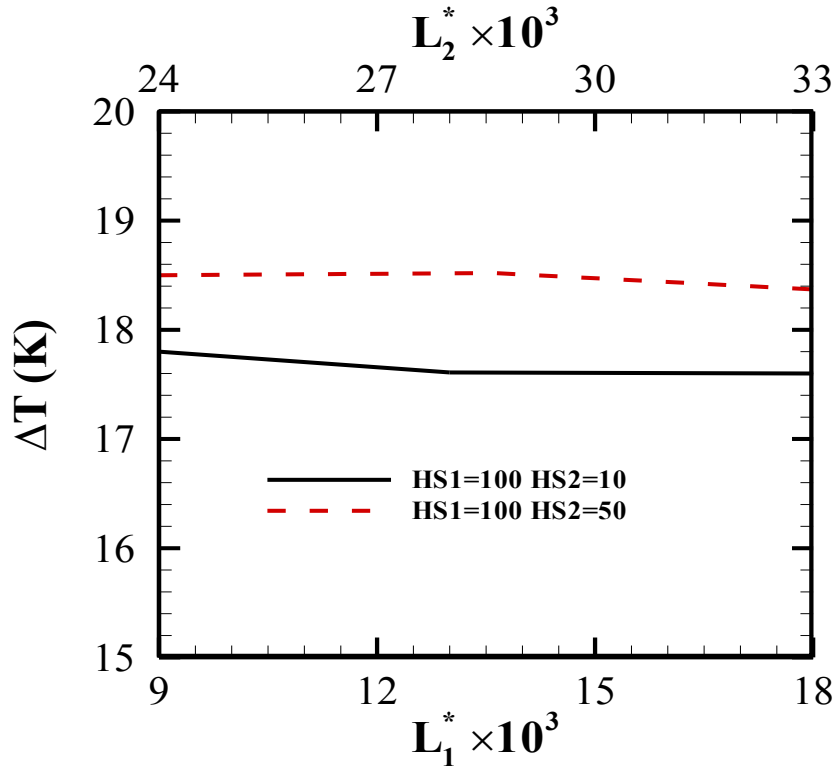

(b) V=1 m/s

Figure. 4.10 Temperature difference of the heat sink versus dimensionless position of cross-linked channels (a) V=0.5 m/s (b) V=1 m/s

4.3.4 Pressure Drop

The value of the pressure drop is equal to the area-weighted average pressure at the inlet for gauge pressure at the outlet is set to zero. Figure.4.11 presents the pressure drop for straight and cross-linked micro heat sinks with two hotspots on the bottom surface. The transverse channels are above the centers of the hotspots. The flow is pressure driven, so pressure drop rises as inlet velocity increases. The difference is minimal for different heating conditions under either inlet velocity. As W_{cr} increases, a minor decrease is observed in pressure drop. The effect of cross-linked channels on pressure drop can be neglected. There is a slight decrease in pressure drop when higher heat flux is applied on the bottom of the heat sink for fluid viscosity is reduced. The effect of positions of transverse channels is negligible on pressure drop which can be observed in Figure.4.12.

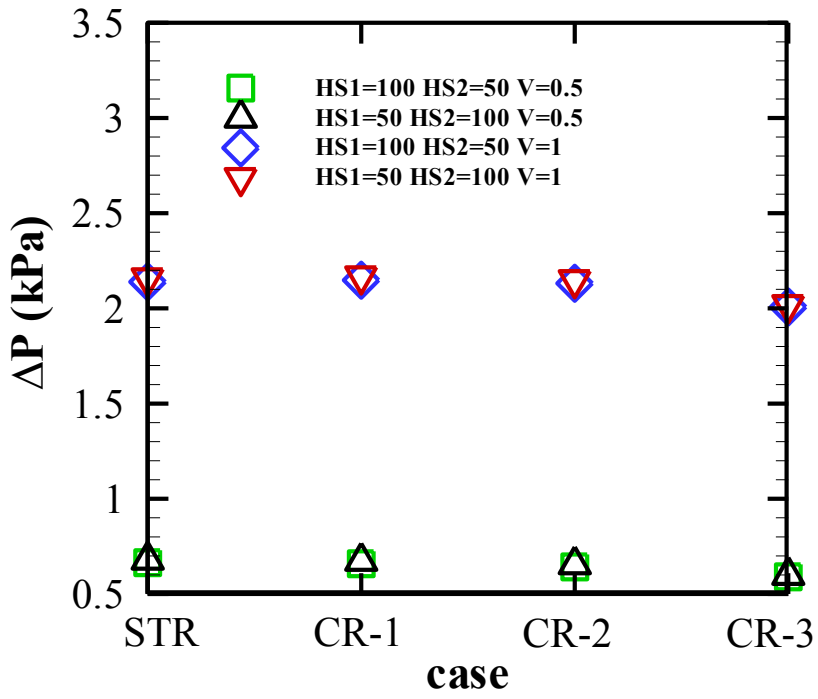

Figure. 4.11 Pressure drop of straight and cross-linked microchannel heat sink

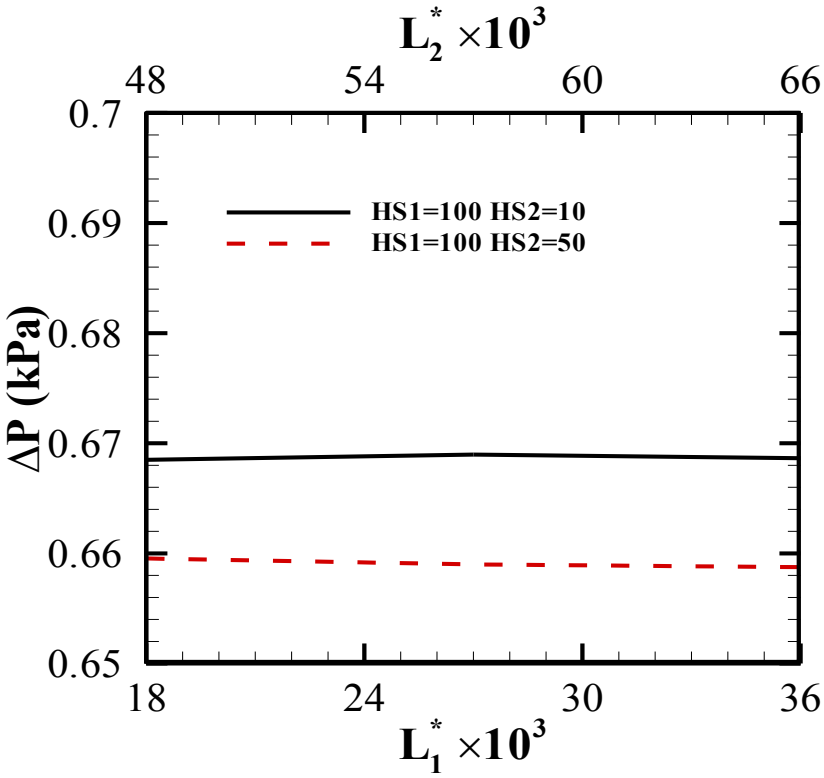

(a) V=0.5 m/s

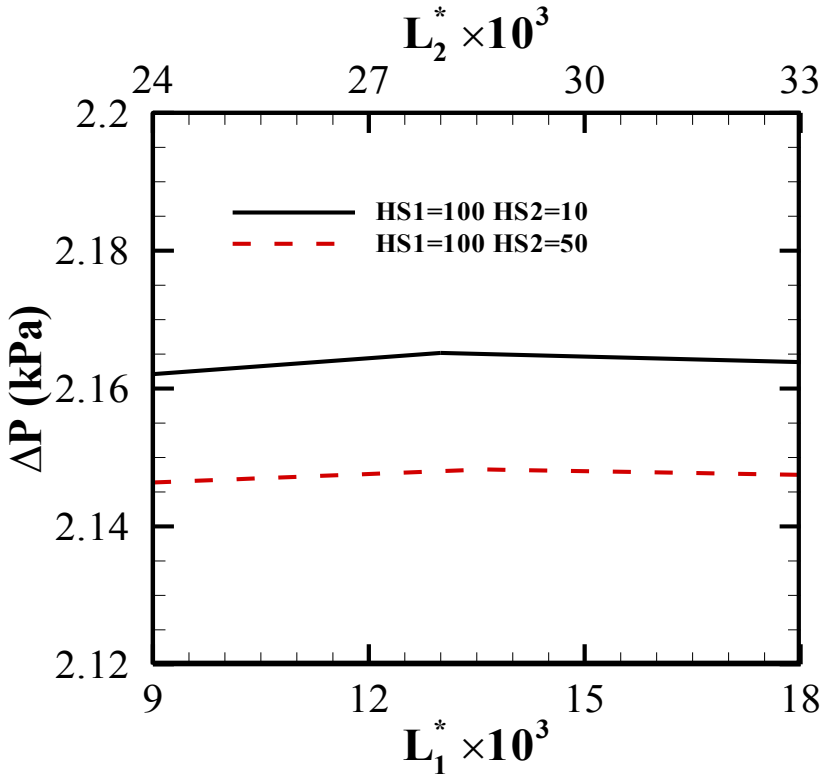

(b) V=1 m/s

Figure. 4.12 Pressure drop of cross-linked microchannel heat sink vs. dimensionless position of cross-linked channels (a) V=0.5 m/s (b) V=1 m/s

4.4 Summary

In this chapter, the cooling performance and pressure drop of a traditional straight channel heat sink and a cross-linked microchannel heat sink with 3 different W_{cr} are studied. Four different non-uniform heating conditions with hotspots are applied to the bottom surfaces of the heat sinks.

It is found that all investigated heat sinks have lower maximum temperatures and temperature differences when hotspot is placed in the upstream region or upstream hotspot is subjected to a higher heat flux than the downstream one. When the hotspot is in the upstream region, adding another hotspot in the

downstream region causes a much more significant temperature rise at the downstream hotspot than the contrary condition. With the presence of cross-linked channels, temperature distribution has better uniformity at the hotspot zones and pressure drop of the heat sink decreases. Although heat sinks with wider cross-linked channel have lower pressure drop, the rapid increase of temperature at the hotspots, notably deteriorates their cooling performance. Consequently, the cross-linked heat sink has the best cooling performance with a cross-linked channel width of 0.5 mm with slight improvement of the heat sink cooling performance. The effects of the position of the cross-linked channels are also studied. No significant improvement in heat sink performance is found.

Chapter 5 Cooling Performance of Straight Channel Micro Heat Sinks under Continuously Varying Heat Flux

In this chapter, straight channel micro heat sink is applied to dissipate heat from heat sources generating continuously varying heat fluxes. Continuously varying heat fluxes on a rectangular plate can be found on the illuminated surface of a concentrated photovoltaic cell. Two heat sink layouts are proposed and their cooling performances are compared. For the heat sink layout with the better performance, optimization is applied to obtain the optimal geometry size and the effects of geometry parameters on heat sink performance.

5.1. Module Specifications

The sketches of the two layouts of straight channel heat sinks are shown in Figure.5.1. The heated area is 10 mm ×10.75 mm at the center of the bottom surface. For heat sink layout 1, the continuously varying heat flux changes perpendicular to flow direction; while for heat sink layout 2, heat flux decreases along flow direction (as shown in Figure.5.2). Heat sink layout 1 is a standard straight channel heat sink with 12 mm in length, 10.75 mm in width, and 1 mm in height. The header and collector are both 1 mm × 10.75 mm × 0.5 mm cuboid plenums placing at the two ends of channel. The top surfaces of the

two plenums are set as inlet and outlet respectively. The size of heat sink layout 2 is 13.75 mm ×10.25 mm ×1 mm. The cuboid header which is 1 mm ×10.5 mm × 0.5 mm is at the middle of the module. There are two collectors with the same size of the header at the two ends of the module. The length of the channels is 4.875 mm. For both heat sinks, the channels are 0.25 mm × 0.5mm. The wall between each two channels is 0.25 mm thick. Due to symmetric geometry, half of layout 1 and a quarter of layout 2 are selected as their computational domains, respectively. Table.5.1 lists the summary of geometric specifications for both of the computational domains. Water and copper are set as the materials of fluid and solid respectively.

For the two layouts, two heat flux distributions with the similar shape with the references are presumed and simulated, which are expressed in following equations:

$$q1 = 80 \times e^{-y} + 20 \tag{5.1}$$

$$q2 = 50 \times e^{-y} + 50 \tag{5.2}$$

The approach of simulating the heat flux is described in section 3.1.3. For heat sink layout 1 and 2, the heat flux changes perpendicular and along flow direction, respectively, as shown in Figure.5.2.

Table. 5.1 Module specifications (unit: mm)

Parameter	L_i	L_w	L_o	W_i	W_w	W_c	H_c	H_b
Layout 1	1	10	1	5.375	0.25	0.25	0.5	0.5
Layout 2	1	4.875	0.5	5.125	0.25	0.25	0.5	0.5

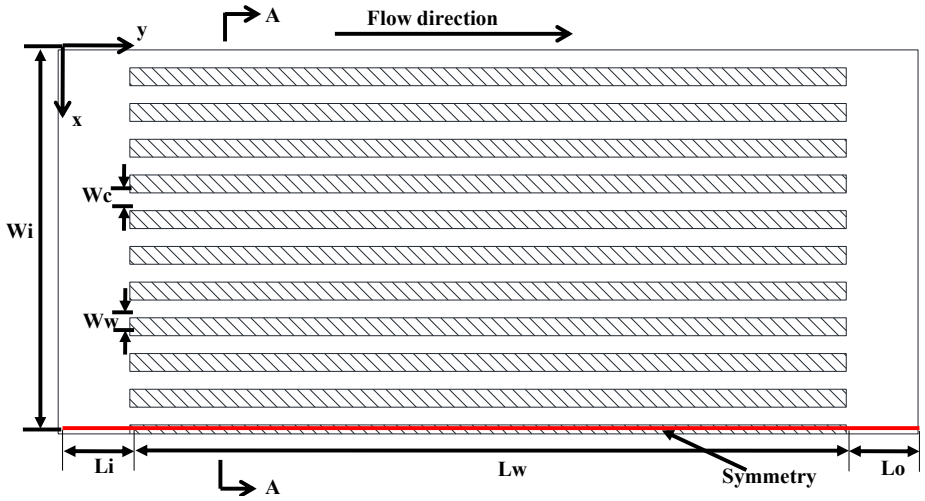

(a)

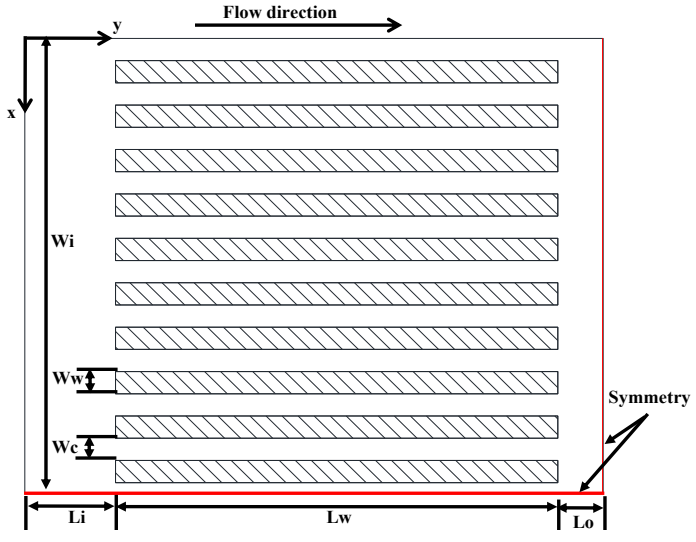

(b)

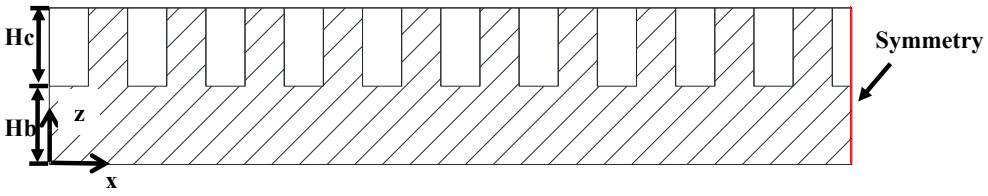

(c)

Figure. 5.1 Sketch of geometry (a) layout 1 (b) layout 2 (c) A- A sectional view

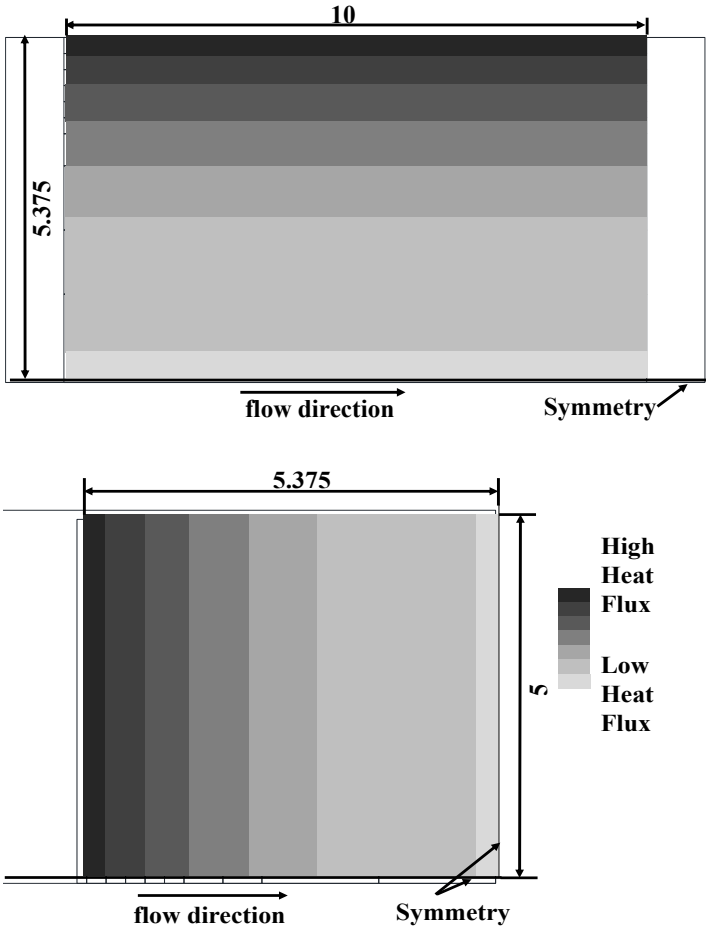

Figure. 5.2 Heat flux on bottom surfaces

5.2 Mesh Independence

Mesh independence is studied before simulation. Take heat sink layout 2 for example, structured non-uniform mesh system with 0.23M cells, 0.68M cells

and 1.13M cells are compared. Figure.5.3 shows the partial mesh from the bottom view of the heat sink. Red boxes are the separated zones for the simulation of the heat flux. Figure.5.4 presents the temperature distribution on the line at x=0.25 mm on the bottom surface which is under the edge of the side channel and at the edge of the heated surface as well. With mass flow rate of 23.4 g/min, mesh systems with 0.68M and 1.13M cells show almost identical performance. Hence, structured mesh with 0.68M cells is used for further simulations.

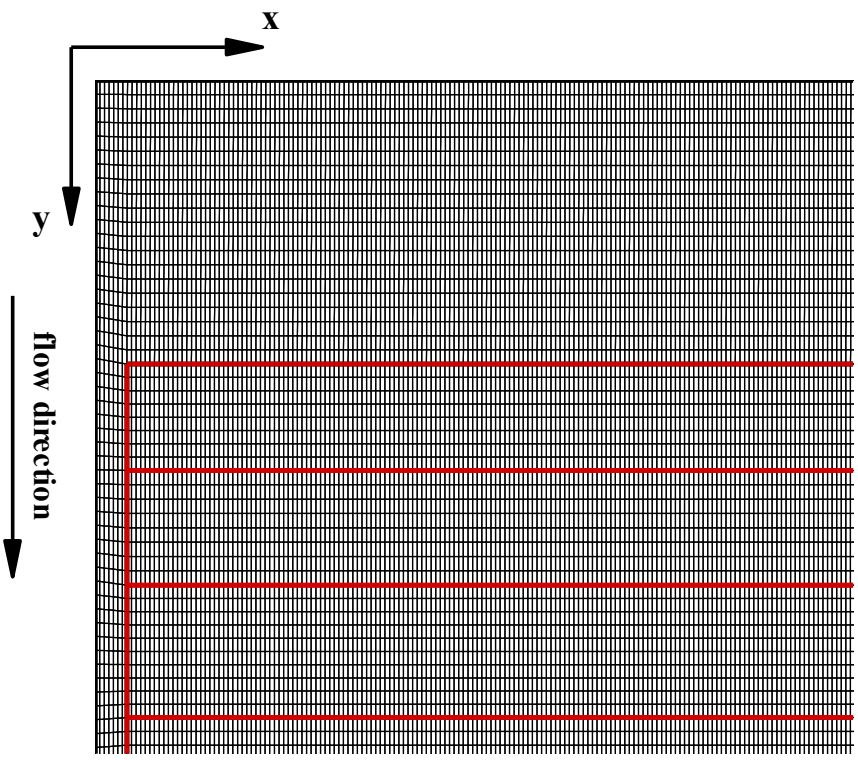

Figure. 5.3 Partial mesh from the bottom view of heat sink layout 2

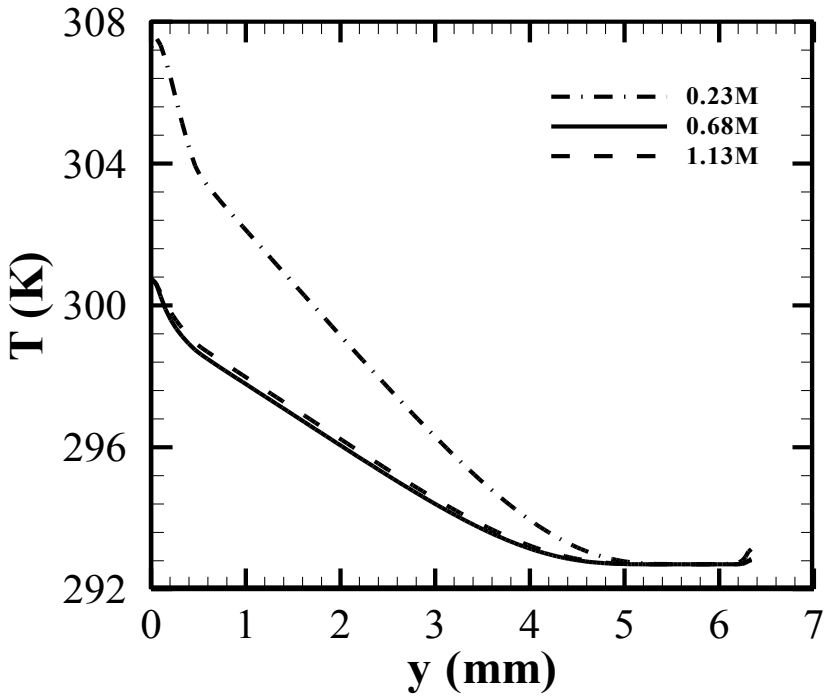

Figure. 5.4 Temperature distribution on the line at x=0.25 mm

5.3 Cooling Performance

5.3.1 Temperature Distribution

Temperature distribution is important for the working efficient for the CPV cells. The CPV cells usually work more efficiently under lower temperatures. And the temperature difference of the cells is another main effect on efficiency. When the CPV cells work under different temperatures, the arrays with lower efficiency deteriorates the overall performance of the CPV cells. Figure.5.4 presents the temperature distribution on the bottom surfaces of the two heat sinks at the mass flow rate of 23 g/min. The mass flow rate is calculated for half of the whole module which is the computational domain for layout 1 and

twice the computational domain for layout 2. Heat sink layout 2 has greatly improved temperature uniformity on the bottom surface than layout 1. For heat sink layout 1, the maximum temperature appears beneath the exit of the side channel which is in the zone with the maximum heat flux. This is resulted from the high heat flux and the high fluid temperature near the outlet. For heat sink layout 2, the zone under the outlet plenum maintains the highest temperature of the whole bottom surface because of the highest fluid temperature. Although the heat flux there is the lowest the small heat transfer surface area and the high fluid temperature cannot remove the large amount of heat flux.

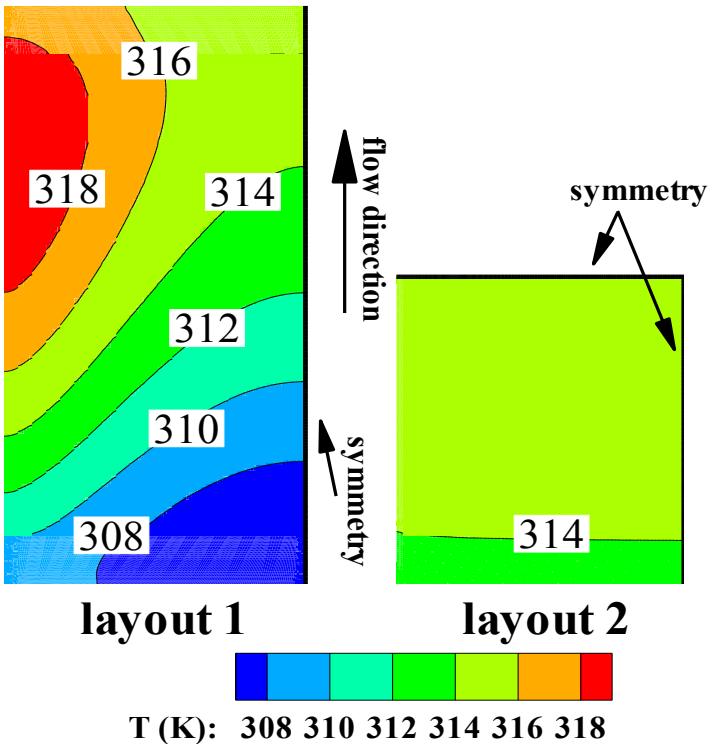

Figure. 5.5 Temperature distribution on the bottom surface of heat sinks under q1 with a mass flow rate of 23 g/min

As can be seen from Figure.5.6 and 5.7, layout 2 maintains lower maximum temperature and temperature difference of the heat sink than that of the other one. In heat sink layout 2, the heat flux decreases along the flow direction in which fluid velocity and temperature rises. The three effects compromise thus low maximum temperature and temperature difference can be obtained. However, in heat sink layout 1, in the channel above the highest heat flux zone, the fluid velocity and temperature rises. Increase of the fluid velocity is not able to compensate the effect of fluid temperature rise on reduction of the heat transfer coefficient, and eventually causes higher maximum temperature and temperature difference on the bottom surface.

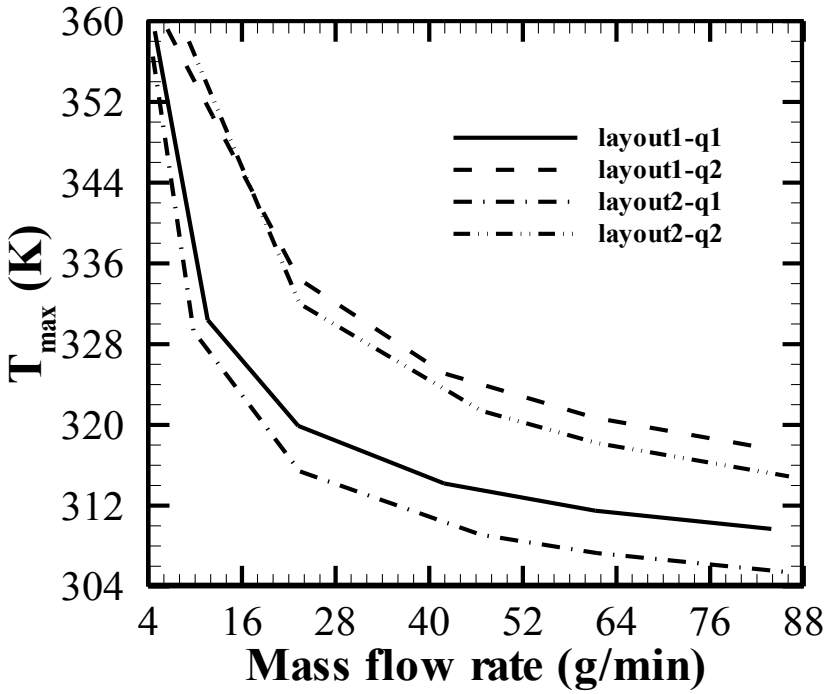

Figure. 5.6 Maximum temperature of heat sinks with various mass flow rate and heat flux distributions

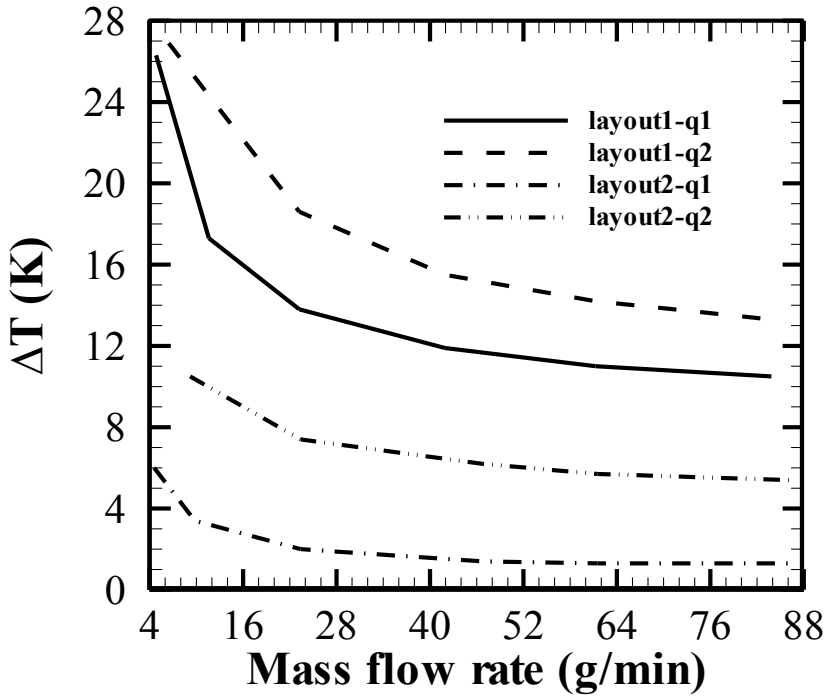

Figure. 5.7 Temperature difference of the bottom surface with various mass flow rate and heat flux distributions

For all conditions tested, increase in the inlet mass flow rate reduces the maximum temperature and temperature difference of the heat sinks, since heat transfer is enhanced by greater fluid velocity. When the mass flow rate is low, maximum temperature and temperature difference drops drastically with increase of mass flow rate. However, the benefit decreases when increasing inlet mass flow rate. There is a critical value for the mass flow rate. When mass flow rate reaches 64 g/min and 40 g/min for maximum temperature and temperature difference respectively, the two parameters almost level off.

5.3.2 Dimensionless pressure drop

The value of pressure drop is determined from the area-weighted-average pressure at the inlet. In this work, Bejan number (Be) at the inlet is used to present the pressure drop in the heat sinks in a non-dimensional way. Bejan number is the dimensionless pressure drop along a channel with length of L, which is calculated by the following equation:

$$Be = \frac{\Delta P L^2}{\mu \alpha} \tag{5.2}$$

where ΔP is the pressure drop of the heat sink; L is the channel length; μ and α are dynamic viscosity and thermal diffusivity of water, respectively.

The length of the channel, dynamic viscosity and thermal diffusivity are fixed values, thus the trend of Bejan number represents the trend of pressure drop in each heat sink, as shown in Figure.5.8. Because the flow is pressure driven, Bejan number rises when mass flow rate increases; and at the same time, average velocity increase in the channels. Increasing heat flux on the bottom surface causes a small drop of the Bejan number. Viscous effect is the main factor influencing pressure drop. Higher heat flux leads to lower viscosity of water which reduces the pressure drop in the heat sink and consequently reduces the Bejan number. In heat sink layout 1, Bejan number is much higher and rises much more drastically than that in heat sink layout 2. Heat sink layout 1 has larger channel length and pressure drop than layout 1 which result in a significant difference between their Bejan numbers. Heat sink layout 2

consumes less pumping power and the scope for mass flow rate rise is larger.

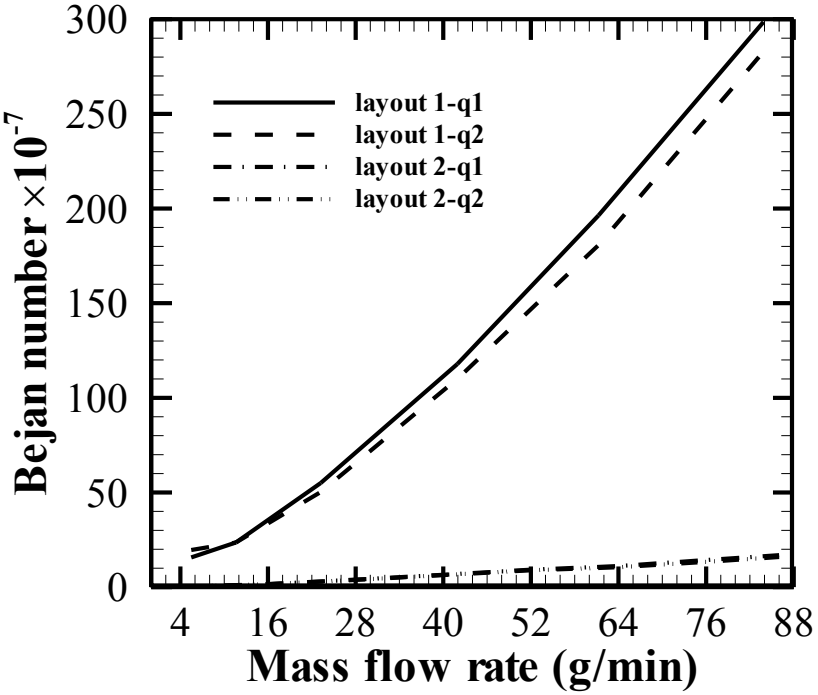

Figure. 5.8 Bejan number with various mass flow rate and heat flux distributions

5.3.3 Dimensionless total thermal resistance

Dimensionless total thermal resistances of the heat sinks with various inlet mass flow rates are compared in Figure.5.9. The dimensionless total thermal resistance as a function of channel geometry for the whole module is calculated as follows:

$$R^*_{total} = \frac{W_c k_f L_c R_{total}}{H_c} \tag{5.3}$$

where

$$R_{total} = \frac{T_{max} - T_{min}}{\dot{Q}_{total}} \tag{5.3}$$

W_c, L_c, H_c are the width, length, height of the channel, respectively; k_f is the thermal conductivity of water. T_{max} and T_{min} are the maximum and minimum temperature of the bottom surface, respectively; $\dot{Q}_{total}$ is the total power applied on the bottom surface.

The total thermal resistance presents the cooling capacity of a heat sink. As shown in Figure.5.9, the dimensionless total thermal resistance decreases with mass flow rate as high Reynolds number of the fluid reduces convective thermal resistance. As a result, the thermal resistance can be reduced by increasing mass flow rate at the inlet. However, there is also a critical value of mass flow rate for the dimensionless total thermal resistance. When the inlet mass flow rate reaches 64 g/min, the dimensionless total thermal resistances for both layouts level off. The dimensionless total thermal resistance of heat sink layout 1 remains higher than that of layout 2. Therefore, at a certain mass flow rate, the cooling capacity of layout 2 is much larger than that of layout 1. Compared to heat sink layout 2, the dimensionless total thermal resistance for layout 1 is more sensitive to the heat flux applied to the heat sink. Heat sink layout 2 has almost identical thermal resistance when increasing heat flux at the bottom surface. As a result, layout 2 is very suitable for high heat flux conditions.

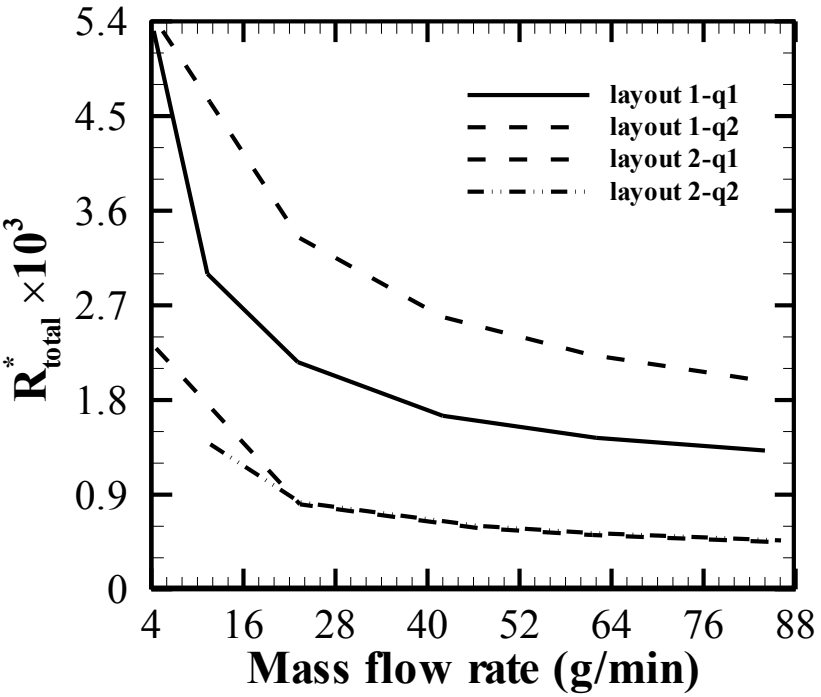

Figure. 5.9 Dimensionless total thermal resistance of heat sinks with various mass flow rate and heat flux distributions

5.3.4 Overall average Nusselt number

The overall average Nusselt numbers vs. Reynolds number for both layouts are depicted in Figure.5.10 under the two heat flux conditions. The overall average Nusselt number is calculated by the following equation:

$$\overline{Nu} = \frac{\bar{h} \cdot D_{h\,c}}{k_f} \tag{5.4}$$

where $D_{h\,c}$ is the hydraulic diameter of the channel, k_f is the thermal conductivity of the fluid, $\bar{h}$ is the average heat transfer coefficient which can be calculated by:

$$\bar{h} = \frac{Q}{A \cdot (T_w - T_b)} \tag{5.5}$$

where Q is the total heat dissipated through the channel wall, A is the total heat transfer surface of the channels, T_w is the temperature of the channel bottom and side surface, T_b is the bulk temperature of the fluid, the average temperature of the fluid is used in this case.

The overall average Nusselt number represents the ratio of convective to conductive heat transfer coefficient near the channel wall. A large average Nusselt number shows more intensive convective heat transfer at the wall. For both heat sink layouts, the average Nusselt number increases with increasing Reynolds number because convective heat transfer coefficient is raised by high Reynolds number. However, the effect of Reynolds number on the overall Nusselt number lessens. For layout 1, the average Nusselt number under q1 is slightly greater than that under q2. The situation is the contrary for heat sink layout 2. In addition, the overall average Nusselt number in layout 2 is much higher than that in layout 1. The local Nusselt number is much higher in the developing flow than that in the fully developed flow. There are two inlets in layout 2 which leads to double entrance length. Therefore, the average Nusselt number is increased significantly, especially under higher Reynolds number.

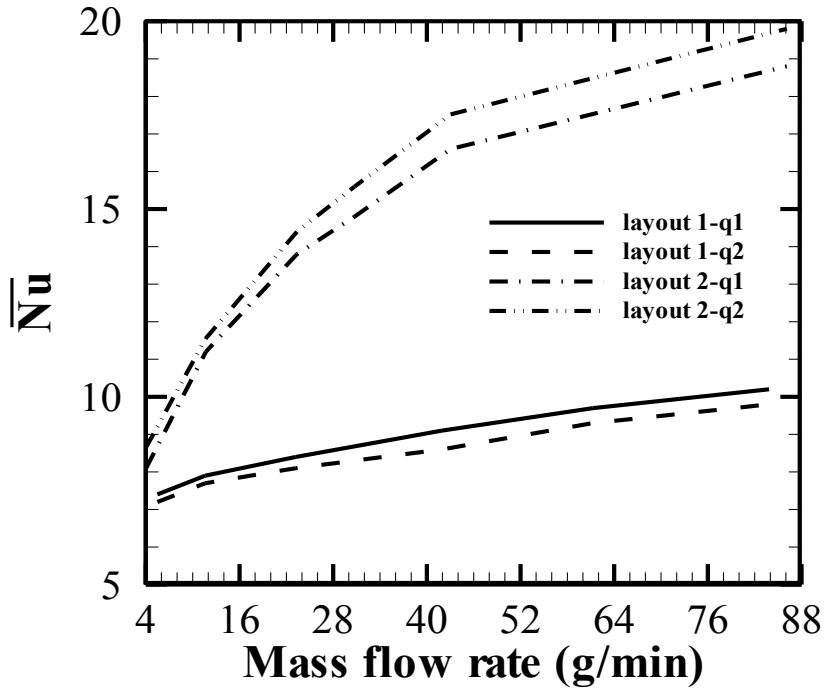

Figure. 5.10 Average Nusselt number with various mass flow rate and heat flux distributions

5.4 Optimization

For heat sink layout 2, the geometry sizes of the micro channel and the substrate are optimized to obtain better cooling performance and to study the effects of geometries on cooling performance. The heat sink layout is optimized under three different heat fluxes as following:

$$q1 = 80 \times e^{-y} + 20 \tag{5.4}$$

$$q2 = 50 \times e^{-y} + 50 \tag{5.5}$$

$$q3 = 30 \times e^{-y} + 20 \tag{5.6}$$

Their distribution curves are shown in Figure.5.9. The mass flow rate given here is the value for half of the module which is twice of the computational domain.

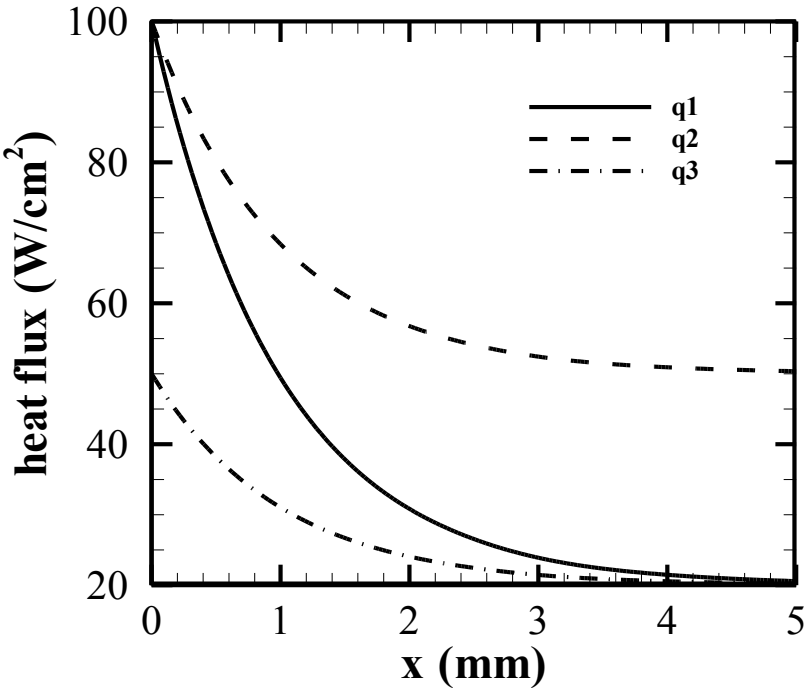

Figure. 5.11 Distribution curves of heat fluxes

The Taguchi method is employed to determine the optimal dimensions from the test ranges under each heat flux condition. The optimization procedure is described in section 3.2. For the micro channel heat sink, the dimensions of channel and wall are important parameters for heat sink cooling performance. The length of the channel is fixed. As a result, the height and width of the channel, the height of the base and the width of the fins are chosen to be the optimization parameters. Their ranges are determined according to the former proposed heat sink layout 2 and presented in the test matrix in Table.5.2. Three levels are selected for each parameter. For a photovoltaic cell, since the

temperature of the cell is the main factor affecting its working efficiency, the objective function of the micro channel heat sink is determined to be the maximum temperature on the bottom surface of the heat sink. According to the Taguchi method, the appropriate an orthogonal array for this optimization is L_9, as shown in Table.5.3. The channel number for each tested heat sink is determined to at least cover the heating area. The flow and heat transfer in the heat sinks are simulated by CFD with a mass flow rate of 20 g/min at the inlet to obtain the objective function which is the maximum temperature on the bottom surface.

Table. 5.2 Test matrix

Parameter	A (H_c)	B (W_c)	C (H_b)	D (W_w)
level 1	0.3	0.1	0.1	0.1
level 2	0.4	0.3	0.2	0.3
level 3	0.5	0.5	0.3	0.5

Table. 5.3 Orthogonal array L_9 (design matrix)

	A	B	C	D
heat sink 1	1	1	1	1
heat sink 2	1	2	2	2
heat sink 3	1	3	3	3
heat sink 4	2	1	2	3
heat sink 5	2	2	3	1
heat sink 6	2	3	1	2

heat sink 7	3	1	3	2
heat sink 8	3	2	1	3
heat sink 9	3	3	2	1

To determine the optimal design, the Signal to Noise ratio (dB) is calculated for the object function– maximum temperature. For the case of minimizing the performance characteristic which is the minimal maximum temperature in the heat sink, the S/N (dB) should be calculated by the following equation:

$$\eta = -10log_{10}\sigma^2 \tag{5.7}$$

where σ^2 is the square of standard deviation of the maximum temperature of the bottom surface which is determined as follows:

$$\sigma^2 = \frac{1}{n}[\sum_{i=1}^{n}(T_i - T_\infty)^2] \tag{5.8}$$

where n is the number of nodes on the bottom surface defined by the mesh; T_i is the temperature of each node; T_∞ is the minimum temperature that the node can reach, which is 293K in this case. Equation 5.7 and 5.8 give an S/N ratio that is negative, with values near zero indicates the better.

5.4.1 Optimization under heating condition q1

Under heat flux q1, the S/N ratio of each test is shown in Table.5.4. With the S/N ratio for each test, the average S/N ratio for each parameter and each level can be calculated. For example, the level 1 of parameter A is examined in test

No.1, No.2 and No.3, so the average S/N ratio for $S/N_{A,1}$ is calculated from:

$$S/N_{A,1} = \frac{S/N_1 + S/N_2 + S/N_3}{3} \tag{5.9}$$

It is similar for other parameters and levels. Once the S/N ratio is calculated for each parameter and level, the noise matrix can be built and the range R (high S/N ratio – low S/N ratio) for each parameter is entered in the table. Larger range R indicates more significant effect on the objective function by the corresponding parameter. The results are listed in Table.5.5 and Figure.5.12.

Table. 5.4 S/N ratio

	A	B	C	D	σ	S/N
heat sink 1	1	1	1	1	417.950	-26.211
heat sink 2	1	2	2	2	1115.100	-30.473
heat sink 3	1	3	3	3	1253.209	-30.980
heat sink 4	2	1	2	3	317.923	-25.023
heat sink 5	2	2	3	1	548.581	-27.392
heat sink 6	2	3	1	2	1075.438	-30.316
heat sink 7	3	1	3	2	207.030	-23.160
heat sink 8	3	2	1	3	842.707	-29.257
heat sink 9	3	3	2	1	930.594	-29.688

Table. 5.5 Noise matrix for q1

level	A	B	C	D
1	-29.222	*-24.798*	-28.595	*-27.764*
2	-27.577	-29.041	-28.395	-27.983

3	*-27.368*	-30.328	*-27.178*	-28.420
Δ	1.853	5.530	1.417	0.656
rank	2	1	3	4

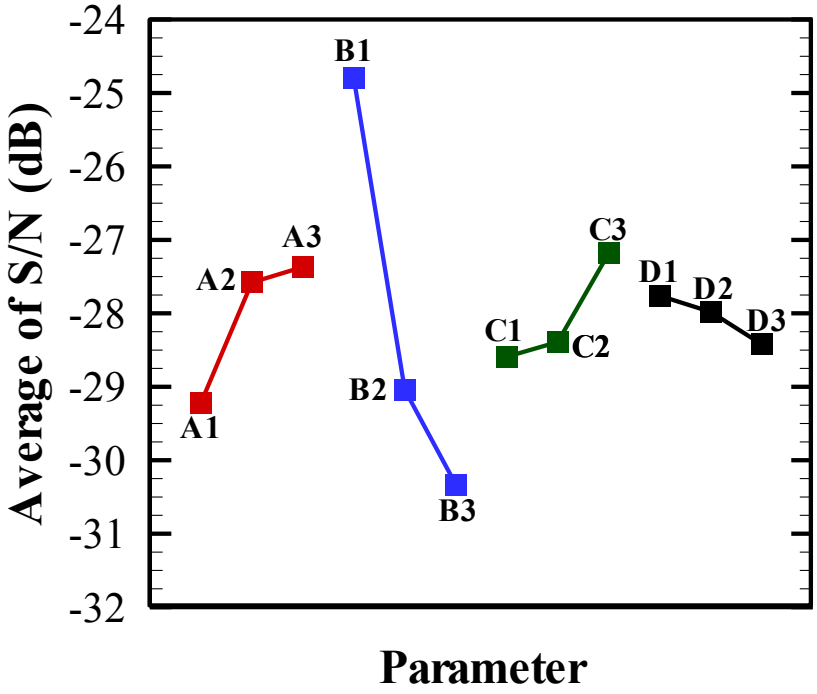

Figure. 5.12 Average S/N of design parameters

As mentioned in former discussion, the nearer to zero the value of the S/N ratio is, the better the performance. In the table of the noise matrix (Table.5.5), the values of the S/N ratio in italic are the levels lead to the best performance for each parameter. And in Figure.5.12, positive slope of the average S/N ratio means that increasing the corresponding parameter causes lower maximum temperature, and vice versa. Thus, combining the results shown in Table.5.5 and Figure.5.12, in the tested range, the optimal dimensions for heat sink layout 2 under q1 are given in Table.5.6. The maximum temperature is most sensitive to the width and height of the channel (parameters listed in order).

Table. 5.6 Optimal design under q1

Paremeter	A (H_c)	B (W_c)	C (H_b)	D (W_f)
Dimension (mm)	0.5	0.1	0.3	0.1

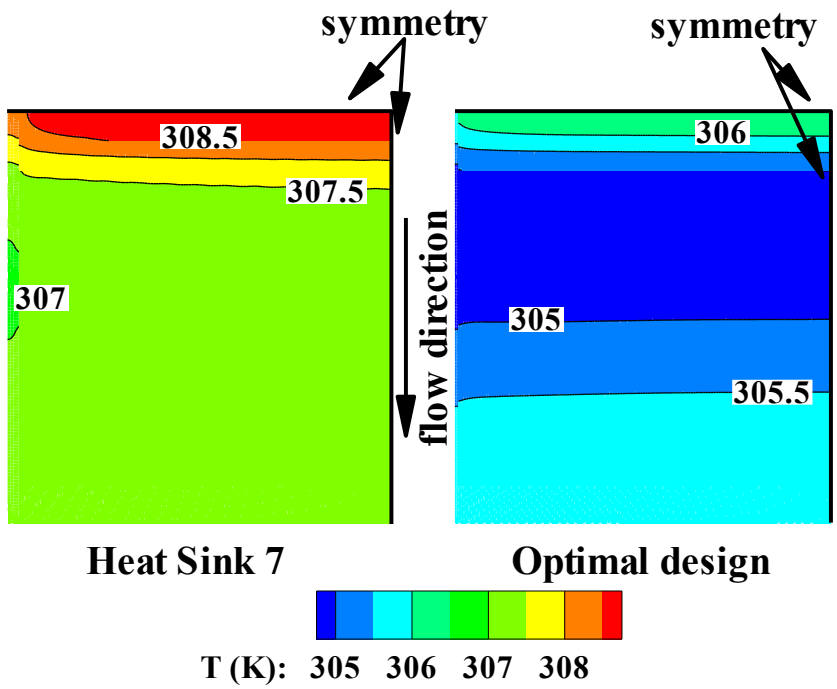

Figure. 5.13 Temperature distribution on the bottom surface of heat sink 7 and optimal design

Figure.5.13 presents the temperature distribution on the bottom surfaces of heat sink 7 and the optimal design. From Table.5.4, heat sink 7 has the highest S/N ratio among the 9 tested heat sinks, which means it has the best performance. Compared to heat sink 7, the optimal design maintains lower maximum temperature and better temperature uniformity in both stream-wise and transverse directions.

The effects of the sensitive parameters are shown in Figure.5.14 and Figure.5.15. The maximum temperature reduces with decreasing channel width.

When the channel width is small, although in each channel the mass flow rate decreases, a greater number of channels are placed in the heat sink and concomitantly results in much larger heat transfer area. Therefore, heat transfer is enhanced with large amount of contact area between fluid and solid. The slope of temperature decreasing increases when the channel width is reduced from 0.3 mm to 0.1 mm. This suggests that the effect on increasing heat transfer area by narrowing the channels is more significant with small channel width. For the height of the channels, with the same channel width, increasing the channel height lowers the maximum temperature. This implies that the larger the aspect ratio (Hc/Wc), the stronger the heat transfer is in the heat sink. Similar results have also been found in the work of Li et al. (2006).

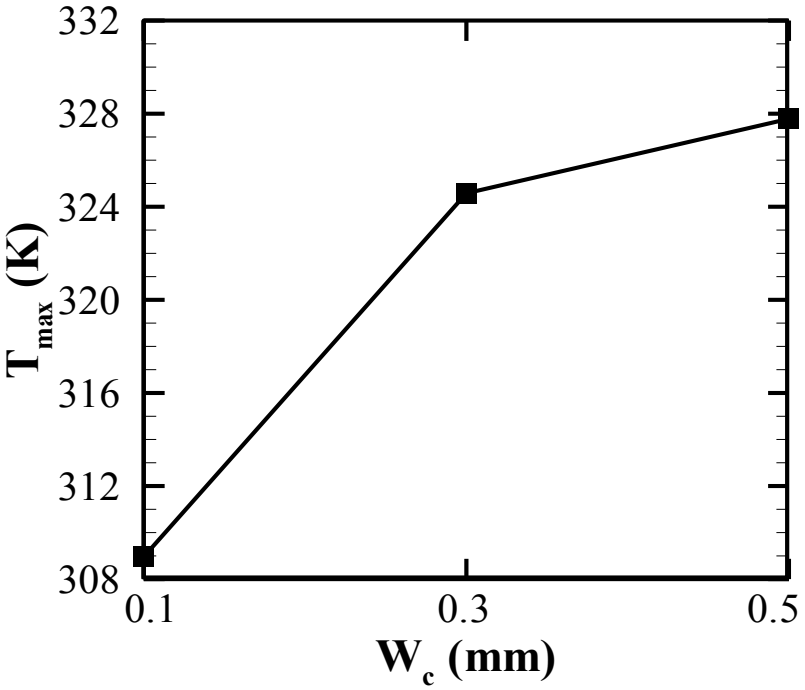

Figure. 5.14 The effect of width of channel (W_c, parameter B) on maximum temperature, H_c=0.5 mm, W_f=0.1 mm

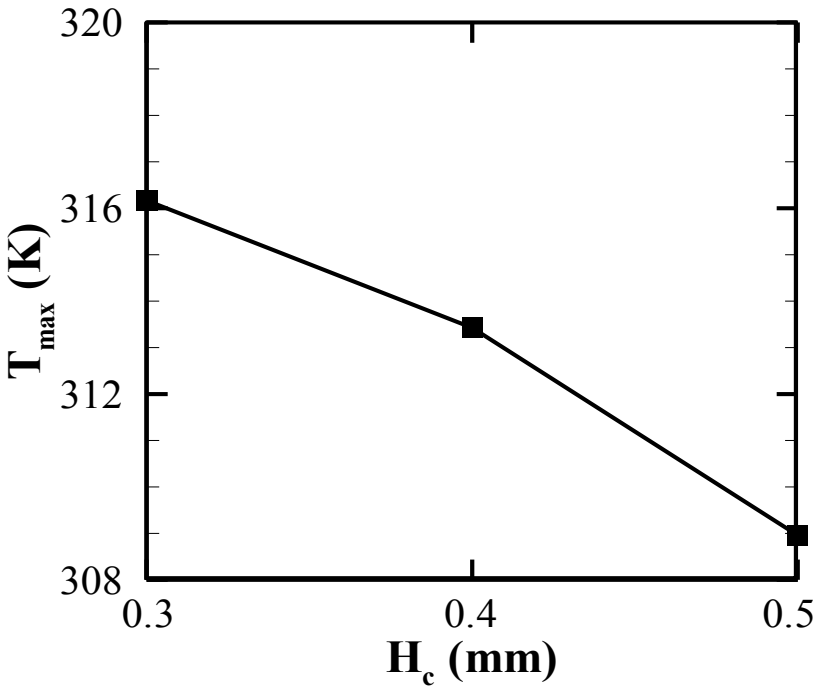

Figure. 5.15 The effect of height of channel (H_c, parameter A) on maximum temperature, W_c=0.1 mm, W_f=0.1 mm

5.4.2 Optimization under heating condition q2

The q2 heating condition has higher heat flux than q1. After simulations with CFD for each test and the calculation for S/N ratios, the optimization results under this heating condition are listed in Table.5.7 – 5.8 and Figure.5.16. And the optimal dimensions are acquired and listed in Table.5.9. The objective function is most sensitive to the width of the channels and the height of the base which is different from that under q1. The width of the channels is still the main effect of heat sink cooling performance. While with high heat flux, the thickness of the base becomes the second most important parameter.

Table. 5.7 S/N ratio

	A	B	C	D	σ	S/N
heat sink 1	1	1	1	1	449.649	-26.529
heat sink 2	1	2	2	2	1935.294	-32.867
heat sink 3	1	3	3	3	3178.958	-35.023
heat sink 4	2	1	2	3	819.900	-29.138
heat sink 5	2	2	3	1	1410.085	-31.492
heat sink 6	2	3	1	2	2878.347	-34.591
heat sink 7	3	1	3	2	530.010	-27.243
heat sink 8	3	2	1	3	1984.923	-32.977
heat sink 9	3	3	2	1	2298.690	-33.615

Table. 5.8 Noise matrix under q2

level	A	B	C	D
1	-31.473	*-27.636*	-31.366	*-30.545*
2	-31.740	-32.446	-31.873	-31.567
3	*-31.278*	-34.410	*-31.253*	-32.379
Δ	0.46	6.77	0.62	1.83
rank	4	1	3	2

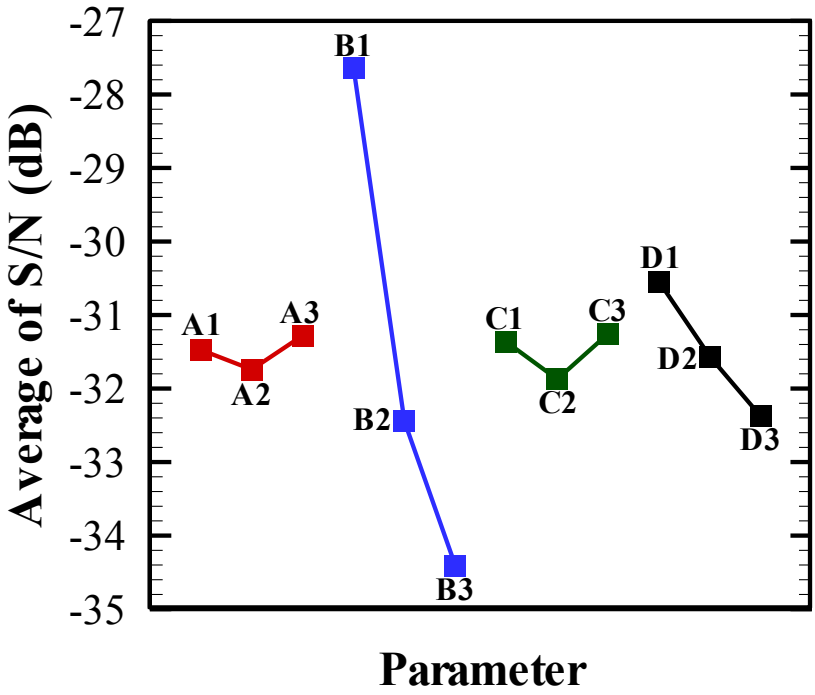

Figure. 5.16 Average S/N ratio of design parameters

Table. 5.9 Optimal design under q2

Paremeter	A (H_c)	B (W_c)	C (H_b)	D (W_f)
value	0.5	0.1	0.3	0.1

The temperature distribution on the bottom surfaces of the heat sink 9 and the optimal design is compared in Figure.5.17. Heat sink 1 performs best among the tested heat sinks since the S/N ratio for the objective function is nearest to zero in Table.5.7. It can be seen from Figure.5.17 that the maximum temperature and the temperature variation on the bottom surface are smaller for the optimal design.

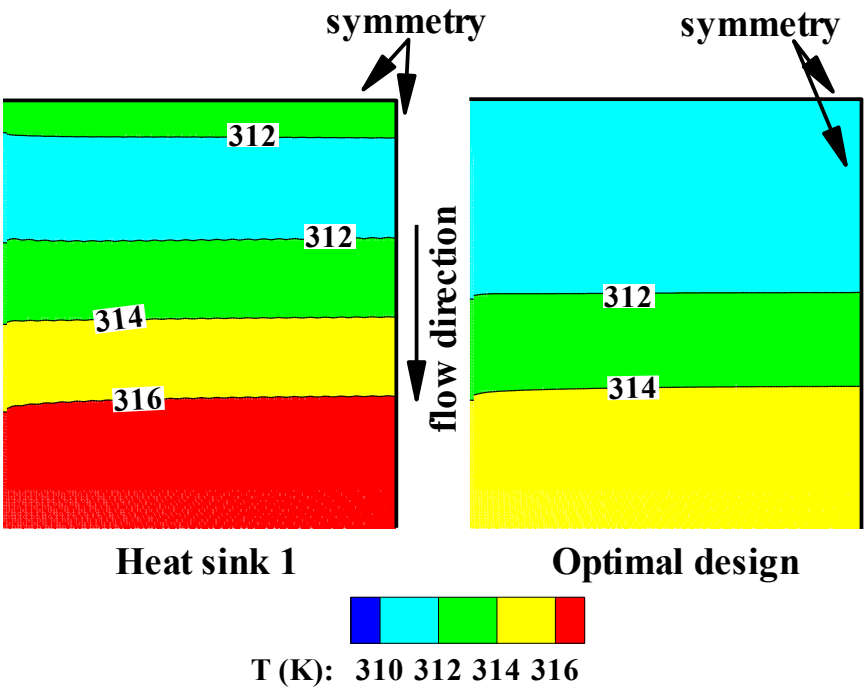

Figure. 5.17 Temperature distribution on the bottom surface of heat sink 1 and optimal design

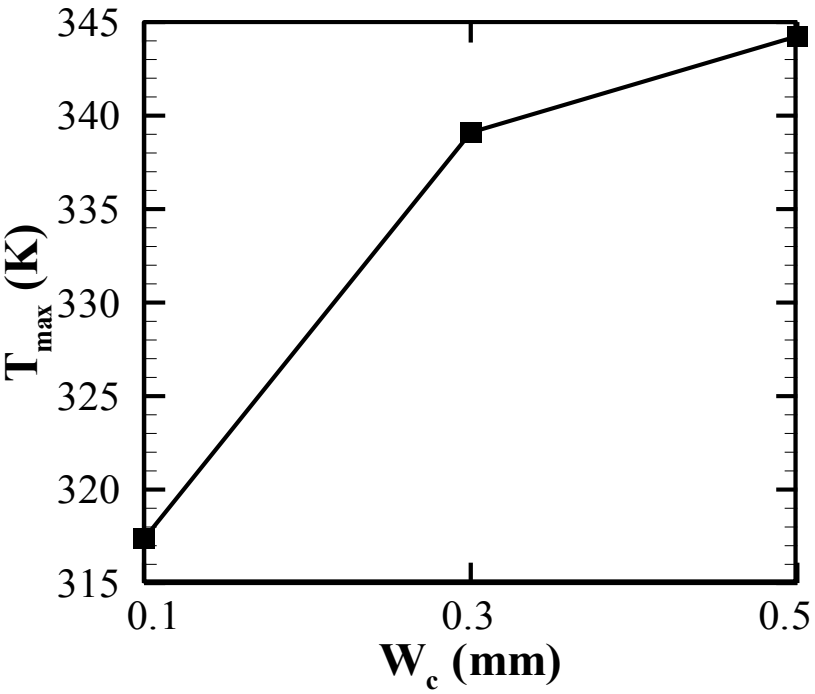

Figure. 5.18 The effect of width of channel (W_c, parameter B) on maximum temperature, H_c=0.5 mm

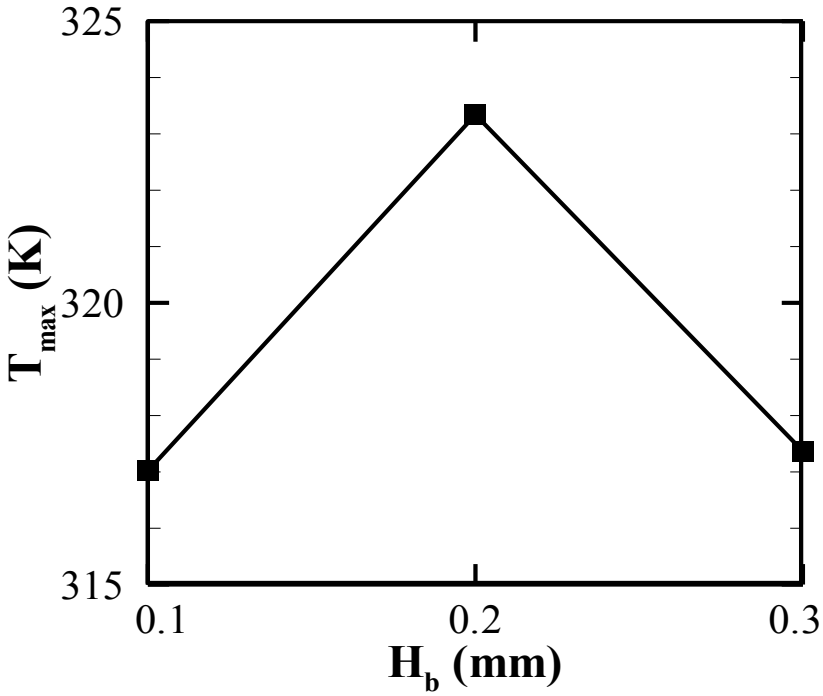

Figure. 5.19 The effect of height of base (H_b, parameter D) on maximum temperature, W_c=0.1 mm

The effects on the objective function of the two most sensitive parameters are given in Figure.5.18 and Figure.5.19. Similar to the results under heating condition q1, under higher heat flux q2, narrower channels bring about lower maximum temperature because there are more channels and consequentially lead to larder heat transfer area. And the effect is more significant with smaller channel width. For the height of the base, the performance of the heat sink is worst when H_b is equal to 0.2 mm.

5.4.3 Optimization under heating condition q3

The heating condition q3 has the lowest heat flux among all three and the

gradient is small like q2. The S/N ratios and noise matrix can be found in Table.5.12 and Table.5.13. The average S/N ratio is also presented in Figure.5.20. The optimal dimensions are listed in Table.5.12; and the two most sensitive parameters are width and height of the channels.

Table. 5.10 S/N ratio

	A	B	C	D	σ	S/N
heat sink 1	1	1	1	1	88.454	-19.467
heat sink 2	1	2	2	2	390.890	-25.921
heat sink 3	1	3	3	3	674.095	-28.287
heat sink 4	2	1	2	3	158.116	-21.990
heat sink 5	2	2	3	1	563.031	-27.505
heat sink 6	2	3	1	2	580.827	-27.640
heat sink 7	3	1	3	2	104.186	-20.178
heat sink 8	3	2	1	3	409.584	-26.123
heat sink 9	3	3	2	1	474.793	-26.765

Table. 5.11 Noise matrix under q3

level	A	B	C	D
1	-24.558	*-20.545*	*-24.410*	*-24.579*
2	-25.712	-26.516	-24.892	-24.580
3	*-24.356*	-27.564	-25.324	-25.467
Δ	1.356	7.019	0.913	0.888
rank	2	1	3	4

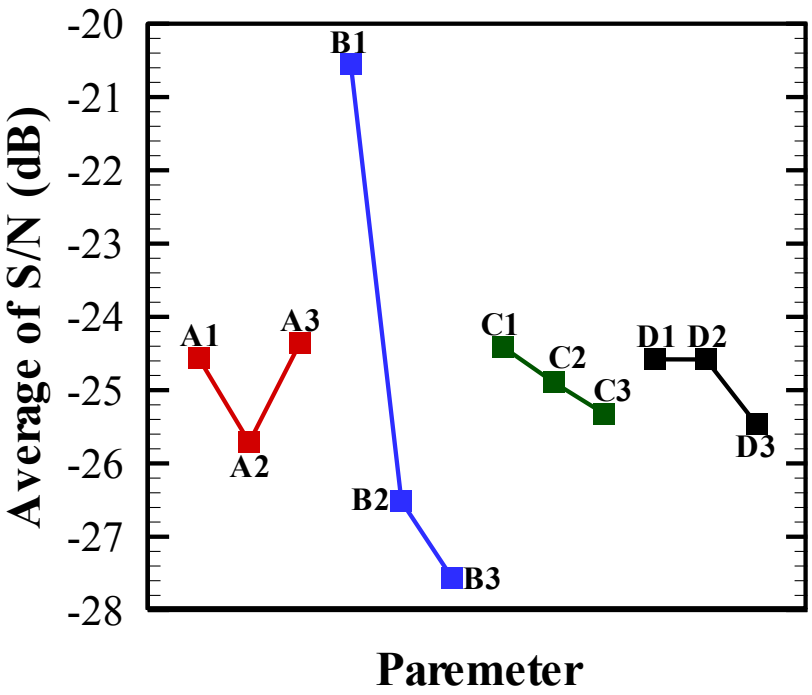

Figure. 5.20 Average of S/N ratio for design parameters

Table. 5.12 Optimal design under q3

Paremeter	A (H_c)	B (W_c)	C (H_b)	D (W_f)
value	0.5	0.1	0.1	0.1

Heat sink 1 is the one with lowest maximum temperature and the temperature distribution on its bottom surface is compared to that of the optimal design in Figure.5.21. Temperature distribution on the bottom surface proves that optimal design maintains a lower maximum temperature and temperature difference. Figure 5.22 and Figure.5.23 shows the effects of channel width and height on the objective function respectively. It should be noticed that under q3, the maximum temperature is highest when channel height is 0.3 mm.

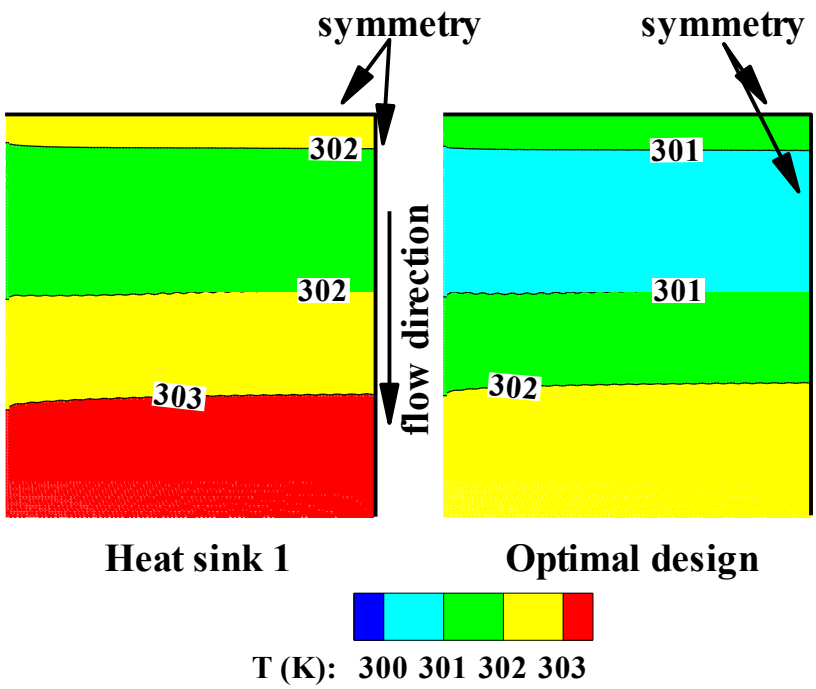

Figure. 5.21 Temperature distribution on the bottom surface of heat sink 1 and optimal design

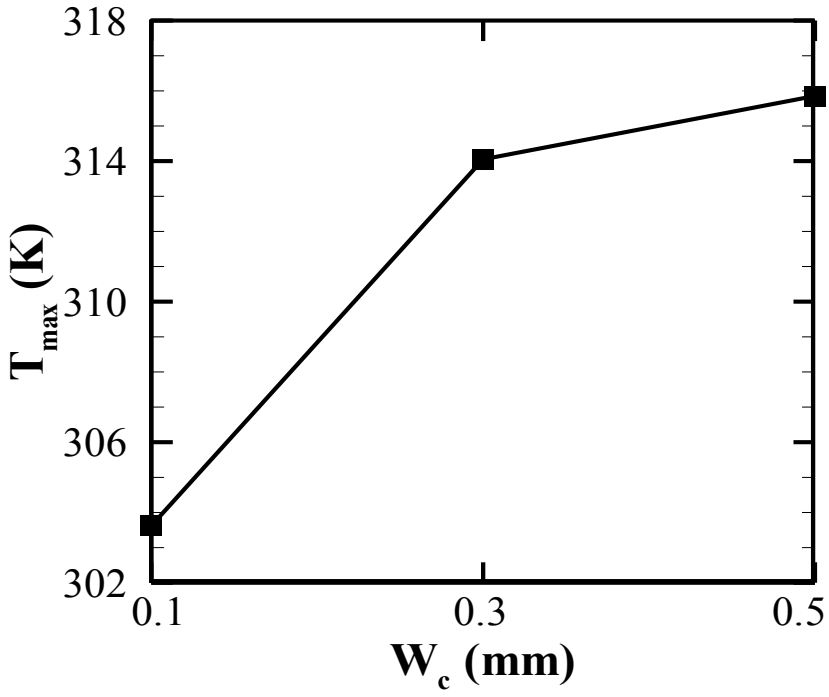

Figure. 5.22 The effect of width of channel (Wc, parameter B) on maximum temperature, H_c=0.5 mm

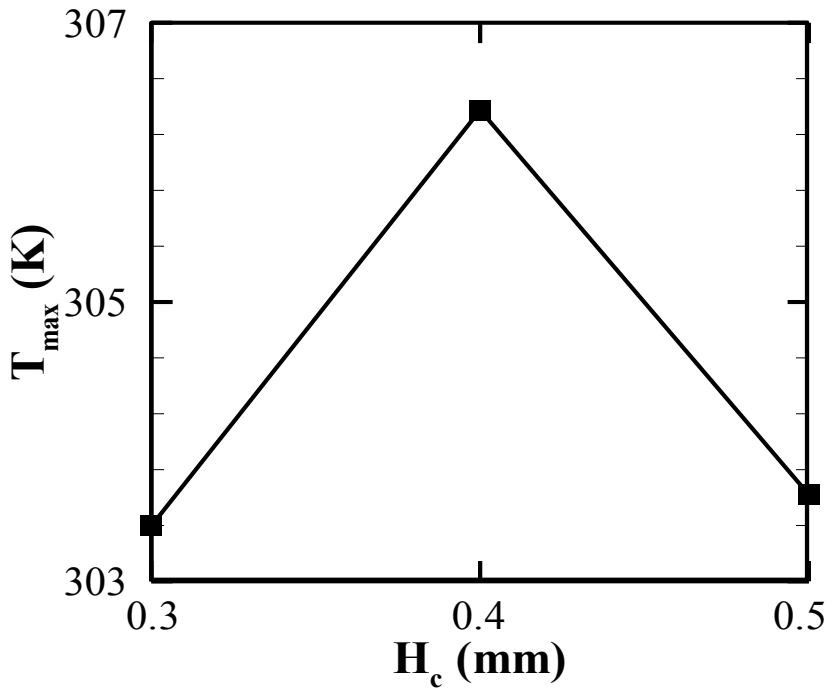

Figure. 5.23 The effect of height of channel (Hc, parameter C) on maximum temperature, W_c=0.1 mm

5.4.4 Cooling performance of the optimal designs

The cooling performances of the optimal heat sinks are simulated under different mass flow rate and compared in Figure.5.24-Figure.5.27. The maximum temperature of the bottom surfaces of the optimal heat sinks are shown in Figure.5.24 which decreases when increasing the inlet mass flow rate. The maximum temperature can be reduced to around 300 K with a mass flow rate of 90 g/min. This is because the heat transfer is enhanced by high fluid velocity. The optimal heat sinks are also able to keep the maximum temperature within the cooling objective range which is under 358 K under a very low mass flow rate. The trends of the maximum temperature for the optimal heat sinks

are similar with each other and are similar with the originally proposed heat sink. The benefit of increasing mass flow rate by reducing maximum temperature meets their common critical value at a mass flow rate of 40 g/min. Under the same mass flow rate, the optimal heat sink under q2 has the greatest maximum temperature because of the high heat flux. However, after the mass flow rate reaches the critical value, the difference between the maximum temperatures of three optimal heat sinks become smaller.

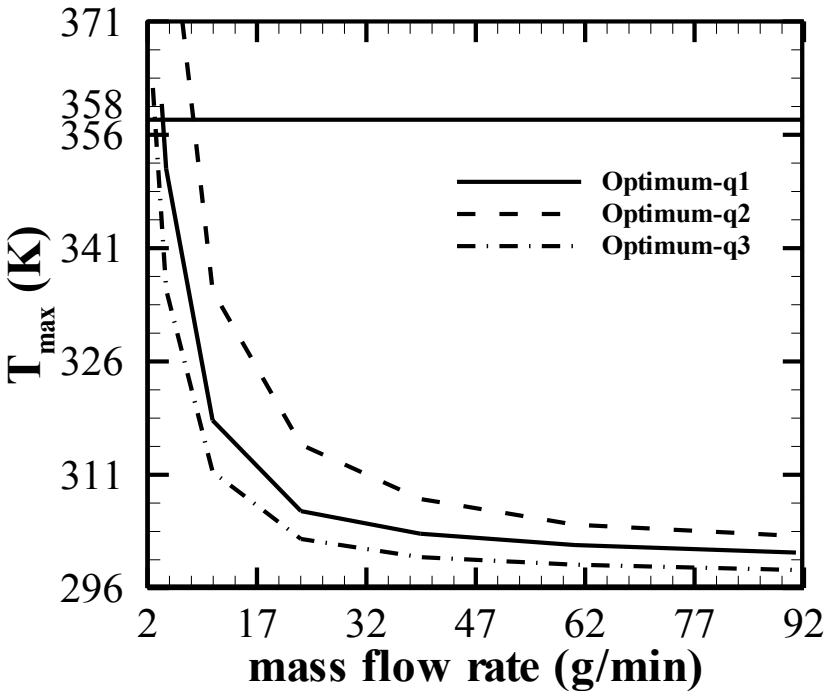

Figure. 5.24 Maximum temperature of optimal designs with various mass flow rate

As mentioned before, the temperature difference of the CPV cells is also an important factor for their working efficiency. Figure.5.25 presents the temperature difference of the optimal designs. For the three optimal heat sinks,

they are capable to reduce the temperature difference as low as 1.7 K over the bottom surface. The temperature differences of the three optimal designs are changing similarly to each other while differently from the original design which can be caused by the limit of the test range. For the optimal designs, the temperature differences have toughs under mass flow rates of 23, 40, and 60 g/min for q1, q2 and q3 respectively. The optimal design for heating condition q2 gives larger temperature variation on the bottom surface because of the high heat flux. For q3, the temperature difference on the bottom surface is even larger under low mass flow rate. Although the heat flux is decreasing along flow direction, the rate of decreasing is small; meantime, the cooling capacity is dropping due to increasing temperature of the fluid. Temperature rises drastically near the outlet plenum, which causes the large temperature difference. However, for the three optimal heat sinks, the minimum values for all heating conditions are almost identical.

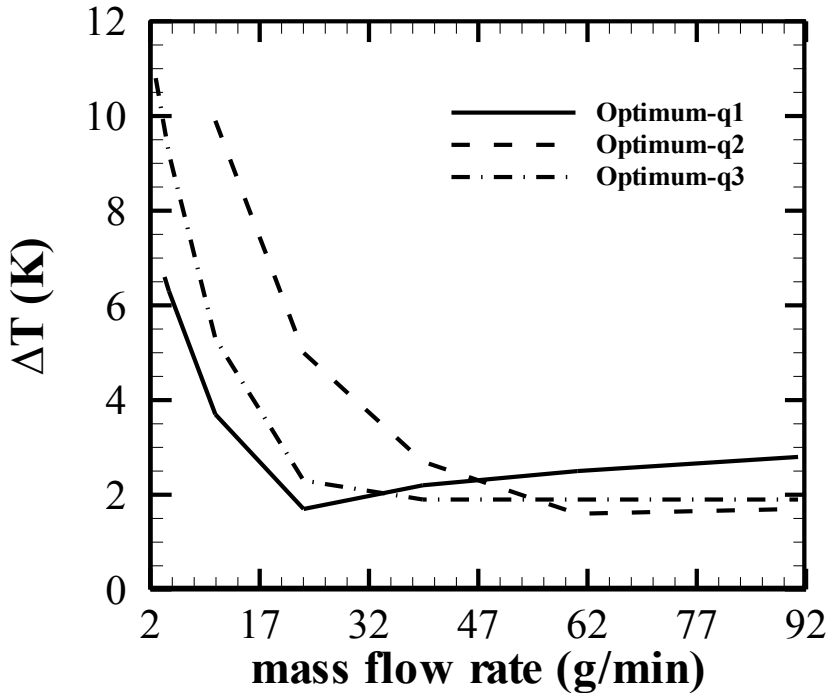

Figure. 5.25 Temperature difference of optimal designs with various mass flow rate

The curve for the dimensionless total thermal resistance is shown in Figure.5.26. The dimensionless thermal resistance is a function of channel geometric parameters calculated by Equation.5.3. Dimensionless thermal resistance decreases as mass flow rate is increased since heat transfer is enhance by high Reynolds number in the channels. Optimum heat sink under q1 and q3 maintains almost identical dimensionless thermal resistance; while for optimum design under q2, dimensionless thermal resistance is slightly higher. High heat flux leads to large thermal resistance of the heat sink. For the optimum design, thermal resistance remains steady under low heat fluxes.

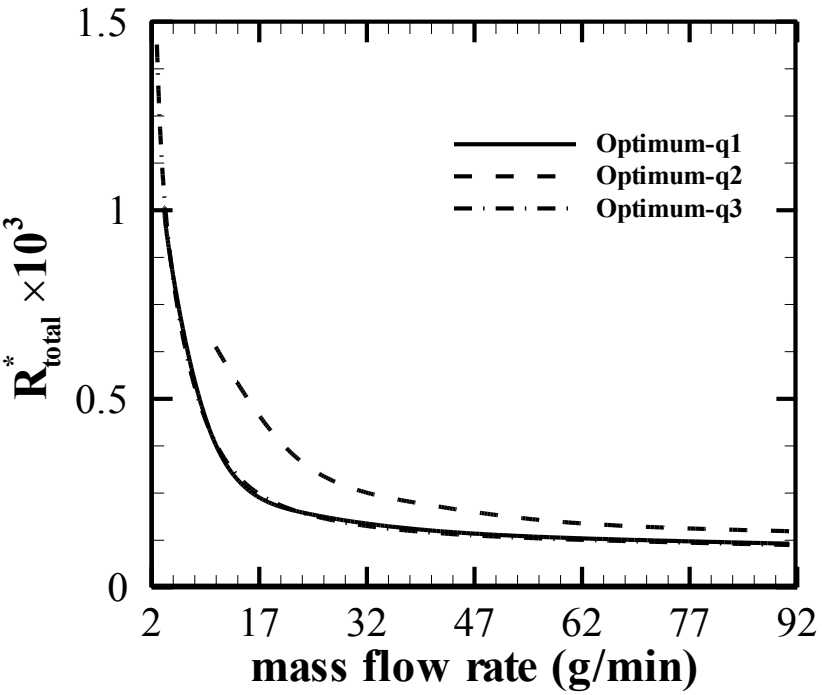

Figure. 5.26 Dimensionless total thermal resistance of optimal designs with various mass flow rate

The dimensionless pressure drop-Bejan number at the inlet increases almost linearly as mass flow rate rises as shown in Figure.5.27. Bejan number for the optimum designs depends only on the pressure drop of the heat sink because channel length is the same. High heat fluxes result in high fluid temperature with low viscosity therefore leads to small pressure drop in the optimum designs. A slight drop of Bejan number can be observed in the figure when increasing the heat flux on the bottom surface.

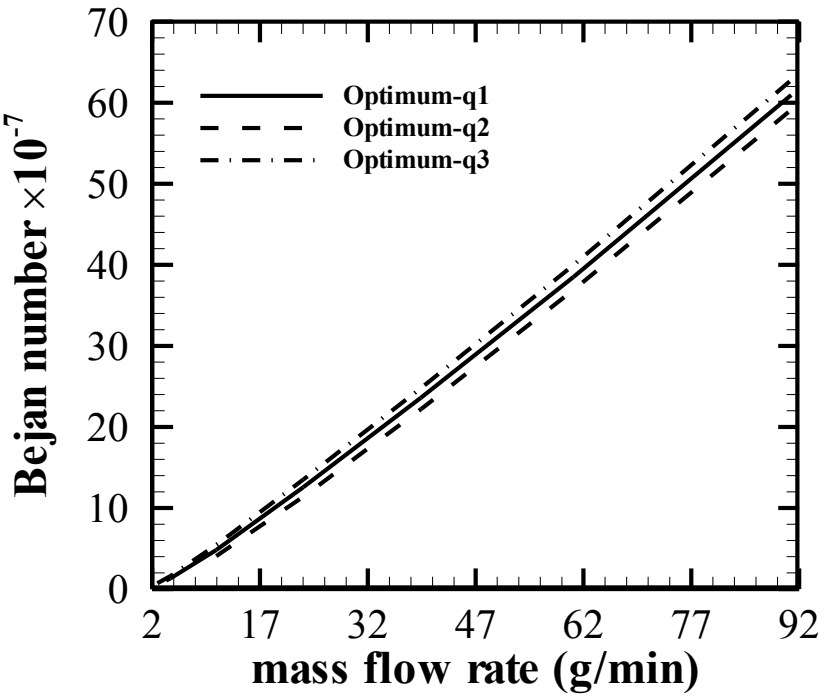

Figure. 5.27 Bejan number of optimal designs with various mass flow rate

The thermal efficiency is introduced for further understanding of the thermal performance of the optimum designs, which is the ratio of dissipated heat to the pumping power of the heat sink, as defined in Equation.5.6:

$$\eta_{eff} = \frac{\dot{Q}}{\dot{V} \cdot \Delta P} \tag{5.6}$$

where $\dot{Q}$ is the total heat dissipated by the coolant, $\dot{V}$ is the volume flow rate, ΔP is the pressure drop of the heat sink.

$\dot{Q}$ is calculated by:

$$\dot{Q} = \dot{V} \rho_f c_p (T_o - T_i) \tag{5.7}$$

where ρ_f and c_p are the density and specific heat capacity of the fluid at the average temperature. T_i and T_o are temperature of the fluid at the inlet and

outlet, respectively. They are obtained as the mass-weighted average temperature at inlet and outlet.

Substitute Equation.5.7 into Equation.5.6, then Equation.5.6 can be reduced into:

$$\eta_{eff} = \frac{\rho_f c_p (T_o - T_i)}{\Delta P} \tag{5.8}$$

The thermal efficiencies of the three designs are compared in Figure.5.28. The thermal efficiency of the heat sink is very high which means that the heat is dissipated with small pumping power requirement, especially at low mass flow rate where the pressure drop of the heat sink is extremely small. The thermal efficiency reduces greatly with the increase of the mass flow rate. The linearly increasing pressure drop and the decreasing outlet fluid temperature are the causes. Optimal heat sink under q2 maintains the highest thermal efficiency among all the three; while heat sink under q3 is the least efficient. The difference between the pressure drops of the three heat sinks is minor, but convective heat transfer is enhanced under high heat flux conditions which increases the heat dissipated by the heat sink. Consequently, the thermal efficiency is improved.

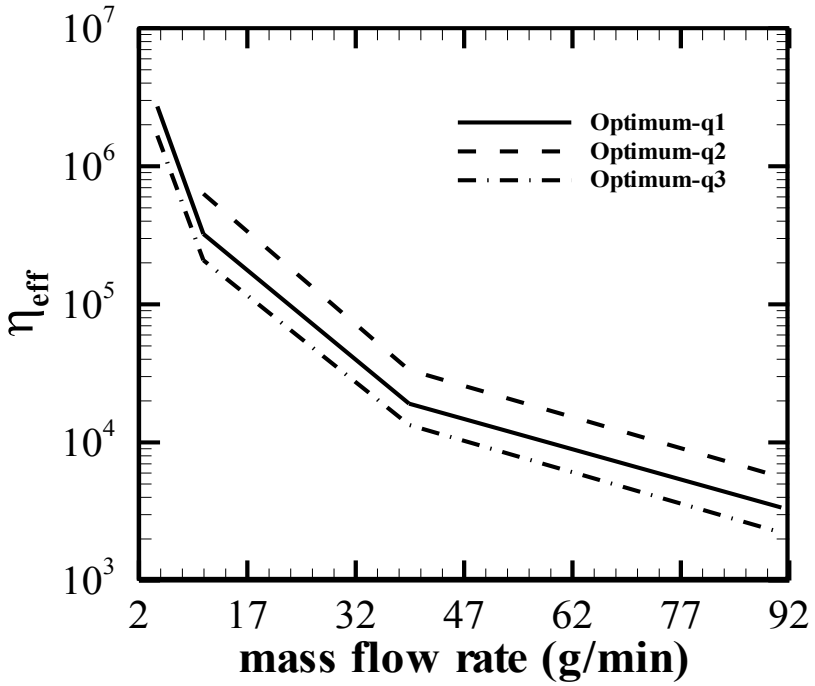

Figure. 5.28 Thermal efficiency of optimal designs with various mass flow rate

5.5 Summary

In this chapter, two heat sink layouts are proposed and their cooling performances are compared to remove continuously varying heat flux. Two heat flux conditions are tested under different mass flow rates. For both layouts, there is a critical value for mass flow rate beyond which mass flow rate has minor effects on temperature distribution of the heat sinks. Results also show that heat sink layout 2 presents better cooling performance than layout 1. Heat sink layout 2 maintains lower maximum temperature, temperature difference, and dimensionless pressure drop under both heating conditions. The overall average Nusselt number and thermal efficiency of layout 2 is much higher than that of layout 1. The dimensionless total thermal resistance for heat sink layout

2 is also smaller and less responsive to heat flux which means that layout 2 is more suitable for high heat flux conditions.

The geometry of heat sink layout 2 is also optimized under three continuously varying heat fluxes. Optimal designs are obtained using Taguchi method under each heating condition. For all optimal designs, the cooling performance is most sensitive to the width of channel (W_{ch}) and the optimal designs have the smallest channel width. Cooling performance of the optimal designs is similar but superior to that of original design.

Chapter 6 Cooling Performance of Swirl Channel Micro Heat Sink under Uniform and Continuously Varying Heat Flux

The swirl channel micro heat sink designed by Fan et al. (2010) is preliminarily studied using Fluent. The effects of channel curvature and channel number are studied under various uniform heat fluxes ranging from 10 W/cm^2 to 60 W/cm^2 and inlet velocities of 0.5 m/s and 1 m/s. It was found that high curvature and channel number improved the cooling performance of the heat sink. This chapter continues the study of the swirl channel micro heat sink with the higher curvature which was proposed by Fan et al. (2010) under different heating conditions. Firstly, the effect of cross sectional geometry on the cooling performance is studied with uniform heat fluxes applied on the bottom surface. Rectangular, trapezoidal, inverse-trapezoidal and isosceles triangular shaped channels are investigated. Secondly, the cross-sectional geometry which results in the best cooling performance is further tested under continuously varying heat flux.

6.1. Module Specifications

The complete module, shown in Figure.6.1, is 24 mm in diameter and 2.7 mm in height. There is a cylindrical expander with 4 mm in diameter placed at the

center of the heat sink. Ten channels are distributed equidistantly around the expander. The curvature of the channel is defined as:

$$x = Ut \cdot cos\omega t \tag{6.1}$$

$$y = Ut \cdot sin\omega t \tag{6.2}$$

Where x and y are coordinates; U is the radial velocity; ω is the angular speed; t is the time, which can be calculated by:

$$t = \frac{r}{U} \tag{6.3}$$

In this work, $U = 1\,mm/s$, $\omega = 5\,rad/s$. A 2 mm long tube (2 mm in diameter) is used as inlet for the heat sink which is at the center. The channel height is fixed at 0.5 mm and the base is 0.2 mm high.

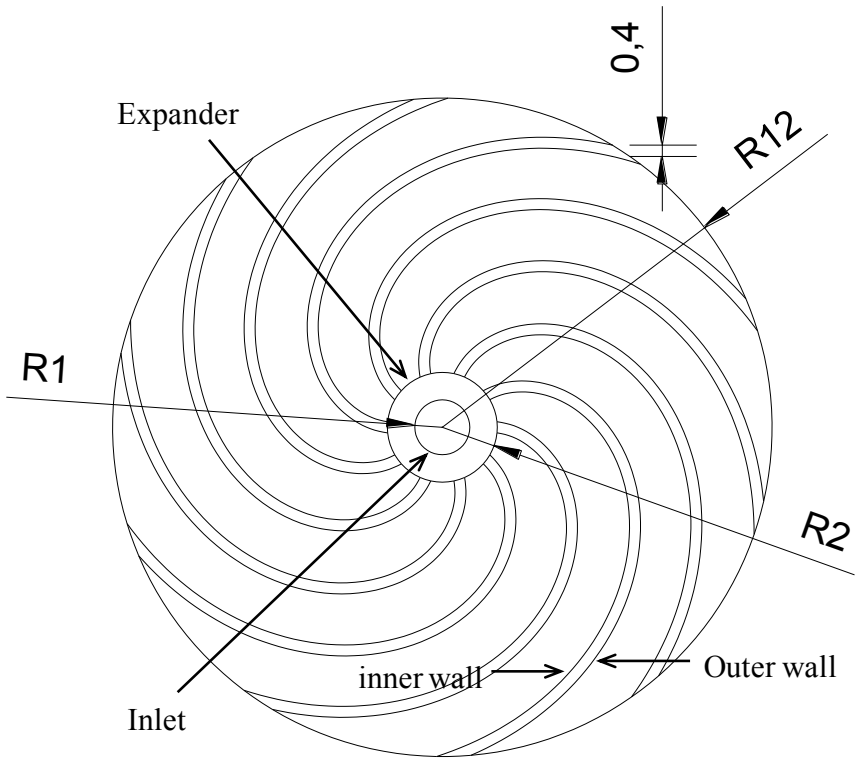

Figure. 6.1 Sketch of swirl channel micro heat sink (unit: mm)

Four cross sectional shapes are proposed which are rectangular, trapezoidal, inverse-trapezoidal and isosceles triangular. Figure.6.2 gives the sketch of a single channel for each design. The dimensions of the test module are summarized in Table.6.1.

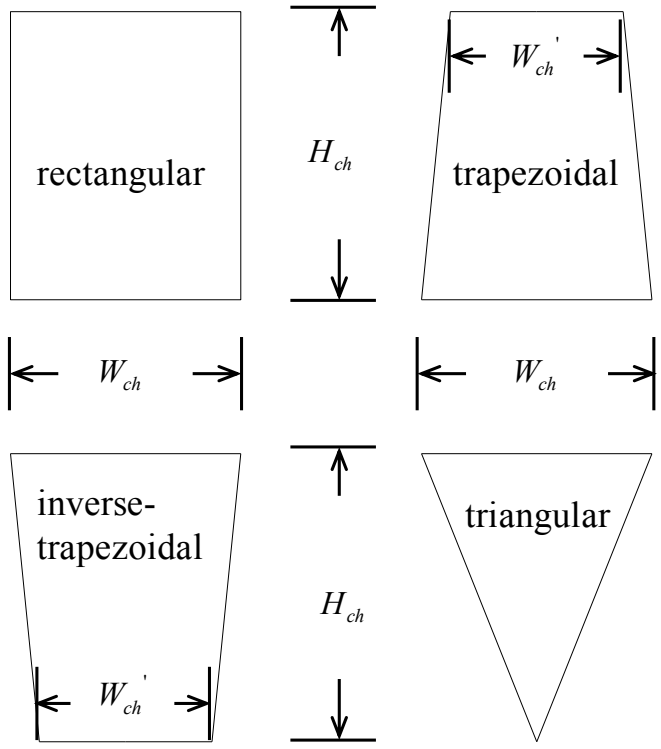

Figure. 6.2 Cross sectional geometries

Table. 6.1 Dimensions of various cross sectional geometries

Cross sectional geometries	Rectangular	Trapezoidal	Inverse-trapezoidal	Triangular
$W_{ch}\ (mm)$	0.4	0.4	0.4	0.8
$H_{ch}\ (mm)$	0.5	0.5	0.5	0.5
$W'_{ch}\ (mm)$		0.3	0.3	
$A_{ch}\ (mm^2)$	0.2	0.175	0.175	0.2
$D_h\ (mm)$	0.44	0.41	0.41	0.39

Under uniform heating conditions, the tested heat fluxes range from 10 W/cm^2 to 60 W/cm^2 with the same Reynolds number of 325 and 650 at the channel entrance for all four proposed cross sections. The inlet velocity is controlled to achieve the same Reynolds number at the channel entrance for different cross sections. Afterwards, the cross section with the best performance is studied under two types of continuously varying heat fluxes (linear and exponential) with inlet velocity varying from 0.5 m/s to 1 m/s which corresponds to inlet Reynolds number from 997 to 1994. The heat flux forms a concentric-circle pattern and decreases along radial direction. In positive radius direction, the heat flux distributions are:

$$q1 = 100 - (20/3)\,r \tag{6.5}$$

$$q2 = 80e^{-r/2} + 20 \tag{6.6}$$

The approach for simulation of the heat flux was described in section 3.1.3. Figure.6.3 shows the distribution curves of the two proposed continuously varying heat flux. The heat flux distribution on the bottom surface is presented in Figure.6.4

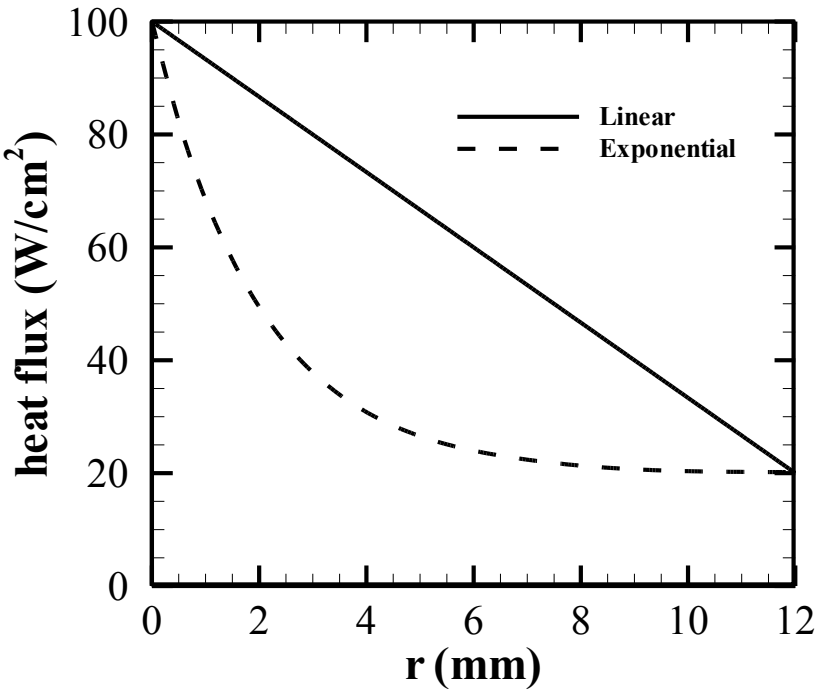

Figure. 6.3 Heat flux distribution

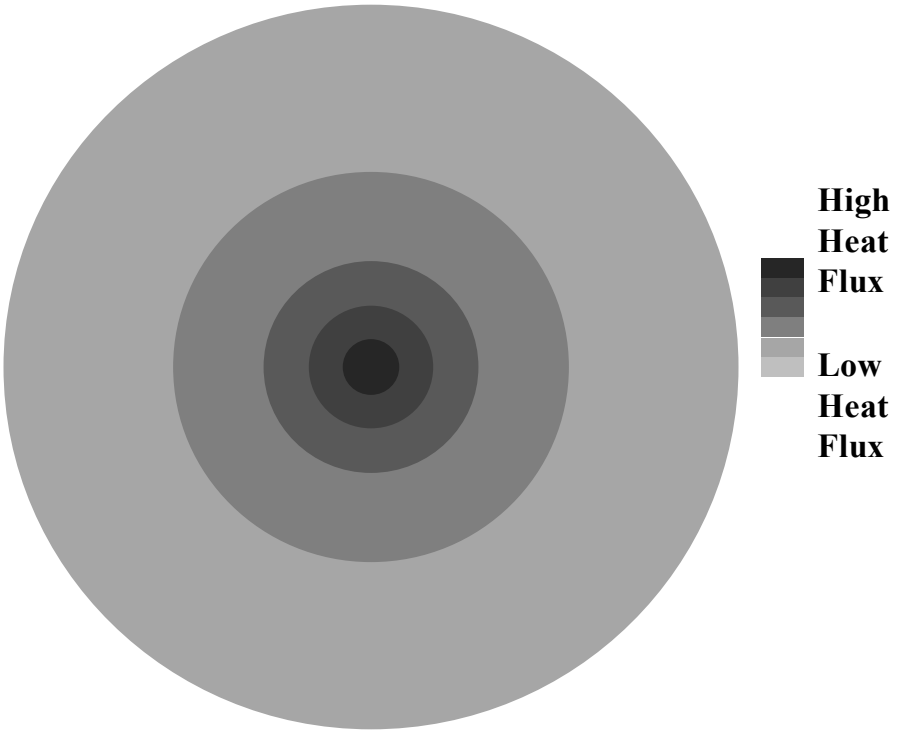

Figure. 6.4 Heat flux distribution on bottom surface

6.2. Mesh Independence

The swirl channel micro heat sink with rectangular channel is selected for the analysis of mesh independence. Unstructured mesh systems with 1.1 M, 1.65 M and 2.1 M cells are simulated under channel entrance Reynolds number of 325 and uniform heat flux of 10 W/cm^2 on the bottom surface. In Figure.6.5, a portion of the mesh at the expander is shown. The temperature and velocity distribution along the radius in the middle of the channel are presented in Figure.6.6 and Figure.6.7. Data obtained using meshes with 1.65 M and 2.1 M show almost the same distribution. As a result, the mesh with 1.65 M cells is considered sufficient for further simulations as it requires reduced computational time.

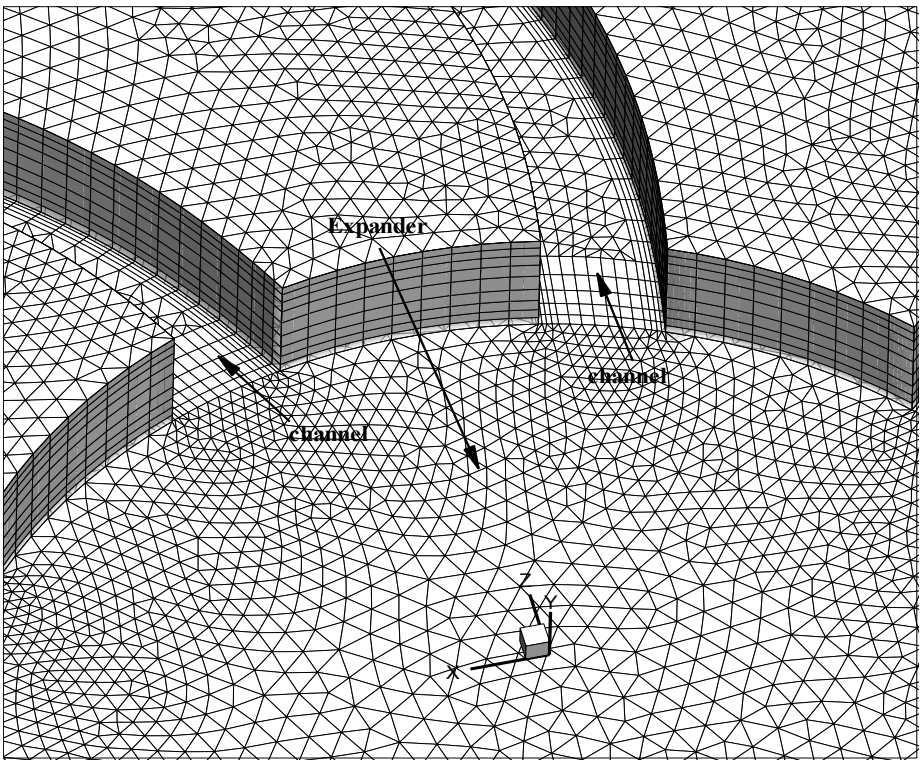

Figure. 6.5 Partial mesh at the expander

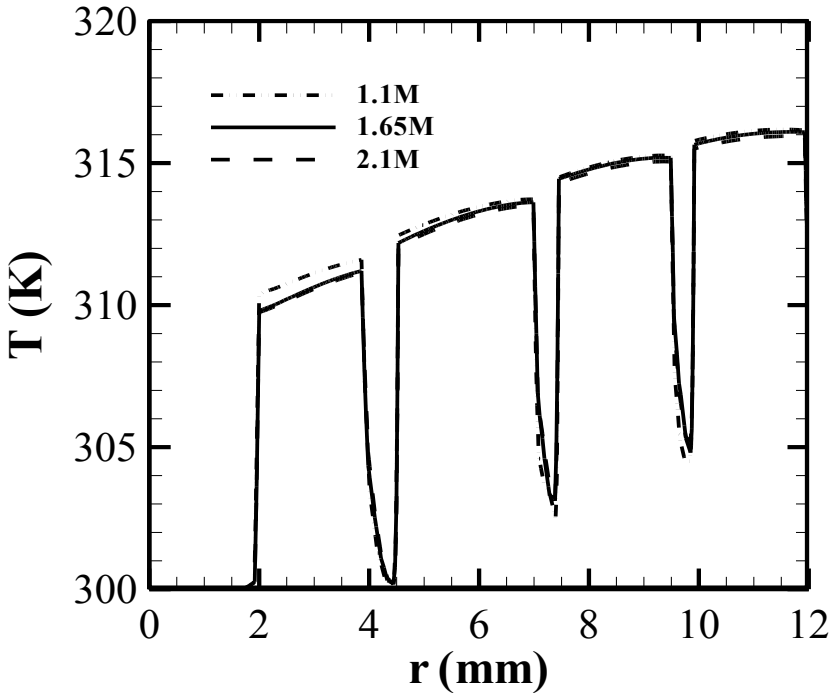

Figure. 6.6 Temperature distribution along the radius direction in the middle of the channel

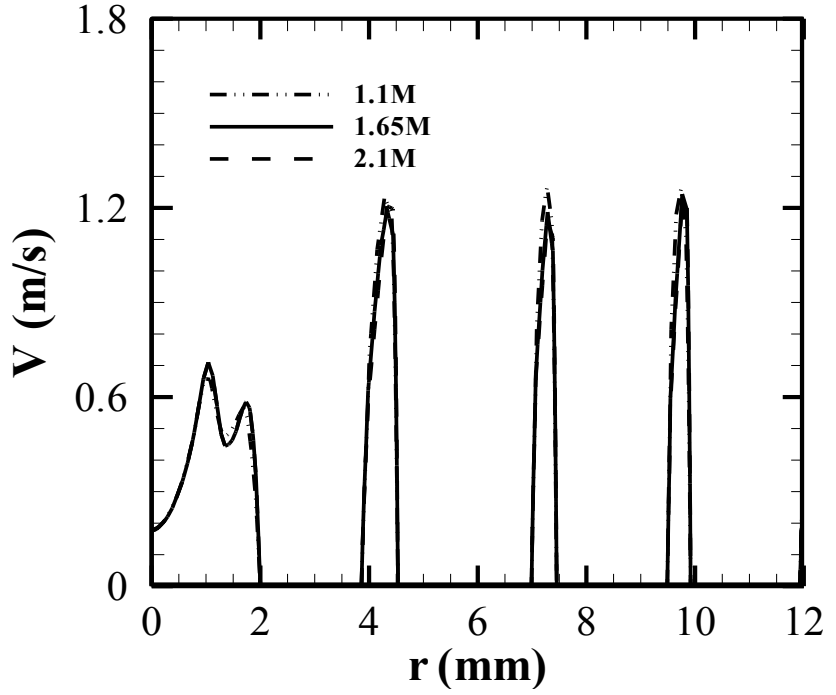

Figure. 6.7 Velocity distribution along the radius direction in the middle of the channel

6.3. Results and Discussion

6.3.1 Effects of Cross Sectional Geometry

6.3.1.1 Temperature distribution

The temperature contours of the bottom surface of the heat sink are shown in Figure.6.8 for different channel cross sections. The Reynolds number at the channel entrance is 325 and the uniform heat flux on the bottom surface is 10 W/cm^2. For all investigated cross sections, the temperature distribution on the bottom surface of the heat sink presents a shape of concentric circles. The increase of the fluid temperature causes a reduction of convective heat transfer between the walls and coolant along the flow direction. Thermal resistance of heat conduction in the solid phase increases along flow direction since the wall between two channels becomes thicker. Therefore, although heat flux decreases drastically along radial direction, the temperature of the heat sink keeps rising. The minimum temperature is at the center of the plate where the fluid temperature is low. At a certain radius, the lowest temperature is beneath the channels. This is a result of the shortest conduction distance between the heat source and coolant which leads to small conduction thermal resistance in the solid phase. Therefore, the region with maximum temperature appears between channels at the edge of the plate where fluid temperature is the highest and channels are farthest apart from each other. At a fixed radius, the temperature at the bottom surface beneath the outer wall of the channel is lower than that

beneath the inner wall. It is caused by the secondary flow which is due to the curvature of the channel. Figure.6.9 shows the pathlines in the channels from the bottom view of the heat sink. It can be found that secondary flow is in the clock-wise direction in the channel. From the bottom view, heat transferred to the outer wall is dissipated by main flow and secondary flow; thus the outer wall is able to maintain a lower temperature.

Different cross sectional geometries have significant effects on heat sink performances. The inlet velocity is controlled to maintain a certain Reynolds number at the entrance of the micro channels with different cross sections. With the same Reynolds number at the channel entrance, trapezoidal and inverse-trapezoidal channels have similar performances. Compared to the rectangular channel, they are less compact and less effective in packaging, which leads to larger thermal resistance in the solid phase. As a result, the maximum temperature is higher and the area with maximum temperature is larger. For the triangular channel, the width of the channel is twice as long as the other three which leads to a half of the distance between each two channels. Conductive thermal resistance is reduced in this case. With the same Reynolds number at the channel entrance, the maximum temperature for triangular channel is lower. The footprint of the channels with triangular shape is the largest among all. Therefore, temperature uniformity is also improved.

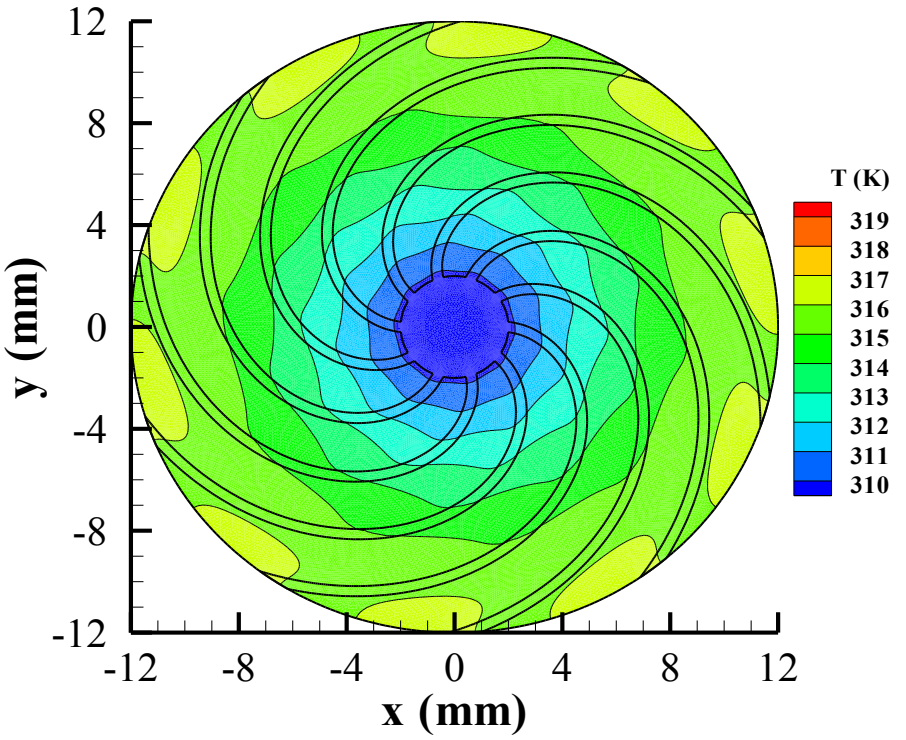

(a) rectangular

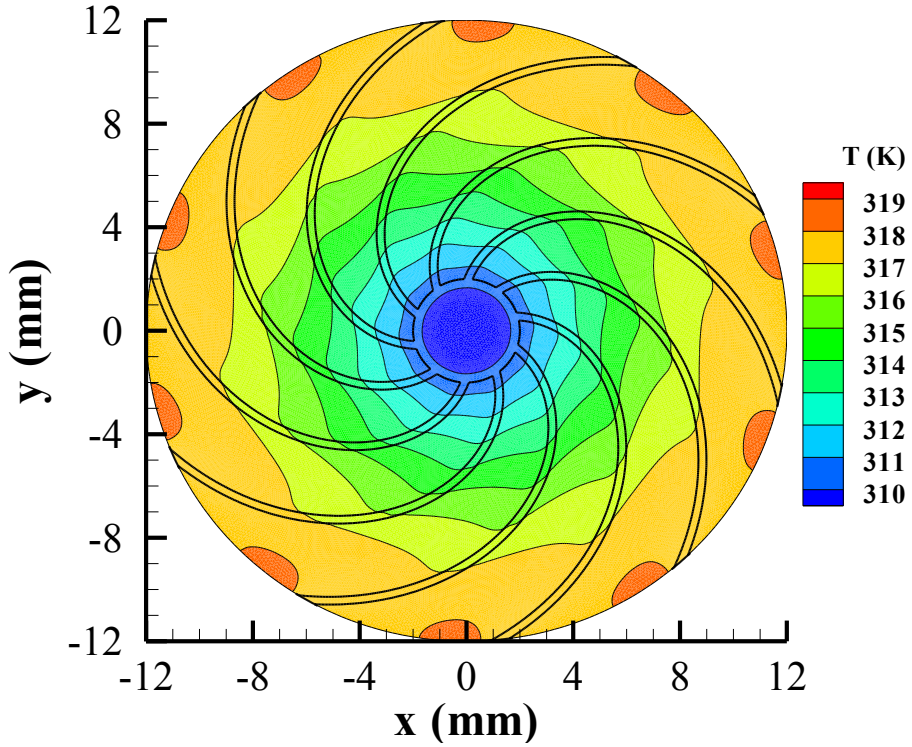

(b) trapezoidal

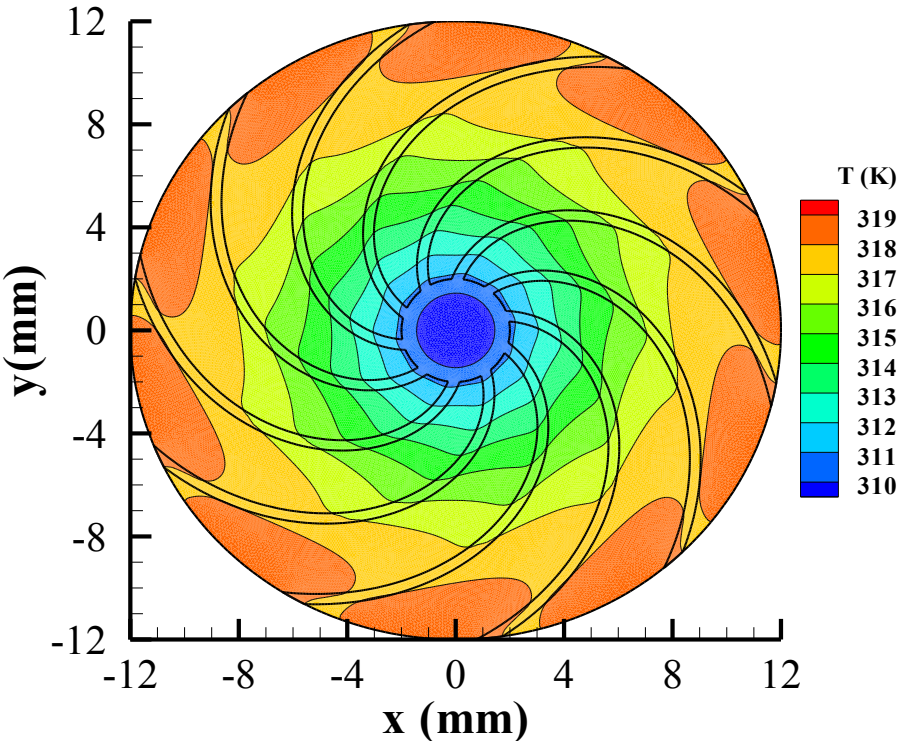

(c) inverse-trapezoidal

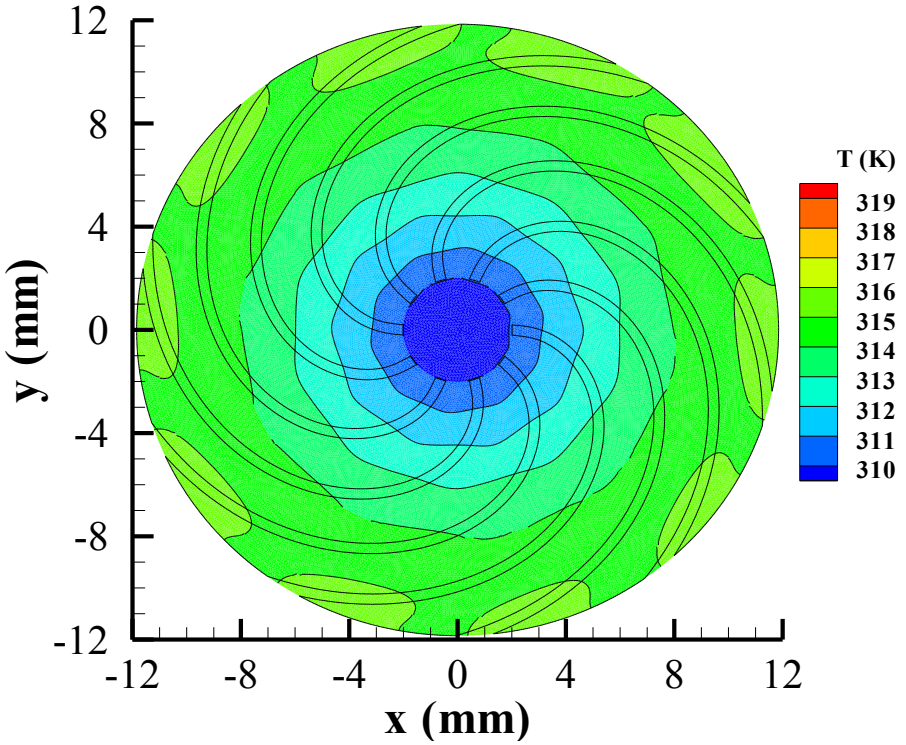

(d) isosceles triangular

Figure. 6.8 Temperature distribution on the bottom surface of the heat sink (a) rectangular channel (b) trapezoidal channel (c) inverse-trapezoidal channel (d) isosceles triangular channel

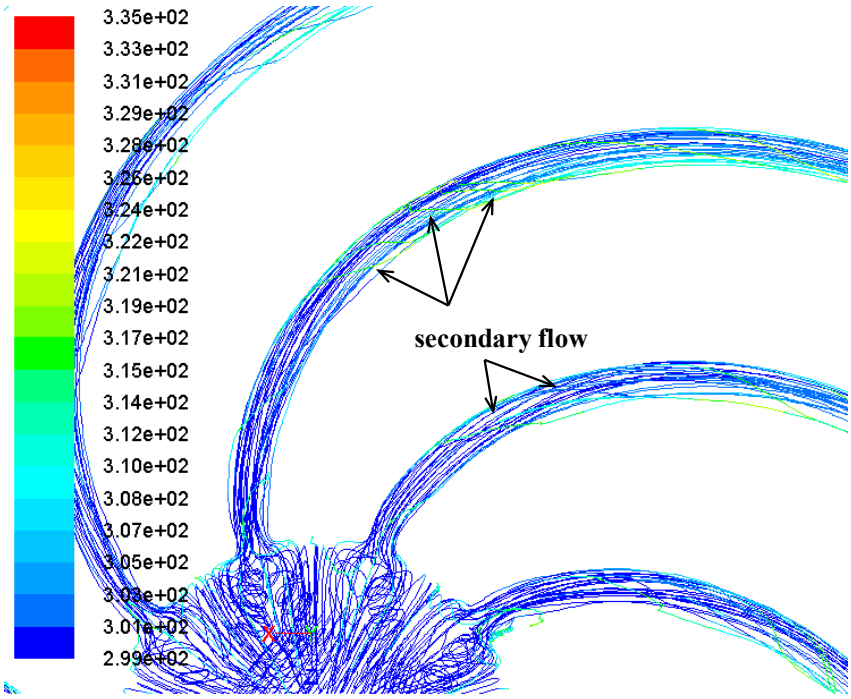

Figure. 6.9 Pathlines of fluid in rectangular channel

6.3.1.2 Maximum temperature

Figure.6.10 quantifies the maximum temperature on the bottom surface for the four investigated cross sectional geometries of the heat sink at tested Reynolds number. For Reynolds number of 325 at channel entrance, fluid boiling occurs when a heat flux of 60 W/cm^2 is applied to the bottom. Increase in the Reynolds number enhances convective heat transfer, so that the maximum temperature is reduced. Accordingly, maximum tested heat flux applied to the heat sink can be raised to 60 W/cm^2 when Reynolds number at the channel entrance is increased to 650. All cross sectional geometries are able to maintain the maximum temperature less than 100 °C except the inverse-trapezoidal channel. Results show a linear relationship between the maximum temperature and the heat flux

for all cross sections. Triangular channels maintain the lowest maximum temperature among the four. It also has the smallest slope which means that the effect of heat flux on maximum temperature is the least significant. The advantage of the triangular channels is more noticeable at lower Reynolds number. The triangular channel fills the solid volume most efficiently among the four, thereby reducing the conductive thermal resistance in the solid phase. The trapezoidal and inverse-trapezoidal channels show the similar performance. The trapezoidal channel is inferior to rectangular and triangular channels but superior to inverse-trapezoidal channels. The hydraulic diameters and Reynolds numbers of all four channels are almost identical which leads to very similar heat transfer coefficient. However, the layouts of trapezoidal and inverse-trapezoidal channels are less compact which causes a larger conduction thermal resistance thus results in a higher maximum temperature. Their slopes are also greater than that of the rectangular and triangular channels.

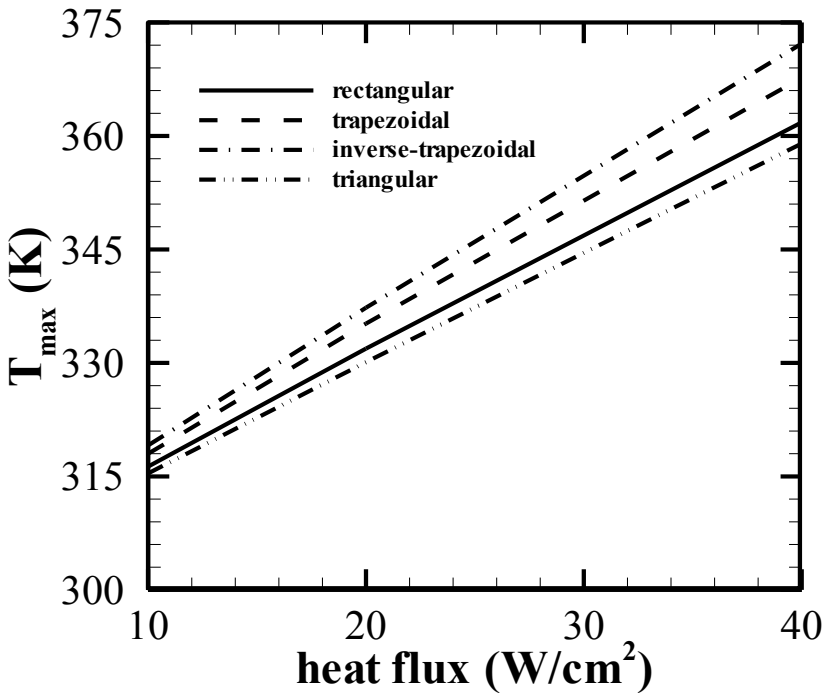

(a) Re=325

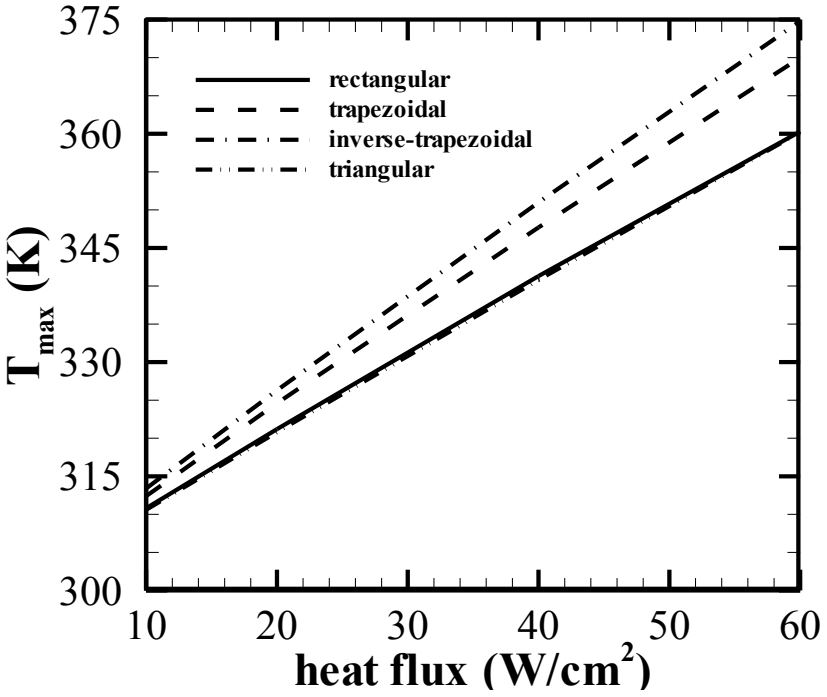

(a) Re=650

Figure. 6.10 Maximum temperature (a) Re=325 (b) Re=650

6.3.1.3 Temperature difference

The temperature difference, which is the difference between the maximum and minimum temperature on the bottom surface, presents the temperature uniformity. It also has a linear relationship with the heat flux, as shown in Figure.6.11. The temperature difference increases linearly with the heat flux and the slope reduces with high Reynolds number at the inlet of the channels since convective heat transfer is enhanced. Triangular channel gives the best temperature uniformity among all and it is not as responsive as others to heat flux due to the large footprint of the channels. Rectangular and trapezoidal channels have the second and third best performance respectively. Inverse-trapezoidal channel has the highest temperature difference, which increases most rapidly with the heat flux.

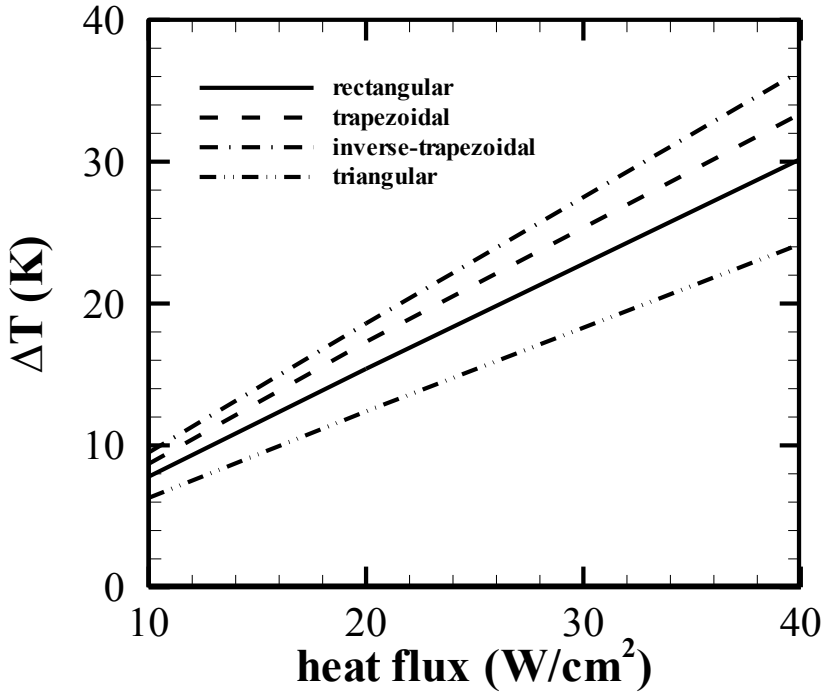

(b) Re=325

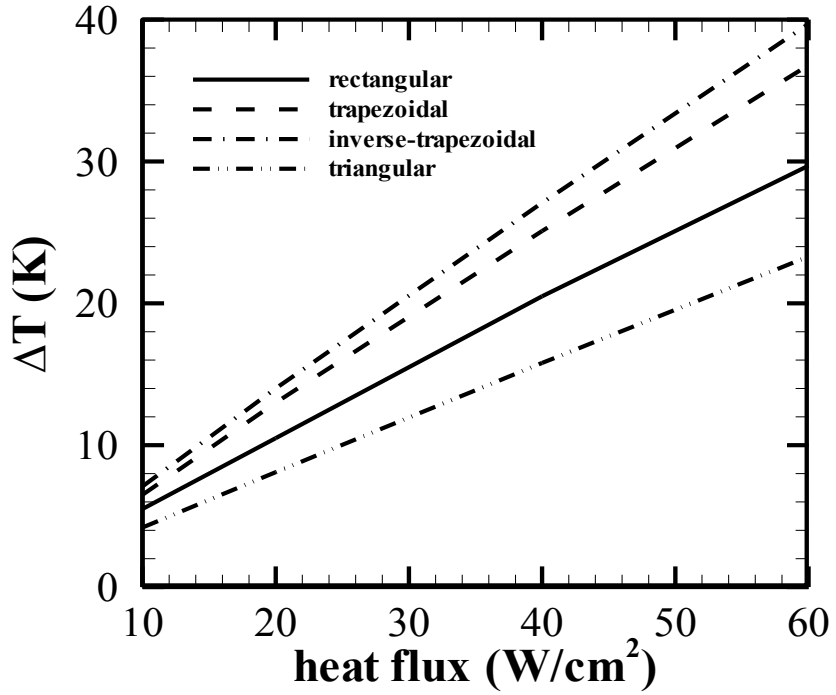

(a) Re=650

Figure. 6.11 Temperature difference (a) Re=325 (b) Re=650

6.3.1.4 Overall average Nusselt number

The overall average Nusselt numbers of the four cross section geometries are calculated by Equation.5.4 and Equation.5.5. The average Nusselt numbers are compared in Figure.6.12 under different heat flux conditions. Increasing heat flux and Reynolds number increases the overall average Nusselt number for all four designs. Convective heat transfer coefficient is increased by high heat flux and high Reynolds number; hence the average Nusselt number is improved as well. Among the four proposed cross sections, the rectangular channel maintains the highest Nusselt number at all time. Trapezoidal and inverse-trapezoidal channels directly follow. The overall average Nusselt

number for the triangular channel is the lowest.

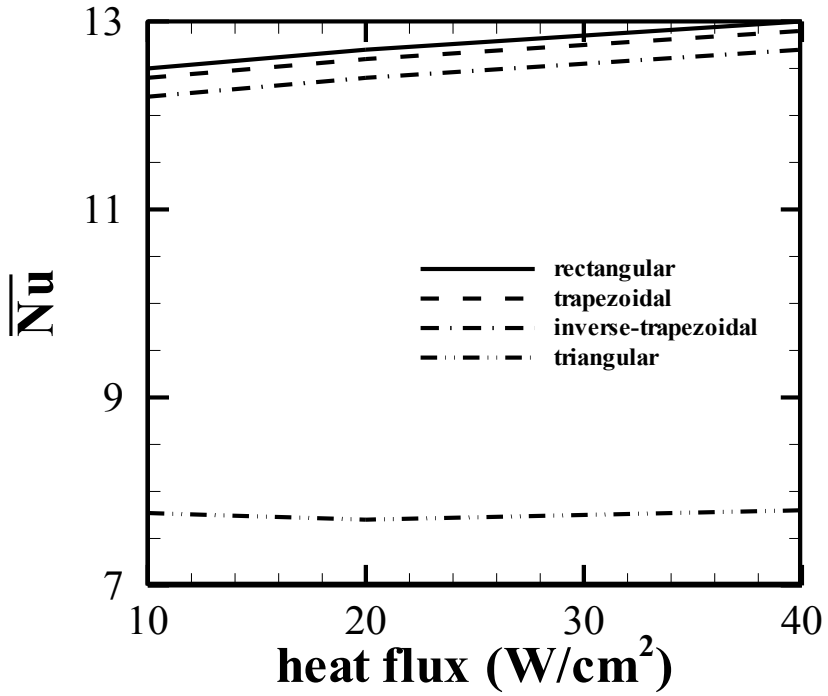

(c) Re=325

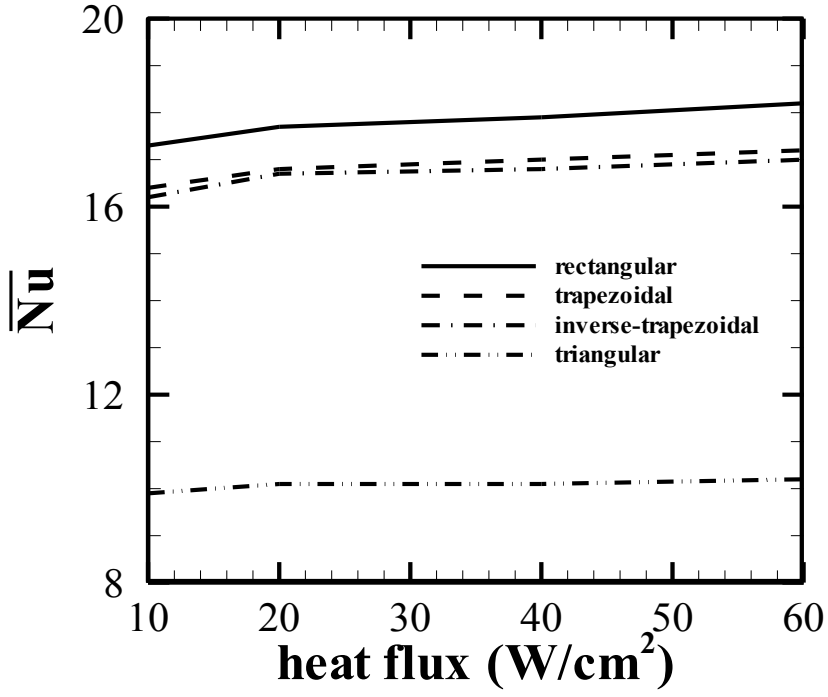

(d) Re=650

Figure. 6.12 Overall average Nusselt number (a) Re=325 (b) Re=650

6.3.1.4 Pressure drop

The pressure drop for the heat sinks with different cross sectional geometries and various inlet velocities is presented in Figure.6.13. The pressure drop for fully developed laminar flow can be calculated in the form of:

$$\Delta P = \frac{f \cdot Re_{D_h} \cdot L \cdot \mu \cdot \bar{V}}{2D_h^2} \tag{6.8}$$

Where f is the friction factor, Re_{D_h} is the Reynolds number, L is the length of the channel, μ is the dynamic viscosity of water, $\bar{V}$ is the mean velocity in the channel, and D_h is the hydraulic diameter of the channel.

A slight decrease in the pressure loss is observed when increasing the heat flux. Because the water properties are temperature dependent, the dynamic viscosity decreases slightly with increasing fluid temperature. The pressure drop in the heat sink with triangular channels is lower than that of the other three. For the triangular channel, the cross sectional area is significantly increased than the others along the flow direction. Hence the fluid velocity reduces, as well as the average velocity in the channel. From Equation.6.8, it is obvious that the low average fluid velocity causes the small pressure drop in the triangular channel. Results for trapezoidal and inverse-trapezoidal channels are almost identical since they have similar geometry.

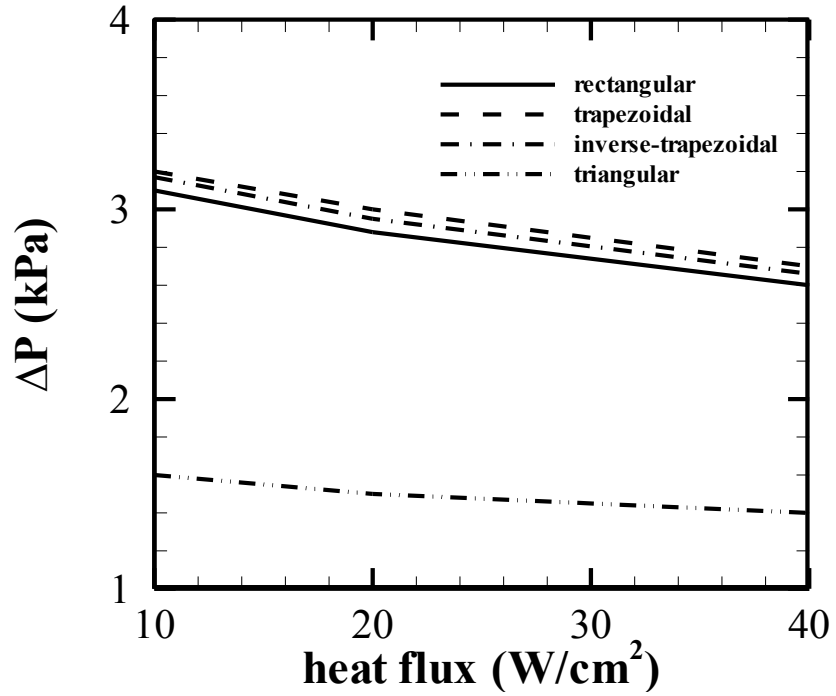

(a) Re=325

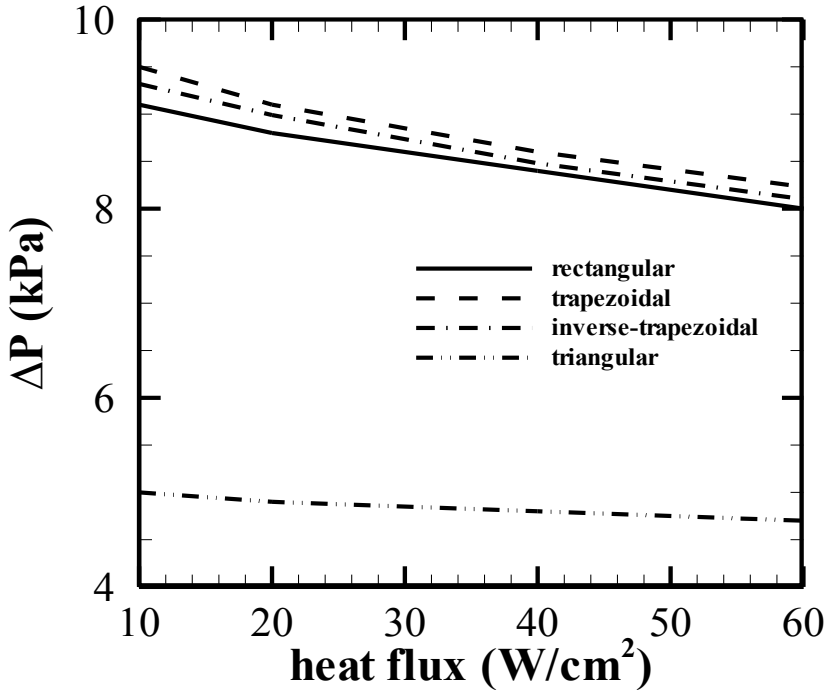

(b) Re=650

Figure. 6.13 Pressure drop (a) Re=325 (b) Re=650

6.3.1.6 Thermal efficiency

The thermal efficiency for each cross section is calculated by Equation.5.8 and compared in Figure.6.14. They are presented as the ratio to the thermal efficiency of the rectangular channel. For the rectangular and inverse-trapezoidal channels, the effects of the heat flux and Reynolds number are minor. However, for the trapezoidal channel, the ratio increases while for the triangular channel, the ratio decreases with increase in the heat flux. The thermal efficiency of the triangular channel is the highest because the pumping power needed which corresponds to the pressure drop is the lowest among all. The trapezoidal channel is the second best.

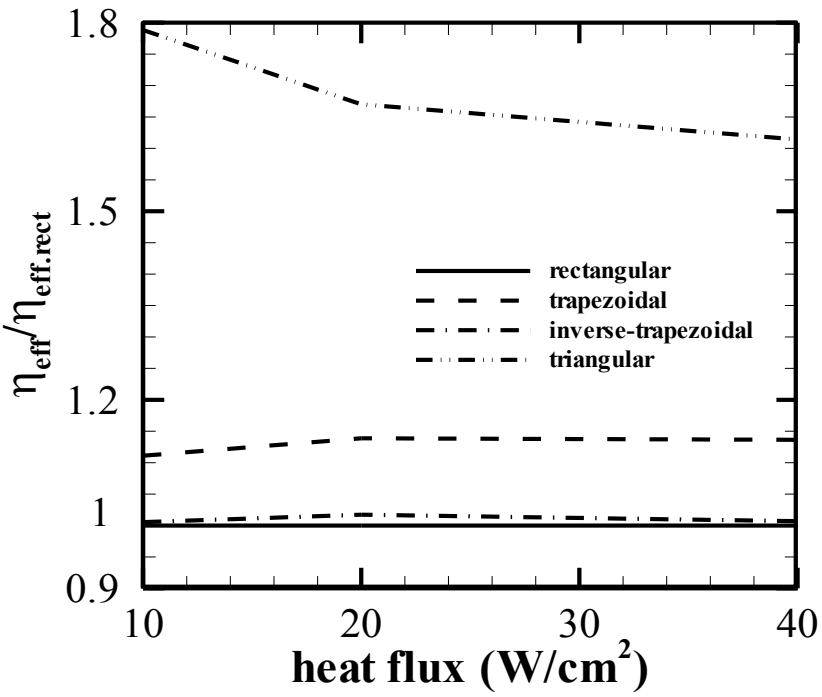

(e) Re=325

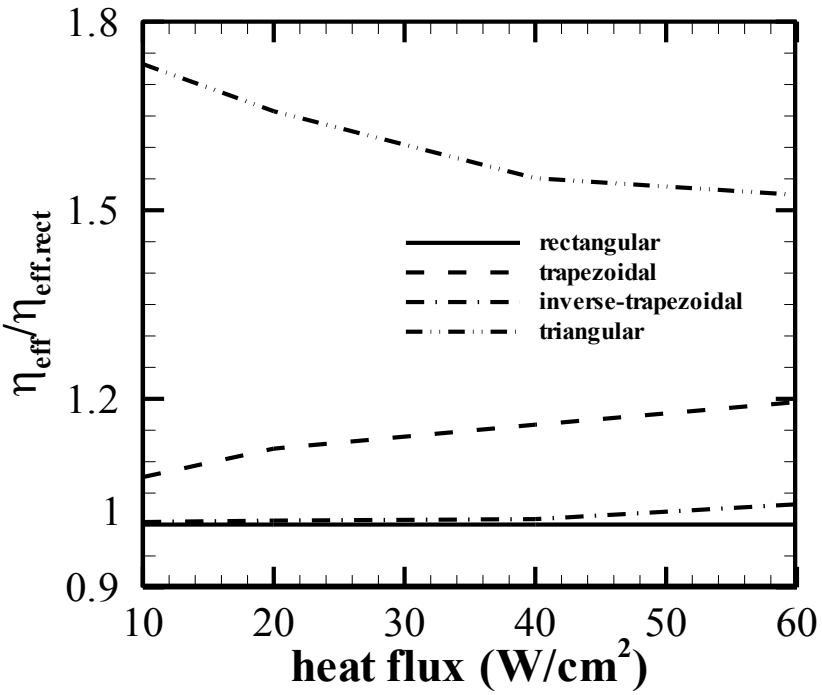

(f) Re=650

Figure. 6.14 Thermal efficiency (a) Re=325(b) Re=650

6.3.1.5 Total thermal resistance

The total thermal resistance is the criteria used to determine the cooling capacity of a heat sink. It is calculated by the following equation:

$$R_{total} = \frac{T_{max} - T_{min}}{\pi r^2 \cdot \dot{q}} \tag{6.9}$$

Where T_{max} and T_{min} are the maximum and minimum temperature of the whole module, respectively; $\pi r^2 \cdot \dot{q}$ is the total heat supplied to the bottom surface.

The results are presented in Figure.6.15. For all cross sections, the thermal resistance reduces with an increase of the Reynolds number because convective

heat transfer is enhanced. A greater amount of heat can be dissipated by the heat sink. The heat flux has a minimal effect on thermal resistance. The triangular channel maintains the lowest thermal resistance under all of the investigated cases. It is resulted from the small conductive thermal resistance in the solid phase due to small wall width.

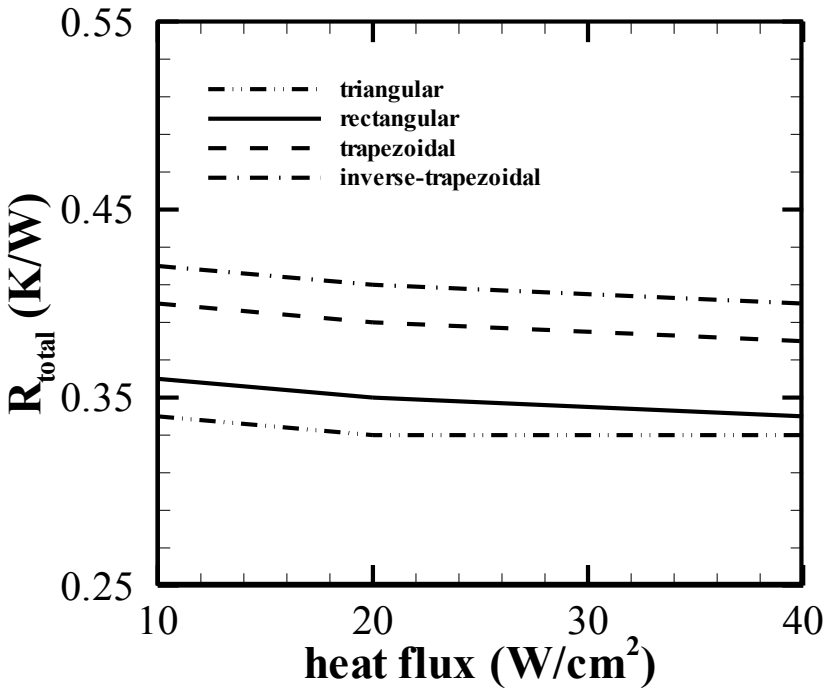

(g) Re=325

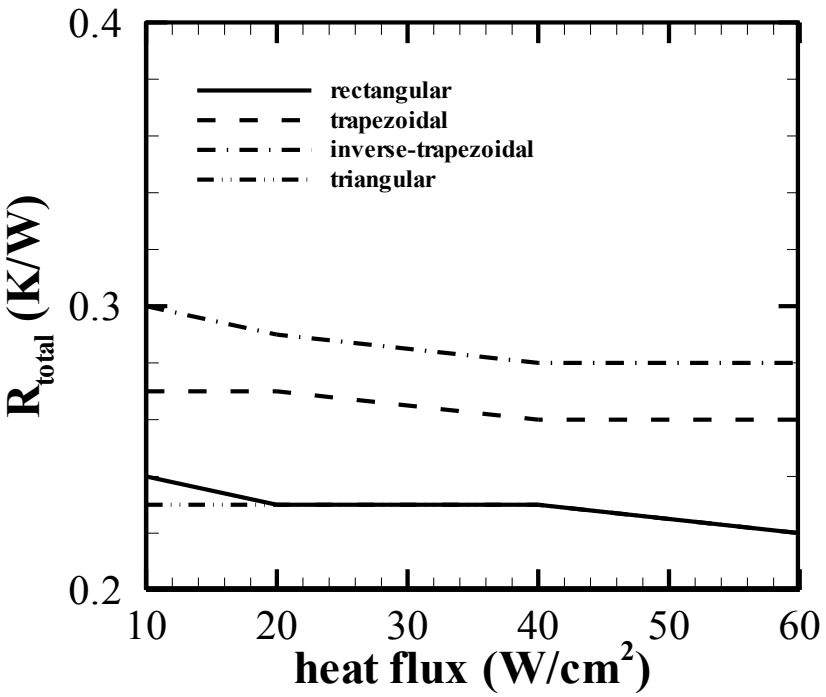

(h) Re=650

Figure. 6.15 Total thermal resistance (a) Re=325 (b) Re=650

6.3.2 Cooling performance under non-uniform heat flux conditions

From the results in section 6.3.1, it can be concluded that under uniform heating, the triangular channel was shown to provide the lowest maximum temperature and the best temperature uniformity. The consumption of pumping power which is corresponding to the pressure drop is also the smallest. Therefore, the swirl channel micro heat sink with triangular channels is chosen for the study under non-uniform heat flux conditions. Results are compared to the heat sink with the same amount of heat applied uniformly on the bottom surface.

6.3.2.1 Continuously varying heat flux condition with linear variation

When continuously varying heat flux with a linear variation is applied to the heat sink, the temperature distribution on the bottom surface of the heat sink with inlet Reynolds number of 997 is shown in Figure.6.16. The area with maximum temperature is closer to the center of the bottom surface while it appears at the edge for uniform heating conditions. At medium radius, the fluid temperature is higher than that under uniform heating conditions whilst heat flux is twice as much. Heat transfer coefficient is low in the area and thus the maximum temperature appears. At the edge, the low heat flux can be removed by coolant although the fluid temperature is even higher.

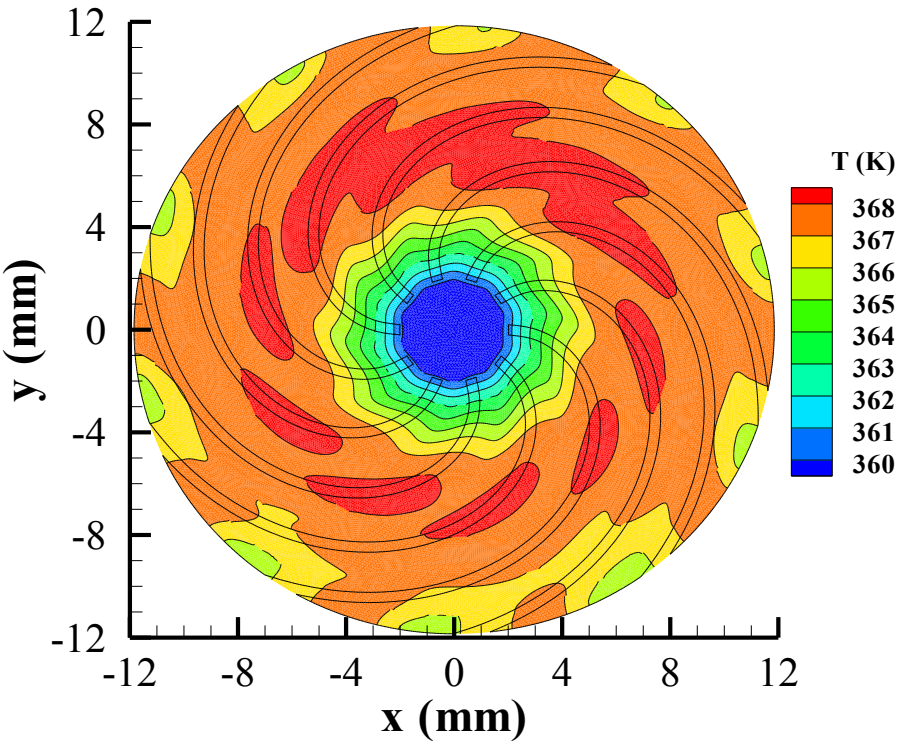

Figure. 6.16 Temperature distribution on the bottom surface Re=997

Figure.6.17 shows the effect of the inlet Reynolds number on maximum temperature under two heating conditions. Increasing the inlet Reynolds number leads to a lower maximum temperature due to enhanced convective heat transfer in the channels. Uniform heating condition leads to a higher maximum temperature than that under non-uniform heating condition at a given inlet Reynolds number. Under non-uniform heating, temperature uniformity is also significantly improved, especially under low inlet Reynolds number (as shown in Figure.6.18). Since the heat flux reduces along radial direction, it compensates for the decrease in heat transfer coefficient caused by increasing fluid temperature. Thus a smaller temperature difference is obtained.

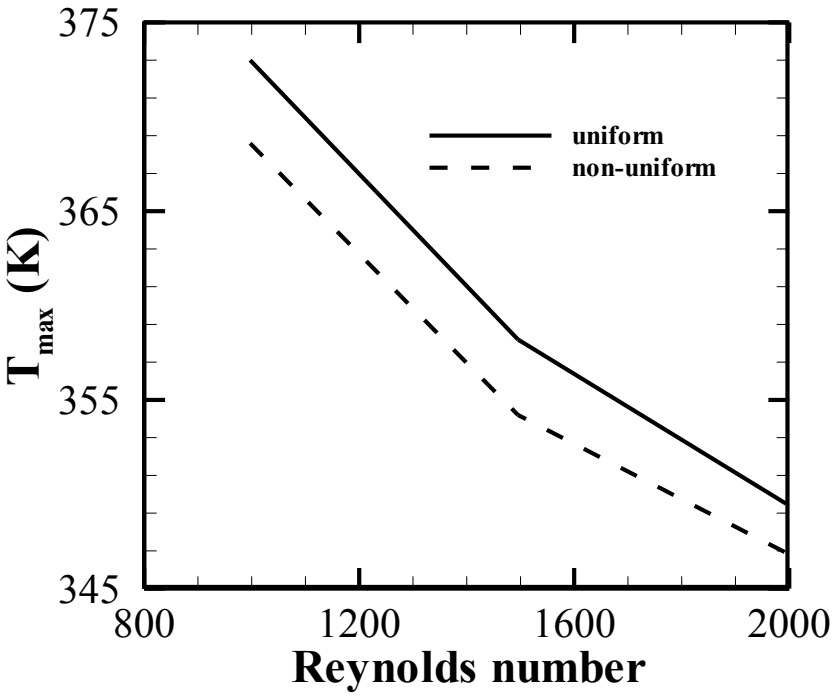

Figure. 6.17 Maximum temperature

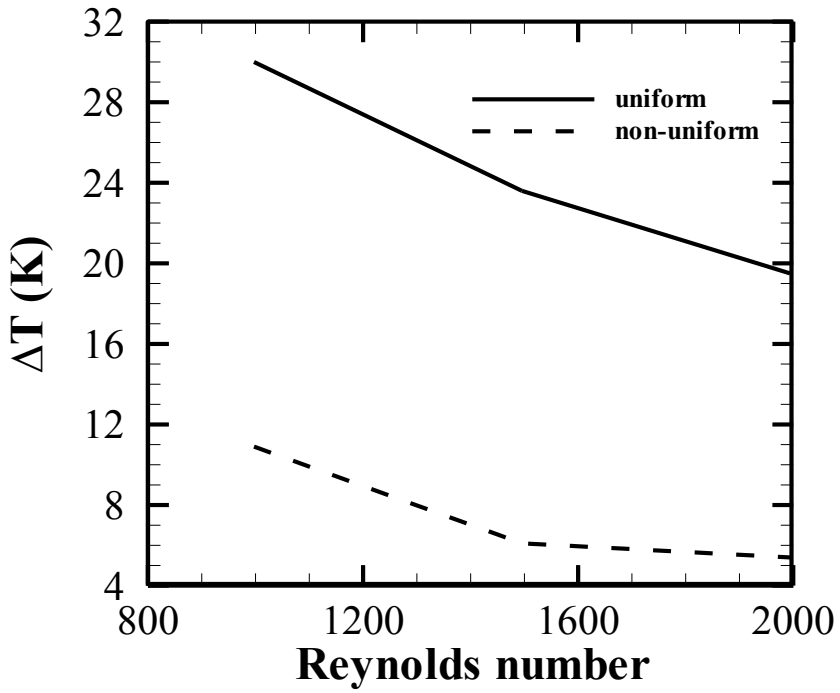

Figure. 6.18 Temperature difference

Figure.6.19 presents the pressure drop of the heat sink under different heating conditions with various inlet Reynolds numbers. An increase in the inlet Reynolds number raises the pressure drop for fluid average velocity is increased in the micro channel which is also supported by Equation.6.9. The pressure drop is slightly affected by heat fluxes, as can be observed in Figure.6.19. The same amount of heat is applied to the heat sink bottom surface, and the maximum temperature of uniform heating is larger. According to energy balance, the fluid temperature is lower under uniform heating which causes a slightly larger dynamic viscosity. Therefore a higher pressure drop is obtained.

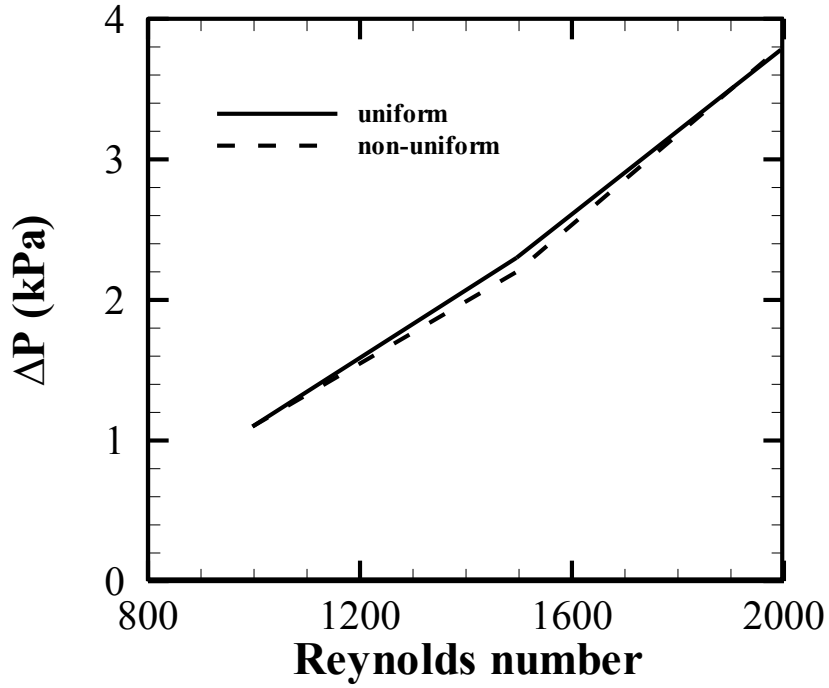

Figure. 6.19 Pressure drop

The overall average Nusselt numbers of the heat sink under uniform and non-uniform heating conditions are compared with various inlet Reynolds number in Figure.6.20. The increase of Reynolds number results in a higher Nusselt number under both heating conditions. However, the increment of the Nusselt number reduces. The overall average Nusselt number for heat sink under uniform heating is higher than that under non-uniform heating. It is due to higher wall temperature under uniform heating condition which enhances conductive heat transfer between the wall and the fluid.

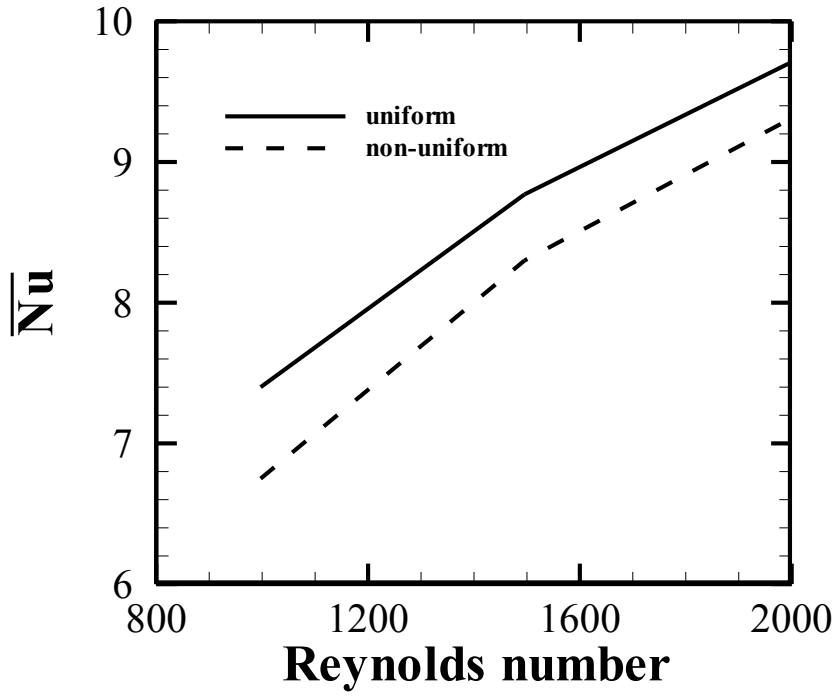

Figure. 6.20 Nusselt number

The dimensionless total thermal resistance based on channel geometry is calculated by Equation.5.3 and presented in Figure.6.21. The dimensionless thermal resistance is reduced when the inlet Reynolds number increases. As a result, at high Reynolds number, the cooling capacity of the heat sink becomes larger. The dimensionless thermal resistance is greater when the heat sink is under uniform heat flux conditions.

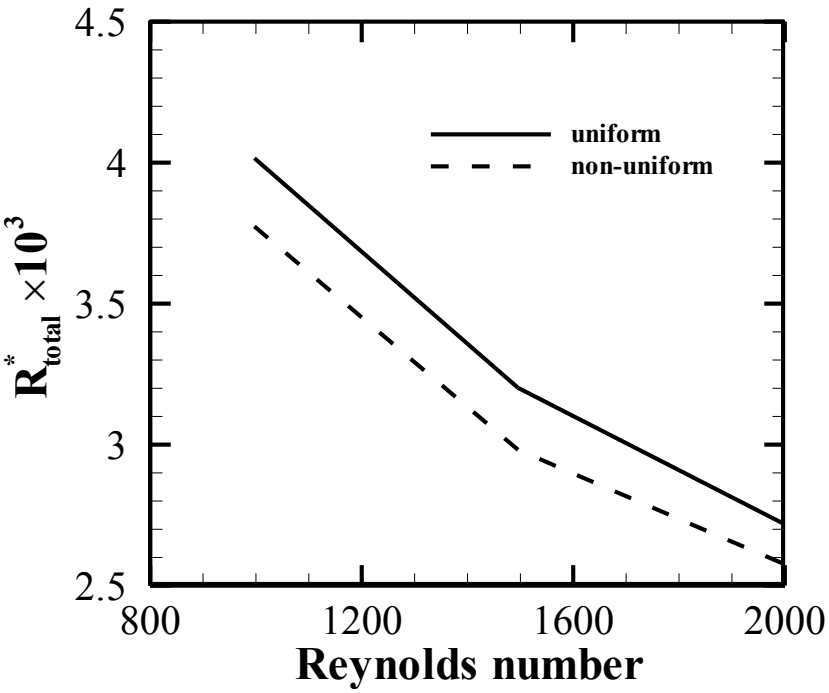

Figure. 6.21 Dimensionless total thermal resistance

6.3.2.2 Continuously varying heat flux condition with exponential variation

The contour of temperature distribution on the bottom surface is shown in Figure.6.22 with inlet Reynolds number of 997. The region with maximum temperature is at the edge and in between two channels, which is similar to the results under uniform heating. The total heat is lesser and the heat flux reduces much more quickly compared to the linear varying heat flux. At the edge of the heat sink, although the heat flux is small, the fluid temperature is high, and the fluid velocity is also low due to enlarged cross sectional area of the channel. Local Reynolds number is small and diminishes convective heat transfer. Heat flux cannot be removed efficiently hence causes the maximum temperature to

occur in this region.

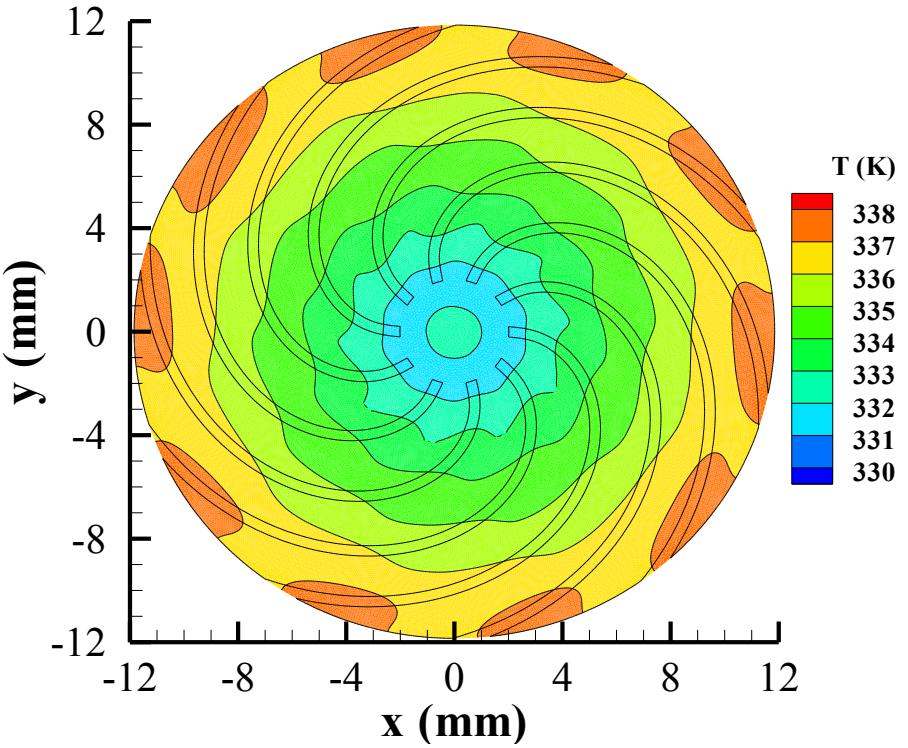

Figure. 6.22 Temperature distribution on the bottom surface, Re=997

Figure.6.23 shows the effect of the inlet Reynolds number on maximum temperature under the two heat flux conditions. Increasing the inlet velocity leads to lower maximum temperature due to more drastic convection heat transfer. Non-uniform heating causes a higher maximum temperature than uniform heating at a certain Reynolds number.

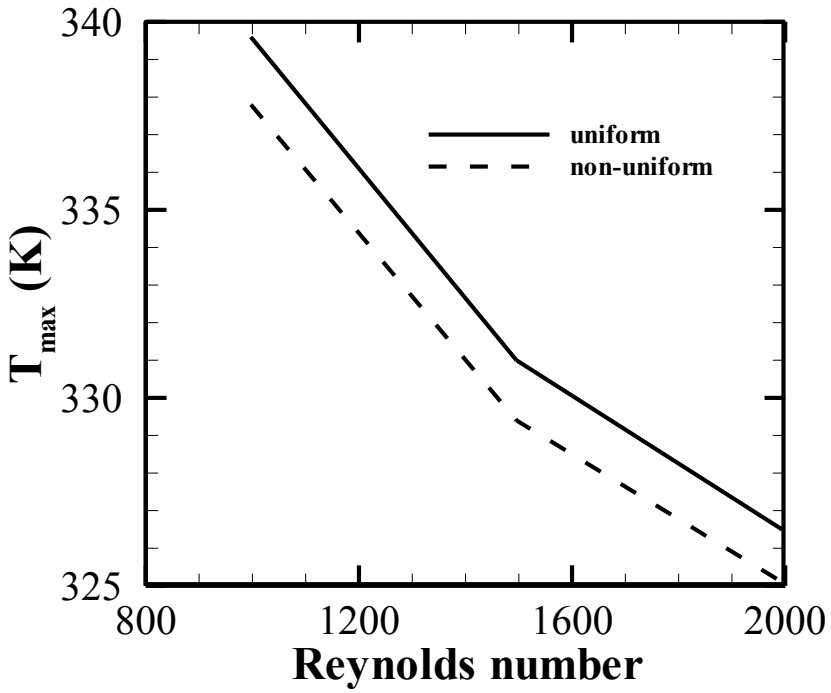

Figure. 6.23 Maximum temperature

From Figure.6.24, it can be seen that the temperature uniformity of the bottom surface is improved by increasing Reynolds number under both heating condition. The heat sink maintains smaller temperature difference when varying heat flux with exponential variation is applied to the bottom. The temperature uniformity is improved by 10 K at most than that under uniform heating.

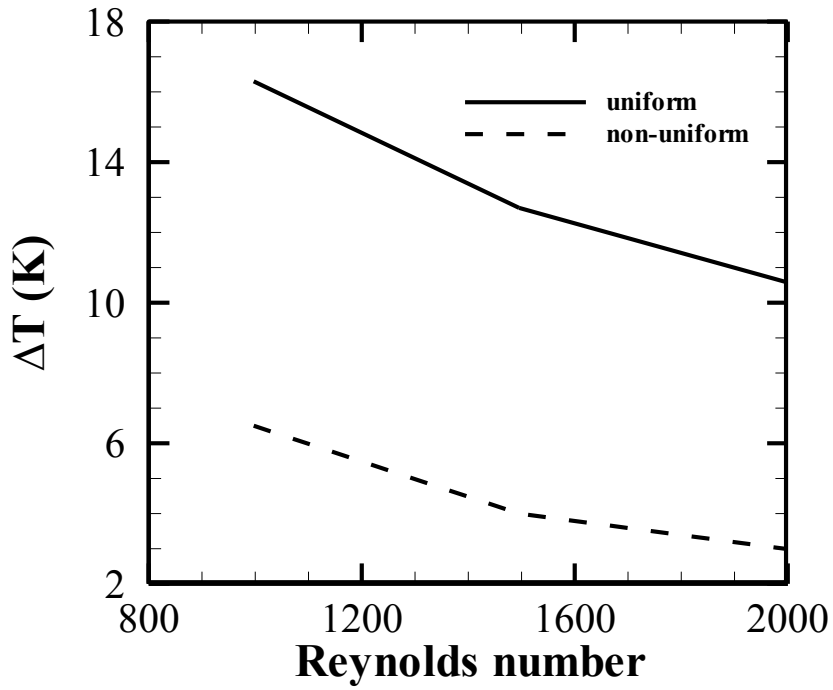

Figure. 6.24 Temperature difference

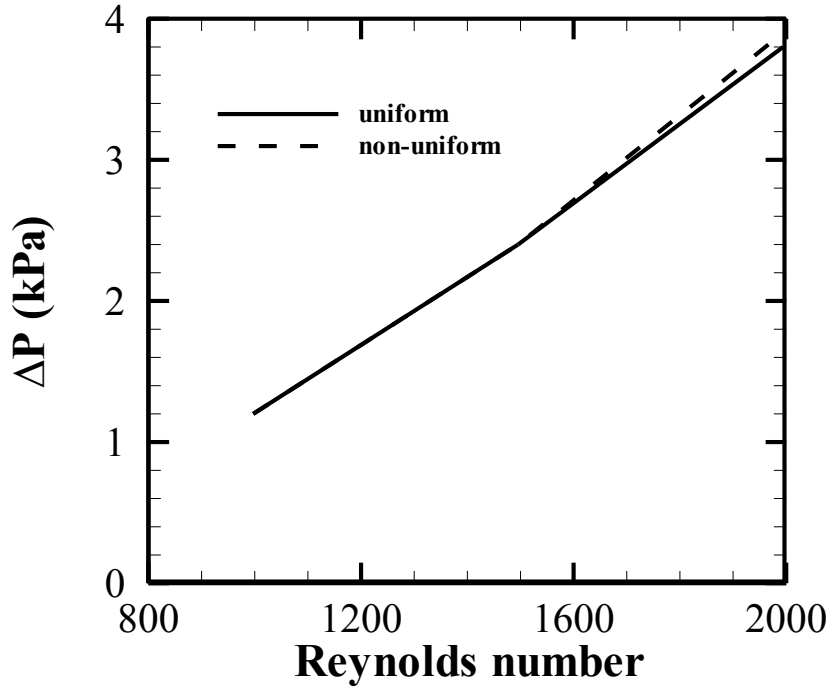

Figure. 6.25 Pressure drop

Figure.6.25 presents the pressure drop under different heating conditions with various inlet Reynolds numbers. Increasing the Reynolds number increases the pressure loss. The pressure drop is slightly affected by the heating conditions. Uniform heating leads to a smaller pressure drop at high Reynolds number.

The overall average Nusselt numbers of the heat sink under both heating conditions are compared with various inlet Reynolds number in Figure.6.26. The heat sink performance is similar to that under linear varying heat flux. Under uniform heating condition, the Nusselt number is higher than that under non-uniform heating condition.

The dimensionless total thermal resistance for the heat sink is calculated (Equation.5.3) and presented in Figure.6.27. The dimensionless thermal resistance is reduced when the inlet Reynolds number increases. Under non-uniform heat flux condition, the dimensionless thermal resistance is larger which demonstrates larger cooling capacity for the heat sink.

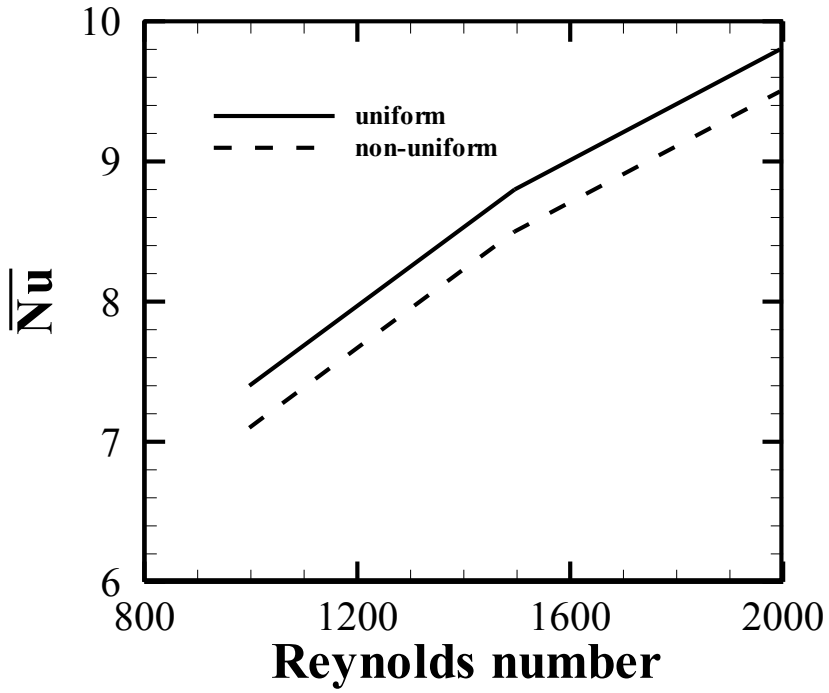

Figure. 6.26 Nusselt number

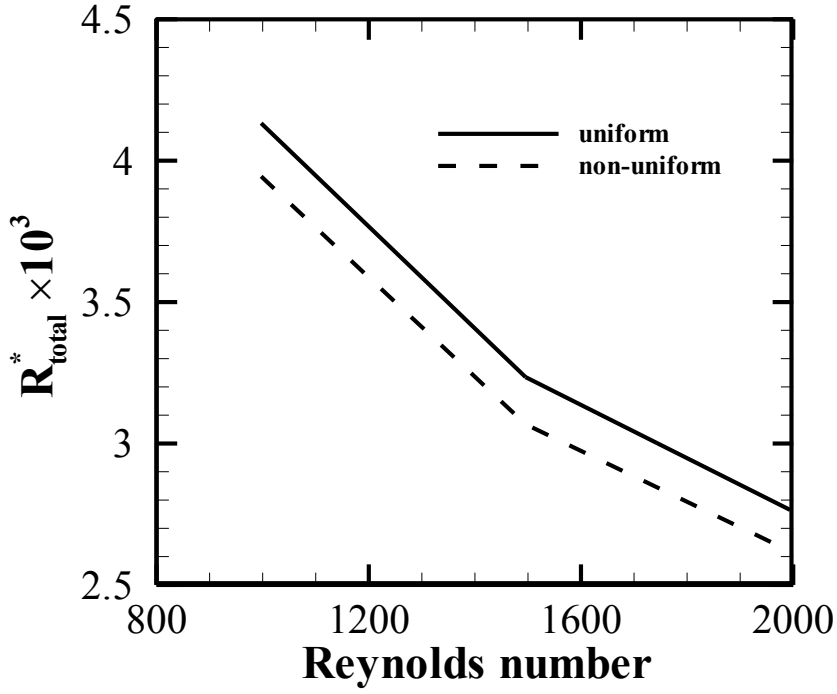

Figure. 6.27 Dimensionless total thermal resistance

6.4 Summary

Throughout this chapter, the swirl channel micro heat sink is numerically studied for cooling on a circular plate. Firstly, uniform heat flux is supplied to the bottom surface of the heat sink and different cross sectional geometries are tested under various heat fluxes. Results show that triangular channels provide the best cooling performance. Secondly, the swirl channel micro heat sink with triangular channels is simulated under two kinds of continuously varying heat fluxes. Better cooling performance can be observed for the heat sink under continuously varying heat flux than that under uniform heating. Under uniform heating, the Nusselt number is higher. The pressure drop is not significantly affected by the heat flux.

Chapter 7 Conclusions and Future Works

7.1 Conclusions

In this work, the cooling performance of microchannel heat sinks were numerically studies under different non-uniform heating conditions using Fluent. Two types of non-uniform heat flux conditions were proposed which were heat flux with hotspots and continuously varying heat flux.

For the heat flux with hotspots, cross-linked microchannel heat sink was used for cooling. The effects of the positions and the amount of heat fluxes of the hotspots were investigated. It was found out that when hotspots were placed in the upstream region or upstream hotspots were subjected to a higher heat flux than the downstream one, the performance of the heat sink was better. This was because of the low temperature of fluid in the upstream region.

With the presence of the cross-linked channels, temperature distribution had better uniformity at the hotspot zones and the pressure drop of the heat sink decreased. However, the effects were minor. Heat sinks with wider cross-linked channel caused rapid increase of temperature at the hotspots. Consequently, the cross-linked heat sink with a cross-linked channel width of 0.5 mm had the best cooling performance among all investigated widths. The effects of the positions of the cross-linked channels were also studied. No significant improvement in temperature distribution or pressure drop was found.

For the continuously varying heat flux, straight channel micro heat sink was applied for cooling with the heat flux on a rectangular plate while swirl channel micro heat sink was used for cooling of heat flux on a circular plate.

There were two layouts of straight channel heat sink. Heat flux was changing perpendicular and along the flow direction for layout 1 and layout 2 respectively. Comparison between the results of the two showed that layout 2 had better cooling performance than layout 1 with lower maximum temperature, temperature difference, and dimensionless pressure drop. The dimensionless total thermal resistance for heat sink layout 2 was also smaller and less responsive to heat flux which indicated that layout 2 was more suitable for high heat flux conditions. Layout 2 maintains a much larger overall average Nusselt number than that of layout 1. The geometry parameters of layout 2 were then optimized with Taguchi method under three heat fluxes. For all optimum designs, the cooling performance was most sensitive to the width of channel (W_{ch}) and all of the optimal designs had the smallest channel width in the test range. The cooling performance of the optimal designs was similar and satisfactory.

The swirl channel micro heat sink was first investigated under uniform heating conditions in order to obtain the best cross sectional geometry among the four proposed geometries. The triangular channel provides the best cooling performance. Two continuously varying heat fluxes were proposed which

changed along radial direction in linear and exponential variations. Better cooling performance can be obtained under continuously varying heat flux than that under uniform heating. However, the Nusselt number is higher under uniform heating conditions.

7.2 Contributions

In this work, numerical studies are conducted to investigate the effects of non-uniform heating conditions and geometries of the heat sinks on their cooling performances. It is discovered that it's better to place the hotspots in the upstream region of the heat sink. The cross-linked channels are found ineffective in non-uniform heating conditions with hotspots. For continuously varying heat fluxes, heat sinks have better cooling performance when heat fluxes decreases along flow direction. With this condition, heat sink can have good performance under heat fluxes with different slopes. High aspect ratio of the channel leads to better performance. The triangular channel is found most effective to improve the performance of the swirl channel heat sink when Reynolds number at the channel entrance is fixed. Continuously varying heat fluxes lead to a better cooling performance.

7.3 Future works

In the future, improvements of current work can be conducted in the following aspects:

1. The cross-linked channels were found ineffective for cooling of hotspots using single-phase laminar flow. The number of cross-linked channels shall be increased to seek chance of improvement in performance. Or new designs of heat sinks shall be proposed or numerical study in two-phase flow shall be performed.

2. For the straight channel heat sink, optimization may be conducted in wider ranges in order to obtain general directions for designs of heat sink geometries.

3. Geometry improvements can be made to the swirl channel heat sink by increasing the channel curvature and channel number. Continuously varying heat fluxes with different distributions may be applied on the swirl channel heat sink for better cooling performance.

Publications from Thesis Work

Conference

Ling, L., Fan, Y.F., and Hassan, I., "Numerical Study of Microchannel Heat Sinks with Non-uniform Heat Flux Conditions", *ASME 2011 9th International Conference on Nanochannels, Microchannels and Minichannels, (ICNMM2011),* June 19-22, 2011.

Ling, L., Fan, Y.F., and Hassan, I., "N*umerical Study of Microchannel Liquid Cooling under Uniform and Non-uniform Heating Conditions*", Engineering and Technological Innovation (IMETI 2011), July 19 - 22, 2011.

References

Asgari, O., Saidi, M.H., "Approximate Method of Determining the Optimum Cross Section of Microchannel Heat Sink", *Journal of Mechanical Science and Technology*, Vol.23 (12), 2010, 3448-3458.

Bejan, A. and Sciubba, E., "The Optimal Spacing of Parallel Plates Cooled by Forced Convection", *International Journal of Heat and Mass Transfer*, Vol. 35, 1992, 3259-3264.

Biswal, L., Chakraborty, S., Som, S.K., "Design and Optimization of Single-Phase Liquid Cooled Microchannel Heat Sink", *IEEE Transactions on Components and Packaging Technologies*, Vol. 32 (4), 2009, 876-886.

Bogojevic, D., Sefiane, K., Walton, A.J., Lin, H., "Experimental Investigation of Non-Uniform Heating Effect on Flow Boiling Instabilities in a Microchannel-Based Heat Sink", *International Journal of Thermal Sciences*, Vol. 50 (3), 2009, 309-324.

Chamarthy, P., Garimella, S. V., and Wereley, S. T., "Measurement of the Temperature Non-uniformity in a Microchannel Heat Sink using Microscale Laser-induced Fluorescence", *International Journal of Heat and Mass Transfer*, Vol. 53, 2010, 3275-3283.

Cho, E.K., Choi, J.W., Yoon, J.S., Kim, M.S., "Modeling and Simulation on the Mass Flow Distribution in Microchannel Heat Sinks with Non-Uniform Heat Flux Conditions", *International Journal of Heat and Mass Transfer,* Vol. 53 (7-8), 2010, 1341-1348.

Cho, E.K., Koo, J.M., Jiang, L.N., Prasher, R.S., Kim, M.S., Santiago, J.G., Kenny, T.W., Goodson, K.E., "Experimental Study on Two-Phase Heat Transfer in Microchannel Heat Sinks with Hotspots", *Nineteenth Annual IEEE Semiconductor Thermal Measurement and Management Symposium*, 2003, 242-246.

Dickey, J. Todd, Lam, Tung T., "Heat Transfer in Triangular Microchannels", *ASME 2003 International Electronic Packaging Technical Conference and Exhibition, InterPACK2003*, Vol.2, 2003, 303-307.

Fan, Y.F., Hassan, I., “Investigation of Cooling Performance of a Swirl Microchannel Heat Sink by Numerical Simulation”, *Proceedings of 9th ASME International Conference on Nanochannels, Microchannels, and Minichannels*, 2011.

Gatapova, E.Ya., Kabov, O.A., “Shear-Driven Flows of Locally Heated Liquid Films”, *International Journal of Heat and Mass Transfer*, Vol. 51(19-20), 2008, 4797-4810.

He, Y.L., Xiao, J., Cheng, Z.D., Tao, Y.B., “A MCRT and FVM Coupled Simulation Method for Energy Conversion Process in Parabolic Trough Solar Collector”, Renewable Energy, 2011, 36(5), pp. 976-985.

Hestroni, G., Mosyak, A., Segal, Z., “Nonuniform Temperature Distribution in Electronic Devices Cooled by Flow in Parallel Microchannels”, IEEE Transactions on Components and Packaging Technologies, Vol. 24 (1), 2001, 16-23.

Jayakumar, J.S., Mahajani, S.M., Mandal, J.C., Vijayan, P.K., Bhoi, Rohidas, “Experimental and CFD Estimation of Heat Transfer in Helically Coiled Heat Exchangers”, *Chemical Engineering Research and Design*, Vol. 86 (3), 2008, 221-232.

Kuan W. K., Kandlikar, S.G., “Experimental Study and Model on Critical Heat Flux of Refrigerant-123 and Water in Microchannels”, *Journal of Heat Transfer*, 2008, 1-5.

Lee, T.-Y.T., “Design Optimization of an Integrated Liquid-Cooled IGBT Power Module using CFD Technique”, *Proceedings of 6th Intersociety Conference on Thermal and Thermomechanical Phenomena in Electronic Systems*, 1998, 337-342.

Li, J., Peterson, G.P., “Geometric Optimization of a Micro Heat Sink with Liquid Flow”, *IEEE Transactions on Components and Packaging Technologies*, Vol.29 (1), 2006, 145-154.

Liu, S.T., Zhang, Y.C., Liu, P., “Heat Transfer and Pressure Drop in Fractal Microchannel Heat Sink for Cooling of Electronic Chips”, *Heat and Mass Transfer*, Vol. 44 (2), 2007, 221-227.

Muwanga, R., Hassan, I., "Flow and Heat Transfer in a Cross-Linked Silicon Microchannel Heat Sink". *Journal of Thermophysics and Heat Transfer*, Vol. 22 (3), 2008, 333-341.

Nonino, C., Savino, S., and Del Giudice, S., "Temperature-Dependent Viscosity and Viscous Dissipation Effects in Microchannel Flows With Uniform Wall Heat Flux", *Heat Transfer Engineering*, Vol. 31 (8), 2010, 682–691.

Poh, S.T., Ng, E.Y.K., "Heat Transfer and Flow Issues in Manifold Microchannel Heat Sinks: A CFD Approach", *Proceedings of 2nd Electronics Packaging Technology Conference*, 1998, 246-250.

Prapas, D.E., Norton, B., Probert, S.D., "Thermal Resistance of a Solar-Energy Collector Absorber under a Non-Uniform Flux Distribution", *International Journal of Heat and Mass Transfer*, Vol. 31(5), 1988, 1103-1111.

Qu, W.L., Siu-Ho, A., "Liquid Single-Phase Flow in an Array of Micro-Pin-Fins Part I: Heat Transfer Characteristics", *Journal of Heat Transfer*, Vol. 130 (12), 2008, 1-11.

Revellin, R., Quiben, J.M.; Bonjour, J., Thome, J.R., "Effect of Local Hot Spots on the Maximum Dissipation Rates during Flow Boiling in A Microchannel", *IEEE Transactions on Components and Packaging Technology*, Vol. 31 (2), 2008, 407-416.

Revellin, R., Thome, John R., "A Theoretical Model for the Prediction of the Critical Heat Flux in Heated Microchannels", *International Journal of Heat and Mass Transfer*, Vol. 51 (5-6), 2008, 1216-1225

Sankar, M., Do, Younghae, "Numerical Simulation of Free Convection Heat Transfer in A Vertical Annular Cavity with Discrete Heating", *International Communications in Heat and Mass Transfer*, Vol. 37 (6), 2010, 600-606.

Tuckerman, D.B., Pease, R.F.W., "High-Performance Heat Sinking for VLSI", *IEEE Electron Device Letters*, Vol. EDL-2 (5), 1981, 126-129

Wang, X.J., Zhang, W., Liu, H.J., Chen, L., Li, Z.S., "Numerical Simulation on Variable Width Multi-Channels Heat Sinks with Non-Uniform Heat

Source", *Proceedings of International Conference on Electronic Packaging Technology and High Density Packaging*, 2009, 1155-1158.

Wang, Y.L., Liu, Q.B., Sui, J., Zhao, Y.H., Su, J.F., Li, H.P., Jin, H.G., "Experimental and Simulation Investigation on a Parabolic Trough Solar Collector", *Journal of Engineering Thermophysics*, Vol. 31(8), 2010, 1261-1264.

Xu, J.L., Gan, Y.H., Zhang, D.C., Li, X.H., "Microscale Heat Transfer Enhancement using Thermal Boundary Layer Redeveloping Concept", *International Journal of Heat and Mass Transfer*, Vol. 48 (9), 2005, 1662-1674.

Xu, J.L., Song, Y.X., Zhang, W., Zhang, H., Gan, Y.H., "Numerical Simulations of Interrupted and Conventional Microchannel Heat Sinks", *International Journal of Heat and Mass Transfer*, Vol. 51 (25-26), 2008, 5906-5917.

Yilmaz, A., Buyukalaca, O., and Yilmaz, T., "Optimum Shape and Dimensions of Ducts for Convective Heat Transfer in Laminar Flow at Constant Wall Temperature", *International Journal of Heat and Mass Transfer*, Vol.43, 2000, 767-775.

Zhang, H.Y., Pinjala, D., Joshi, Y.K., Wong, T.N., Toh, K.C., "Development and Characterization of Thermal Enhancement Structures for Single-Phase Liquid Cooling in Microelectronics Systems", *Heat Transfer Engineering*, Vol.28 (12), 2007, 997-1007.

Zhang, M.L., Wang X.J., Liu H.J., Wang G.L., "Numerical Simulation of the Micro-Channel Heat Sink on Non-Uniform Heat Source", *Proceedings of International Conference on Electronic Packaging Technology & High Density Packaging*, 2008, 3-6.